Micromechanics of Fiber Networks Including Nonlinear Hysteresis and its Application to Multibody Dynamic Modeling of Piano Mechanisms

by

Ramin Masoudi

A thesis
presented to the University of Waterloo
in fulfillment of the
thesis requirement for the degree of
Doctor of Philosophy
in
Systems Design Engineering

Waterloo, Ontario, Canada, 2012

I hereby declare that I am the sole author of this thesis. This is a true copy of the thesis, including any required final revisions, as accepted by my examiners.

I understand that my thesis may be made electronically available to the public.

Abstract

Many engineering applications make use of fiber assemblies under compression. Unfortunately, this compression behavior is difficult to predict, due to nonlinear compliance, hysteresis, and anelasticity. The main objective of this research is to develop an algorithm which is capable of incorporating the microscale features of the fiber network into macroscopic scale applications, particularly the modeling of contact mechanics in multibody systems. In micromechanical approaches, the response of a fiber assembly to an external force is related to the response of basic fiber units as well as the interactions between these units, i.e. the mechanical properties of the constituent fibers and the architecture of the assembly will both have a significant influence on the overall response of the assembly to compressive load schemes. Probabilistic and statistical principles are used to construct the structure of the uniformly-distributed random network. Different micromechanical approaches in modeling felt, as a nonwoven fiber assembly with unique mechanical properties, are explored to gain insight into the key mechanisms that influence its compressive response. Based on the deformation processes and techniques in estimating the number of fiber contacts, three micromechanical models are introduced: (1) constitutive equations for micromechanics of three-dimensional fiberwebs under small strains, in which elongation of the fibers is the key deformation mechanism, adapted for large deformation ranges; (2) micromechanical model based on the rate theory of granular media, in which bending and torsion of fibers are the predominant elemental deformations used to calculate compliances of a particular contact; and (3) a mechanistic model developed using the general deformation theory of the fiber networks with fiber bending at the micro level and a binomial distribution of fiber contacts.

A well-established mechanistic model, based on fiber-to-fiber friction at the micro level, is presented for predicting the hysteresis in compression behavior of wool fiberwebs. A novel algorithm is introduced to incorporate a hysteretic micromechanical model – a combination of the mechanistic model with microstructural fiber bending, which uses a binomial distribution of the number of fiber-to-fiber contacts, and the friction-based hysteresis idea – into the contact mechanics of multibody simulations with felt-lined interacting bodies. Considering the realistic case in which a portion of fibers slides, the fiber network can be treated as two subnetworks: one from the fibers with non-sliding contact points, responsible for the elastic response of the network, and the other consisting of fibers that slide, generating irreversible hysteresis phenomenon in the fiberweb compression. A parameter identification is performed to minimize the error between the micromechanical model and the elastic part of the loading-unloading experimental data for felt, then contribution of friction was added to the obtained mechanistic compression-recovery curves.

The theoretical framework for constructing a mechanistic multibody dynamic model of a vertical piano action is developed, and its general validity is established using a prototype model. Dynamic equations of motion are derived symbolically for the piano action using a graph-theoretic formulation. The model fidelity is increased by including hammer-string interaction, backcheck wire and hammer shank flexibility, a sophisticated key pivot model, nonlinear models of bridle strap and butt spring, and a novel mathematical contact model. The developed nonlinear hysteretic micromechanical model is used for the hammer-string interaction to affirm the reliability and applicability of the model in general multibody dynamic simulations.

In addition, dynamic modeling of a flexible hub-beam system with an eccentric tip mass including nonlinear hysteretic contact is studied. The model represents the mechanical finger of an actuator for a piano key. Achieving a desired finger-key contact force profile that replicates that of a real pianist's finger requires dynamic and vibration analysis of the actuator device. The governing differential equations for the dynamic behavior of the system are derived using Euler-Bernoulli beam theory along with Lagrange's method. To discretize the distributed parameter flexible beam in the model, the finite element method is utilized. Excessive vibration due to the arm flexibility and also the rigid-body oscillations of the arm, especially during the period of key-felt contact, is eliminated utilizing a simple grounded rotational dashpot and a grounded rotational dashpot with a one-sided relation. The effect on vibration behavior attributed to these additional components is demonstrated using the simulated model.

Acknowledgements

I would like to
Express my deep appreciation to my supervisor, Professor John McPhee,
for his continued support, valuable guidance,
and the freedom he gave me during the course of the research.

I also wish to
Express my gratitude to my committee members,
Professor Glenn Heppler, Professor Eihab M. Abdel-Rahman , and Professor Hamid Jahed,
for reviewing my thesis and the part they played in developing my education.

Sincere thanks to
My sponsors, Natural Sciences and Engineering Research Council of Canada, Steinway & Sons,
and Brand Felt of Mississauga,
for their financial supports.

I am grateful to
My fellow students in Motion Research Group, especially Tom Uchida and Aden Seaman,
for all seminars, discussions, support, and for providing a friendly and dynamic environment.

I would like to extend my heartfelt gratitude to
My parents, father, and mother, for their unflagging love and support, and
for giving me the encouragement, understanding, and care.

Finally and most importantly, I wish to
Express my utmost appreciation to my wife for her CONSTANT *love,*
STABLE *understanding,* CONTINUOUS *sacrifice, and* NON-STOPING *support,*
without which none of this would have materialized.

Dedication

To my beloved parents, father, mother, and my dearest friend and partner, Nasim Choroumi.

Table of Contents

List of Tables

List of Figures

Nomenclature

(x_{hsc}, y_{hsc}) Hammer contact circle center coordinates

$(x_p, \dot{x}_p)$ Position and speed of a typical point p on the actuator flexible beam

: Double-dot product

$[C]$ Compliance tensor

$[S]$ Stiffness tensor

α Unloading-loading transition speed parameter

β Crimp ratio

$\boldsymbol{\delta}$ Kronecker delta

$\boldsymbol{\psi}(\boldsymbol{e})$ Probability of finding a fiber with configuration $\boldsymbol{e}$

Δ Dynamic penetration depth of string in hammer felt

δ Dirac delta function

δ_f Length scale on which the fiber can be considered straight

δ_n Node deflection

δ_Y Deformation in Y direction

$\delta_{LU}(\varepsilon_p)$ Difference between loading and unloading curve fits

Δ_{bs} elongation of the bridle strap

ℓ_c Half the crimp spacing

ϵ Engineering strain

η_n Node density

$\eta_j(t)$ jth mode of string vibration

$\gamma_{ij,\ i\neq j}$ Shear strains

$\hat{\alpha}$ Retarded time parameter

$\hat{\kappa}_{(\theta,\phi;\theta',\phi')}$ Angle between two arbitrary spatial fiber

$\hat{\boldsymbol{\Phi}}$ State vector of the generalized positions and velocities for the piano action

$\hat{\boldsymbol{C}}(t)$ Rigid body translation between two frames of reference

$\hat{\boldsymbol{Q}}$ Orthogonal time-dependent second-order tensor

$\hat{J}$ Compliance nonlinearity exponent

$\hbar(\boldsymbol{e})$ The average number of fibers that contact the fiber with direction $\boldsymbol{e}$

$\imath$ Hysteresis amplitude

$\langle\cdot\rangle_c$ Average over all possible values of contact variables

$\boldsymbol{e}$ Unit vector along the test fiber axis

$\boldsymbol{F}$ Deformation gradient tensor

$\boldsymbol{F}(\boldsymbol{q},\dot{\boldsymbol{q}},t)$ Column matrix of generalized forces

$\boldsymbol{F}_0$ Initial deformation tensor

$\boldsymbol{F}_r$ Deformation tensor in reference configuration

$\boldsymbol{I}$ Identity matrix

$\boldsymbol{K}$ Global stiffness matrix

$\boldsymbol{K}_n$ Stiffness matrix for the n^{th} element

$\boldsymbol{L}$ Spatial velocity gradient

$\boldsymbol{M}$ Mass matrix

$\boldsymbol{M}_n$ Local mass matrix of the n^{th} element

$\boldsymbol{n}$ Outward unit normal vector to the test particle surface at the point of contact

$\boldsymbol{P}$ Contact force between solid particles

$\boldsymbol{Q}$ Column matrix of generalized forces in FEM approach

$\boldsymbol{q}$ Column matrix of generalized coordinates

$\boldsymbol{q}_{\text{flex}}$ Time-dependent column matrix of generalized coordinates associated with flexible motions in hammer shank and backcheck wire

$\boldsymbol{q}_{\text{rigid}}$ Time-dependent column matrix of generalized coordinates associated with rigid-body motions

$\boldsymbol{r}$ Local position vector of the contact points

$\boldsymbol{V}$ Spatial velocity vector

$\boldsymbol{x}$ Position vector relative to an arbitrary coordinate system

$\boldsymbol{x}^*$ Mapped position vector

$\boldsymbol{X}_r$ Position vector in reference configuration

$\mathscr{L}$ Lagrangian

μ Coefficient of friction

μ_s String linear mass density

ν_n Relative normal speed between interacting bodies at the contact point

$\Omega(\theta, \phi)$ Orientation distribution function

$\overline{\lambda}$ Mean distance between contact points

$\overline{\lambda}_j$ Mean projection of the random fiber length on direction j

$\overline{\langle s_j \rangle_c}$ Average compliance of all contacts in the j direction

ϕ Azimuthal angle

$\phi_{in}(x)$ i^{th} shape function for the n^{th} element

$\phi_j(y)$ jth undamped mass-normalized mode shape of the string

Ψ Total energy stored in fibers

ρ_n Density of the n^{th} element

σ_f Stress along the fiber with orientation (θ, ϕ)

σ_{el} Elastic stress developed in the network during loading

σ_{eu} Elastic stress developed in the network during unloading

τ_0 Relaxation time

θ Polar angle

θ_{crj} Critical angle of sliding between fibers

$\theta_d(t)$ Damper rotation angle with respect to the ground frame

$\theta_h(t)$ Hammer rotation angle with respect to the ground frame

$\theta_j(t)$ Jack rotation angle with respect to the whippen frame

$\theta_k(t)$ Key rotation angle with respect to the ground frame

θ_n Rotations at the end nodes of the n^{th} element

$\theta_w(t)$ Whippen rotation angle with respect to the ground frame

υ_f^{random} Volume fraction for the initial random state

υ_m The maximum number of contact points that could be created on a fiber length

ε Inharmonicity index of string

ε_f Strain along a random fiber element

ε_p Penetration depth between interacting bodies

$\varepsilon_{ij,\ i=j}$ Normal strains

ϑ Mean value of Poisson distribution

ξ_j String modal damping

$\zeta(\boldsymbol{r}, \boldsymbol{n}, \dots)$ The probability density of configuration $(\boldsymbol{r}, \boldsymbol{n}, \dots)$

a Equivalent radius of the hub

A_f Cross section area of the fiber

A_n Cross section area of the n^{th} element

$B(k; \upsilon_m, S(\vartheta))$ Binomial distribution of the number of contact points on the fiber

C_j Contact force between interacting fibers in direction j

C_{jn} Normal contact force between interacting fibers, generated by C_j

C_{jt} Tangential force on the test fiber, generated by C_j

C_{ns} Average contact force per non-sliding contact point

C_{params} Contact parameters for hammer-string interaction

C_s Average contact force per sliding contact point

d String diameter

d_f Fiber diameter

D_{bs} Deformed length of the bridle strap

E Young's modulus of elasticity of the fiber element

E_i Modulus of elasticity of the fiber network in the principal direction i

E_s Young's modulus of elasticity of the string

E_{Bi} Structural energy stored in fibers due to bending

E_n Modulus of elasticity of the n^{th} element

E_{Si} Structural energy stored in fibers due to slipping

E_{Ti} Structural energy stored in fibers due to straightening

f Orientation structural tensor

F_0 Instantaneous stiffness

F_{action} Equivalent reaction force from the piano action to the actuator system

$F_L(\varepsilon_p)$ Loading curve fit to the felt experimental data

F_n Normal contact force between interacting bodies

$f_n(t)$ Normal impact force in hammer-string interaction

$F_U(\varepsilon_p)$ Unloading curve fit to the felt experimental data

F_Y Transverse contact force in Y direction

f_{bs} Bridle strap force

F_{felt} Contact force in the actuator system

F_G Force due to gravity

H Heaviside step function

$H(\varepsilon_p)$ Heaviside step function

I Second moment of area of the fiber cross section

I_n Second moment of area of the n^{th} element

J_H Moment of inertia of the hub

k Number of exact occurrences in Poisson distribution

KE_n Kinetic energy for the element n

K_B Bending spring constant

k_b Bending uncertainty parameter

K_E Uncertainty parameter in Narter's approach

K_p Uncertainty parameter for Neckář model based on a binomial distribution of fiber contacts

k_p Statistical uncertainty constant in van Wyk's model

K_S Tensile/compressive spring constant

k_t Torsion uncertainty parameter

L Length of the actuator beam

l Undeformed fiber segment length

l_f Total fiber length in the assembly

l_n Length of the element n

L_s String speaking length

l_v Total fiber length per unit volume

L_{bs} Undeformed length of the strap

$m_{_T}$ Tip mass

N Total number of fiber contacts

N_B Number of fibers undergoing bending

N_f Number of fibers in the total volume of the fiber assembly

N_S Number of fibers undergoing slipping

N_T Number of fibers undergoing straightening

N_v Number of fiber-to-fiber contacts per unit volume of the fiber network

$n_{\overline{\lambda}_j}$ Number of contact points in the volume $V_{\overline{\lambda}_j}$

N_{fc} Average number of contacts on an arbitrary fiber

N_{fv} Number of straight fiber segments per unit volume

N_m Number of string modes in the string model

n_U Number of elastic generalized coordinates in the longitudinal direction

n_V Number of elastic generalized coordinates in the lateral direction

$P(v_f)$ Macroscopic pressure on the fiber network

PE_n Potential energy for element n

p_c Nodal force

$P_f(\theta, \phi)$ Axial force along the fiber with orientation (θ, ϕ)

p_j Contact force between fibers in the j direction

$p_{2\to1}$ Probability that fiber No.2 interacts with fiber No.1

$P_{loading}$ Macroscopic loading pressure on the fiber network

$P_{unloading}$ Macroscopic unloading pressure on the fiber network

r Eccentricity

r_f Fiber radius

r_j Contact position vector component in the j direction

r_{cut} Cut-off distance between the fibers centerline

r_h Equivalent radius of the hammer head virtual circle

$r_{i,j}$ Distance between centerlines of two non-consecutive imaginary fibers

r_{sc} Proportion of fiber contact points that slide

s Nodal compliance

s_j Local compliance of a particular contact in the j direction

$s_{i,i+1}$ Elongation between two nodes

T String tension

T_h Applied torque on the hub by the motor

U Stain energy function

$u_{fs}^n(t)$ Elastic generalized coordinates in the longitudinal direction for flexible hammer shank

$u_{fw}^n(t)$ Elastic generalized coordinates in the longitudinal direction for flexible backcheck wire

V Volume of the fiber assembly

v Fiber volume in the network

$v_{fs}^{n}(t)$ Elastic generalized coordinates in the lateral direction for flexible hammer shank

$v_{fw}^{n}(t)$ Elastic generalized coordinates in the lateral direction for flexible backcheck wire

v_f Fiber volume fraction

v_t Threshold speed

$V_{\overline{\lambda}_j}$ Volume with unit cross section area and the height $\overline{\lambda}_j$

$v_{f,m}$ Critical volume fraction

v_{f0} Initial volume fraction

W Volume occupied by all the fiber contact points

Wf_0 Withdrawal force per unit length of fiber in the absence of external loads on the fiber mass

w_f Contact volume fraction

w_n Elastic deformations at the end nodes of the n^{th} element

$w_n(x,t)$ Elastic displacement for the element n

$Y_{key}(t)$ Key pivot translational displacement

$\overset{\triangle}{\boldsymbol{\sigma}}$ Truesdell stress rate tensor

Chapter 1

Introduction

1.1 Research goals

Fiber assemblies play an important role in various industrial applications, e.g. thermal insulation, sound insulation, fluid filtration, vibration isolators, and deformable structures. Nonwoven fabrics are broadly defined as web structures that are bonded mechanically, thermally or chemically together by entangling fibers or filaments. The complex structures and random features of these fiber networks demand a systematic structural characterization and precise mechanistic formulation to study their performance under various loading schemes.

Felt, a nonwoven fibrous material formed by interlocked wool fibers, has been used in musical instruments as the vibration damper or to remove undesired noises for many years. For instance, in piano action mechanisms, all contacting surfaces and bushings are lined with felt or leather to allow a softer feel and reduce mechanical noise in the action. In addition, piano hammers are covered with a dense felt layer to produce a softer sound, interacting with complaint strings.

Determining the mechanical properties of these networks subjected to repeated compressive stresses has been a challenging issue in many fields of engineering. This is specifically utilized in contact modeling between felt-lined interacting bodies in dynamic analysis of multibody systems. Modeling felt compression versus force characteristics is a complex and computationally expensive process, so simplification scenarios such as statistical and probabilistic techniques are incorporated to derive a force-compression relation that can be updated at every step of a multibody simulation in a reasonable time.

The main objectives of this research can be categorized as follows:

1. To characterize the structure of a fiber mass statically and dynamically. This is important for extracting information regarding the properties of constituent fibers, like geometry and surface properties, as well as architecture of the network, such as fiber orientation distribution, mean free fiber length, number of fiber contacts, and predominant deformation mechanisms at the micro level.

2. To examine micromechanical models in generating the nonlinear compliance in fiber assembly compression, particularly felt, considering different microscale deformation schemes. Two micromechanical models have been assessed: the first one considers pure elongation of the fibers under small deformation ranges, and the second is based on the rate theory of granular media. Evaluation of the proposed models and parameters will be accomplished by comparing to experimental results.

3. To introduce a micromechanical model, appropriate for felt compression that incorporates nonlinear hysteresis based on microstructural features of the network.

4. To construct a multibody dynamic model of an upright piano action mechanism, employing the proposed micromechanical approach to include a mechanistic contact model between interacting bodies. The obtained simulation results are then compared to experimental ones from the real prototype mechanism.

5. To develop a finite element model (FEM) of a rotating flexible hub-beam system to the analyze dynamic and vibration response of a typical actuator system designed to replicate a pianist's finger force on the action prototype.

In developing the micromechanical model, uniform compression is considered, so that it can be extended to nonuniform cases such as curved layer of felt used in piano hammers or hammer butt cushions. Macroscopic nonlinear compliance is derived on the basis of microstructural fiber bending and fiber contacts, and hysteresis is incorporated by considering fiber-to-fiber friction and structural parameter changes during loading and unloading stages.

In comparison to grand piano actions, a vertical or upright piano (shown in Figure 1.1) is more compact because the frame and strings are placed vertically behind the keyboard, requiring an action with hammers striking the strings from the front. It is considered harder to produce a sensitive piano action with horizontally moving hammers, possibly because the hammer return is dependent on springs that are prone to wear and tear. So,

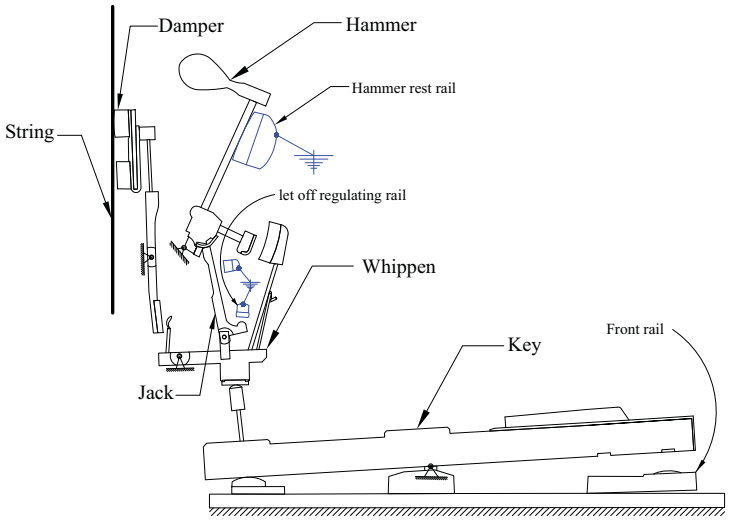

Figure 1.1: Side view of a vertical piano action mechanism.

more accurate and complicated modeling considerations are required when constructing the multibody simulation model. As the kinematic constraints of the mechanism at the contact surfaces are not simple ones, i.e. the different bodies are not always in contact during the action of the mechanism, a continuous analysis method has been used to model the impact so that these are treated as coupled applied forces during the contact period. Based on experimental observations, it seems necessary to include the flexibility in the hammer shank and backcheck wire. However, a trade-off between a more realistic component model and the computation cost should be examined. The results obtained in the micromechanical modeling of felt will be utilized in the context of the vertical action model and hammer-string interaction. Figure 1.2 demonstrates the way that a state-of-the-art modeling of fiber assemblies may be achieved and applied in the simulation of multibody systems including compliant contacts.

For experimental study of the dynamic behavior of the action, it is important to replicate the key input to the mechanism in an appropriate automated and repeatable way that accurately reflects a pianist's finger force on the key. To this end, a mathematical model of the mechanical actuator is beneficial in analyzing its performance and adjusting its design. A FEM-based simulation model of a rotating flexible hub-beam system with an eccentric tip mass is a methodical starting point for developing and constructing such actuator mechanisms, reproducing the pianist's finger force/motion on the key, and for analyzing the interaction between the action mechanism and the actuator system.

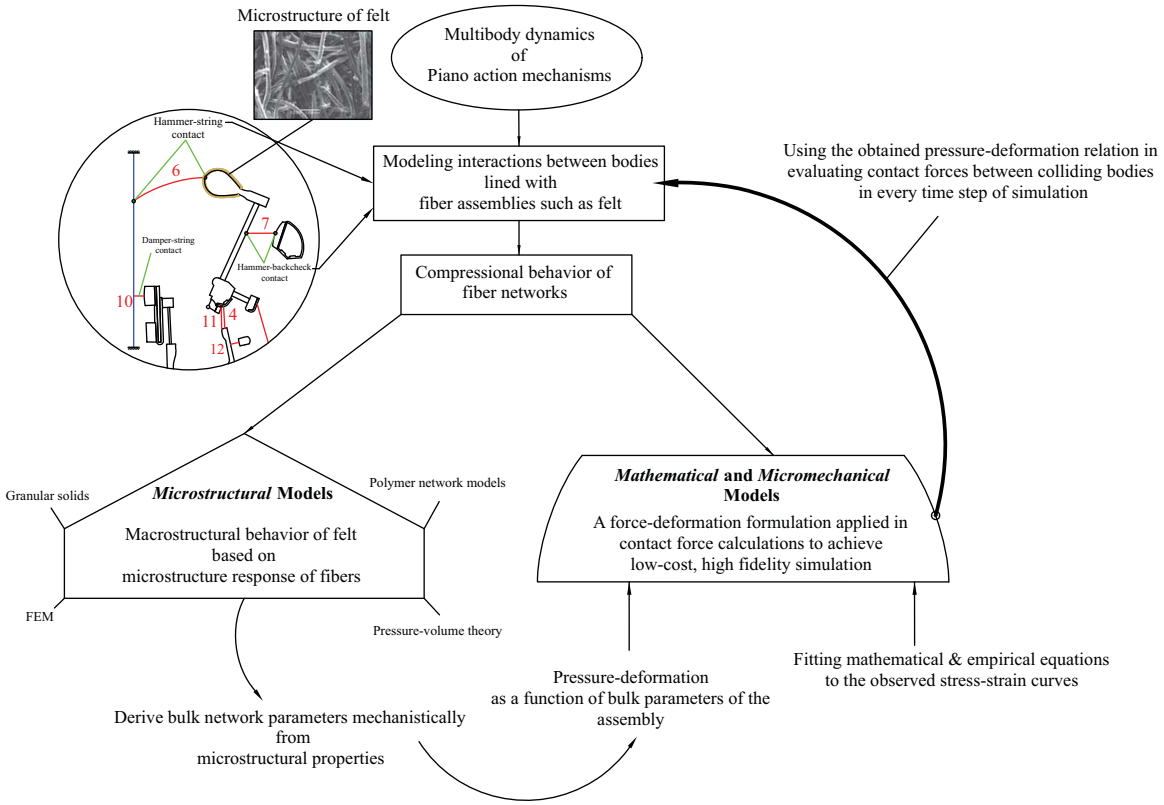

Figure 1.2: A descriptive flowchart, illustrates the proposed direction of the research project.

1.2 Background

Predicting mechanical behavior of nonwoven fabrics will have a considerable impact on the intended task expected from the assembly. There are three major trends in modeling the mechanical response of fiber assemblies: (1) statistical micromechanical models which are based on fitting mechanistic equations, achieved using statistical tools, to the observed stress-strain curves of the fiber assembly sample, and (2) microstructural models which adopt a continuum mechanics approach along with discretization techniques and involve the response of every single fiber in the network. (3) fitting mathematical and empirical equations to the experimental data, particularly when computation costs are at the highest importance level. In micromechanical models (statistical and microstructural models), the response of the fiber assembly to an external force is related to the response of basic fiber units along with interactions between fibers. Images taken using Scanning

Electron Microscopy (SEM) technology show that felt consists of random pattern of fibers with void-spaces in between; in comparison to composite materials, no matrix is present. Therefore, the forces applied on the felt at the macro level will flow through the assembly by interconnected fibers, assuming that there is nothing in the space between the fibers to store or dissipate energy. Assuming that the fibers are well dispersed in the assembly, statistical approaches such as averaging are employed to predict the contribution of fibers with specific alignments in responding to the loads on the bulk structure. In most cases, such fiber networks are modeled by straight structural elements located between contact points, called free fibers, with random orientations. The fiber network may be considered homogeneous, a reasonable assumption according to justifications considered by several former researchers. Moreover, according to experiments, the hysteretic behavior of the structure under compression is attributed to internal friction rather than viscous damping. This implies that fiber slippage in the current models cannot be ignored or substituted by viscoelastic elements. There are several existing models of mass-spring systems with Coulomb friction elements to account for hysteresis-dependant compressive behavior of fiber assemblies, but they do not convey the physical significance of a micromechanical concept.

1.3 Motivation

A piano action mechanism passes force applied on the key to a felt-covered hammer that strikes the strings to produce a desired sound. The interconnected bodies of the action must satisfy geometric and dynamic requirements in order to transfer the expected motions and generate the desired response. To allow a softer feel and reduce mechanical noise in the action, motion transition between different bodies is formed through contact surfaces covered with felt or similar fiber assemblies. Consequently, an accurate simulation model must involve a mechanistic contact approach to capture intermittent loading-unloading during the bodies' interaction. Estimating the value of contact forces in terms of penetration depth between colliding bodies in the dynamic simulation of the action motivates a systematic investigation into the nonlinear behavior of these contact interfaces. To be mechanistic, the developed contact model should employ microstructural features and response of the network, but be simple enough to estimate the contact forces using computationally low-cost algorithms in multibody dynamic simulations.

1.4 Challenges

Dynamic experimental studies on felt demonstrate some significant features of this nonwoven fiber network: nonlinear compliance, the effect of rate of loading on the slope of the loading curve, and complex hysteresis behavior. This means that wool felt has to be considered a material possessing history-dependent properties. Most research in micromechanical modeling of nonwovens have considered fiber bending as the dominant deformation mechanism in sustaining the macroscopic loads on the structure. It is important to construct a mechanistic model that accounts for the nonlinear compliance present in fiber assemblies with relatively high volume fraction (dense networks) under compressive load schemes. This may be done by introducing other deformation mechanisms: elongation and torsion of the constituent fibers. Furthermore, estimation of fiber orientation and number of fiber contacts has a broad room for further development. It strongly affects the mean free fiber length, and thus the response of the structure to force applied on the fiber mass. Sliding between fibers in nonwoven fabrics is one of the likely sources of hysteretic behavior of the network. It is a considerable challenge to incorporate friction dissipation, formed on a micromechanical concept, at the contact points. Applying more sophisticated computational tools such as finite element analysis and molecular dynamics approaches can be promising alternatives to the contact model, provided that their feasibility for this special case is examined. The key feature of these detailed methods is that nonlinear compliance of the structure as well as friction at contact points can be predicted at microscale levels.

Higher degree of simulation fidelity and accuracy in multibody dynamic modeling of piano action mechanisms can be acquired by including more precise modeling considerations in developing the equations of motion, e.g. flexible parts, compliant string, key pivot model, and mechanistic contact model. Incorporating micromechanical models, either microstructural models or statistical micromechanical models, into contact modeling of multibody system dynamics provides a wide context of research in both the micromechanics of fiber networks and computational techniques to involve them. Biomechanical approaches to making a more realistic finger model can significantly improve the input to the simulated piano action. In other words, a biomechanical model implies a more accurate input that is influenced by the response of the piano action components – the reaction force from the components, accumulated and transmitted through the key to the finger actuator mechanism – during a key stroke.

1.5 Applications

The micromechanics of fiber assemblies has numerous key applications in several leading-edge industrial technologies. The compliance and damping features of these fiber networks make them suitable for advanced manufacturing, musical instruments, the automotive industry, and robotics. It is particularly of interest in constructing fully mechanistic dynamic models of multibody systems with felt-lined interfaces. Results from this research project on piano technology can be beneficial to piano users, as well as piano manufacturers and technicians via developing and constructing more effective and sensible piano action mechanisms and components. Various types of felt have been used in piano hammers, backchecks, key punchings, and dampers to control the touch and noise generated by the action. A mechanistic model of felt compression can improve the modeling issues and increase fidelity of the simulated piano action model. Moreover, it facilitates a state-of-the-art design of felt and felt products utilized in piano mechanisms with enhanced performance.

1.6 Thesis Layout

Chapter 2 of the thesis is a literature review in which some of the accomplished investigations during recent decades are summarized in two main categories: in Section 2.1, the focus is on the characterization of the structure of fiber assemblies; Section 2.2 discusses several theories and developments in the micromechanical modeling of nonwoven fiber networks followed by new progress reported in this challenging field. It also examines existing criteria in modeling hysteresis of the fiber networks. Section 2.3 introduces previous work done on dynamic modeling of the piano action mechanism including contact modeling between colliding bodies, hammer shank flexibility, hammer-string interaction, and key pivot model.

Chapter 3 presents the research results in three correlated sections: Section 3.1 describes the preliminary experimental results obtained by scanning electron microscopy, its alternatives and guidelines in recognizing microstructure of nonwovens; Section 3.2 proposes and validates distinct criteria in modeling the compression behavior of fiber assemblies based on small deformation of dense fiber networks, rate theory of granular solids, and binomial distribution of fiber contacts; Section 3.3 establishes nonlinear hysteretic behavior of random fiber networks base on fiber-to-fiber friction at microscale followed by a novel method to apply it in dynamic simulation of multibody systems.

Chapter 4 focuses on dynamic modeling of a vertical piano action mechanism: Section 4.1 describes a mechanistic multibody dynamic model of a vertical piano action mecha-

nism, examining the approaches (micromechanical and mathematical models) proposed in chapter 3 for modeling contact between colliding bodies. Modeling issues in hammer shank and backcheck wire flexibility, hammer-string interaction, key pivot model, and bridle strap and butt spring are discussed in this section. In Section 4.2, an experimental prototype is constructed and instrumented to validate the simulation results. Regulation of the action is done following a sequence of specific events during the key stroke that maintain the proper feel and response of the action.

Chapter 5 initiates preliminary studies in dynamic and vibration analysis of a rotating flexible hub-beam system, an experimental version of which has been utilized to replicate the finger force profile on the piano action. In Section 5.1, a dynamic model of the mechanistic actuator is developed using Lagrange's approach and finite element analysis; simulation results from the actuation system is derived in Section 5.2 and discussed in Section 5.3. The obtained results are then quantitatively compared with the real finger force and possible ideas to achieve more realistic models are introduced.

Chapter 2

Literature Review

The micromechanical modeling of fiber assemblies requires extensive research in two major fields:

1. Characterizing the structure of the networks.
2. Modeling the nonlinear behaviors that may be present in nonwovens including nonlinear compliance, hysteresis, stress relaxation, and anelasticity.

The first area focuses on topology analysis of the network, geometrical and physical properties of the fibers, and dynamics of the structure deformation under different loading schemes. The latter deals with the correlation between the macroscopic response of the network and microstructural element reactions to the applied loads, including structural mechanics of fiber deformation, fibers interaction, and time-dependent responses.

Incorporating micromechanical models in the dynamic analysis of piano mechanisms, in which the overall nonlinear relation between force-deformation is required during interaction between colliding bodies, demands a background on multibody dynamic modeling of such systems. Furthermore, the micromechanical model should be simple enough so that calculation of contact forces can be carried out in a relatively short time for each simulation step. In general, micromechanical modeling of fiber assemblies based on microscale features of the network components can be categorized into two major groups:

1. *Microstructural models*: the models that represent microstructural behavior of fiber assemblies, relying on the response of representative elementary fiber units in tiny

scales using discretization techniques and continuum mechanics approaches. In fact, the deformation of every single fiber and its interaction with other fibers will be specifically considered in detail in these models. It is different from the statistical micromechanical models in which statistical concepts are employed to estimate the structure and components of the network in the form of fiber bundles with the same geometrical and physical features. Finite element method, discrete element method, and molecular dynamics are systematic procedures that employ discretization tools to study the macroscopic behavior of such networks based on response of the fiber segments and their interaction with other network components [5, 7, 8, 10, 34, 43, 77, 97, 98].

2. *Statistical micromechanical and mathematical models*: the models in which force-deformation calculations will be done in a relatively short time along with computationally low-cost algorithms. These models are obtained by fitting empirical and mathematical equations to the observed stress-strain curves [103–106] or can be developed using statistical and probabilistic tools to reduce the degree of complexity in microstructural approaches [1, 2, 39, 47–51, 53, 56–60, 72, 73, 110, 111, 115].

2.1 Experimental characterization of fiber assemblies

Several studies have been conducted in analyzing the architecture of nonwoven fiber networks using mathematical and statistical algorithms and image analysis tools. Tan et al. [108] measured distribution of fiber segment length and fiber orientation using analysis of tomography images. By utilizing a 3-D skeletonisation technique, they could reconstruct fiber surfaces and then reproduce them into a medial axis network. Using the generated network, geometrical data such as distribution of fiber segment and orientation could easily be extracted. The basics of scanning electron microscopy (SEM) and its applicability for nonconductive samples have been studied extensively by Goldstein et al. [30]. In the book, they referenced methods that can be applied to get reasonably traceable images from fabric networks (like felt) using metal coating. Various methods of sample preparation and coating along with the problems such as stresses generated on the samples, due to bombardment of the fibers with the coating material, have been discussed. They demonstrated that a combination of secondary electron (SE) and back scattered electrons (BSE) imaging can be used to distinguish contamination from surface morphology.

Environmental Scanning Electron Microscopy (ESEM) and its advantages over SEM, particularly for nonconductive, contaminant generating samples has been technically introduced in ESEM manual [4]. Its ability to obtain images from nonconductive samples

in a relatively short time, makes it a reliable candidate to study the mechanical behavior of such samples under dynamic deformation schemes. Rawal, Lomov, and Verpoest [95] relied on the capability of ESEM in capturing images at relatively short time intervals and performed an in-situ mechanical testing. It permitted investigating tensile behavior of through-air bonded structures by identifying the regions of deformation together with visual observations. The effect of fiber orientations on the mechanism of load transfer inside the network was analyzed by the dynamic characterization experiments. They observed architecture changes in some identified regions as well as stress-strain behavior of the structure at macroscale. As it was expected, the fibers that aligned in the loading direction would be the load bearing elements and the other fibers tended to reorient in the loading direction during the deformation. Furthermore, evolution in anisotropic characteristic of the assembly was discussed in the research work; specifically, it could be deduced that the anisotropy parameter in the network increased with an increase in the applied strain.

Pourdeyhimi et al. [44,81,82,84,86–89] directed a series of investigations on estimating fiber orientation in nonwoven fiber assemblies, considering different approaches, e.g. direct tracking, Fourier transform, flow field analysis, real webs, optical Fourier transform, and Hough transform. Moreover, Pourdeyhimi et al. [83, 90, 91] accomplished some comprehensive studies on pore size characterizing and fiber diameter distribution measuring in nonwovens. Online characterization of fabric compression behavior (fabric stress-strain relation) was done by Huang [37]. An in-situ prototype measurement system was constructed and instrumented to extract the desired experimental data during the fabric deformation. Several well-established approaches, including statistical, empirical, and continuum concepts in compression behavior of fiber networks were reviewed and compared in Huang's PhD thesis.

Perrin et al. [78] developed a novel procedure to determine the fiber Young's modulus of elasticity. The method was based on the dependency of the elastic modulus to the resonance frequency of oscillations of fibers for different modes. They assumed that the fiber behaves as an Euler-Bernoulli beam with circular cross section and applied classical beam theory in order to relate its modulus of elasticity to resonant frequency, density, and dimensions of the fiber. The dimensions of fibers were obtained by optical and scanning electron microscopy. They constructed and instrumented an experimental set up in which individual fibers of various lengths were mounted on a polymeric support to resemble a cantilever beam with vibrating support. An adhesive was utilized to position around the fiber mounting to enhance its rigidity at the point of contact. The support was attached to a vibrating platform of an electrodynamic shaker capable of producing oscillations with required frequency.

2.2 Micromechanical modeling of nonwoven fiber masses

2.2.1 Statistical micromechanical approaches

To adopt a micromechanical model for fiber assemblies, statistical and probabilistic approaches such as averaging and homogenization are the most common tools utilized in developing the structure of such random networks. In most micromechanical models, a homogeneous discrete continuum consisting of fibers and void space is considered and then a continuum mechanics approach is utilized, assuming that the constituent fibers are the only load-bearing phase in the network under macroscopic loads. The most famous and pioneering work in micromechanical modeling of three-dimensional random fiber networks has been done by van Wyk [115]. In his notable development in compression behavior of fiber assemblies, he assumed that bending of the fibers is the predominant deformation process in comparison to the other modes of fiber deformation such as extension, compression, and torsion. He considered the structure as a system of straight fiber beam elements, which are located in different layers of the assembly, supported by two adjacent fiber contact points and developed a power relation between pressure and volume fraction of the fiber mass at macroscale as follows:

$$P(v_f) = k_p E(v_f^3 - v_{f0}^3) \tag{2.1}$$

in which $P(v_f)$ is the pressure on the sample, E is fiber Young's modulus of elasticity, v_f is the fiber volume fraction defined as

$$v_f = \frac{v}{V} \quad \Rightarrow \quad v_f = \frac{v_{f0}}{1+\epsilon} \tag{2.2}$$

where v is fiber volume in the network, V is volume of the assembly, v_{f0} is the initial volume fraction for which pressure on the structure is considered to be zero, ϵ is the engineering strain, and k_p is a statistical constant accounting for all uncertainties considered in the formulation, including direction and location of the contact force on fibers, the deformation direction, and ignoring the crimp of fibers. Mean free fiber length (defined as the distance between two neighboring contact points), elasticity of the constituent fibers, and density of the assembly were the main structural parameters that governed the compression behavior of the network. In evaluating mean free fiber length, van Wyk used two statistical methods to obtain the number of contact points as well as the distance between them. It was the most determinant parameter in the relation that provided a wide source for further research.

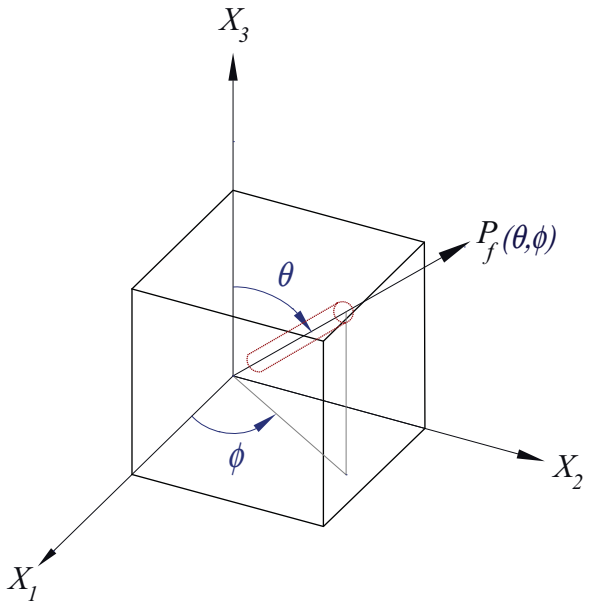

Figure 2.1: A representative volume element along with a random fiber.

Neglecting the frictional forces, increases in number of contacts during deformation, fiber crimp, the distribution of fiber length and diameter, and compression-induced orientation were the main concepts considered in the theory.

Komori and Makishima [52] presented a novel idea for estimating the numbers of fiber-to-fiber contacts in general fiber assemblies, with any arbitrary fiber bends, cross sections, and distribution of orientation and length. The method was based on the concept of spatial density of fiber orientation and probabilistic principles. They assumed that all the free fiber segments are straight cylinders of equal diameters and defined the position of a typical fiber in space by polar and azimuthal angles as shown in Figure 2.1. Hence, the orientation space could be spanned by a pair of configuration variables (θ, ϕ), provided that $(\theta, \phi) \in [0, \pi]$. Fiber networks could be distinguished by introducing fiber orientation distribution function $\Omega(\theta, \phi)$, which satisfies the normalization condition over the orientation space. They set up a geometrical model and evaluated the probability in which two fibers are in contact with each other, then extended it into the average number of fibers that contact a typical fiber. Based on the statistical computations, they showed that the total number of fiber contacts in such imaginary fiber assemblies, N, would be

$$N = \frac{d_f l_f^2}{V} \iiiint_A \sin \hat{\kappa}_{(\theta,\phi;\theta',\phi')} \Omega(\theta,\phi) \sin\theta \, \sin\theta' \, \mathrm{d}\theta \, \mathrm{d}\phi \, \mathrm{d}\theta' \, \mathrm{d}\phi' \tag{2.3}$$

where $\hat{\kappa}_{(\theta,\phi;\theta',\phi')}$ is the angle between axes of a couple of fibers with orientations (θ, ϕ) and (θ', ϕ'), d_f is the fiber diameter, A is the region of integration spanned by fiber rotation angle over the orientation space, and l_f is the total length of fiber in the assembly. They presented a method of geometrical probability in another work [53], developed to estimate the density function of fiber orientation and length in a general fiber assembly. The distribution of fiber length was assumed to be arbitrary based on their previous work.

It is logically conceivable that fiber orientation in the assembly at microscale depends on the deformation of the network at macroscale. As a matter of fact, a correlation between strain and orientation distribution functions can be observed by several methods such as electron microscopy or in-situ mechanical experiments, especially in extensive compression schemes. Relying upon the inevitable physical phenomenon, Komori and Itoh [47] presented a formula in differential form that could describe the change in direction distribution induced by compression. Accordingly, an orientation-dependent mean free fiber length could be calculated. In the evolution of orientation distribution, they assumed the affine deformation rule in which the projection of the bending element onto any axes is deformed similar to the dimension of the mass itself. They also made some other assumptions to develop their theory:

1. There is no slippage between fibers, i.e. no energy dissipated during deformation.
2. Fibers are assumed to be initially straight and of the same length.
3. No new contact will be generated during incremental deformation.
4. The shape of the deformed fiber under compression can be estimated by an arc line.
5. Shear deformation in the fiber network can be ignored.

They obtained the mechanical stress-strain relation based upon an energy method, then applied the developed framework for a random fiber mass in different compression schemes like isotropic compression, laterally confined compression, and simple compression. They treated only compression without shear deformation, so all off-diagonal components in the stress-strain tensors are zero. Komori and Itoh interpreted the fibrous assembly as a continuum and assumed affine deformations for elemental response of the individual

straight fibers. This means that a rectangular prism whose diagonal is spanned by a fiber segment is deformed similarly to the assembly itself, at a sufficiently small macroscopic scale below which the fiberweb volume elements are discrete and inhomogeneous in structure [47]. Theoretical development behind the continuum approach first assumes that displacement of consecutive contact points on any fiber segment is a result of applied assembly strains, determinable under the affine deformation model. Then, these fiber segments are assumed to deform into circular arcs, between neighboring contact points, in a way that preserves their initial length. From this deformation geometry, the energy density stored in a single elastic unit bent into a constant curvature can be computed and summed up over all units to give the total strain energy density of the fiber mass. The partial derivative of this total energy density with respect to the assembly strain applied along any reference direction then gives the assembly stress developed along the same direction.

In the estimation of number of fiber contacts presented by Komori et al. [52], decrease in the probability of contact between two fibers due to preceding contacts with other fibers has not been considered. In other words, they incorrectly assumed an independent and equal probability of making contact in contact formation of the fibers with a specific fiber. The number of contact points due to the misconception will be too high in the model and leads to much shorter mean free fiber length, which subsequently results comparable error in the prediction of compression modulus of the fiber network. Carnaby and Pan [14] also noticed the problem of higher macroscopic compression modulus in comparison to experiments, which could be due to overestimation of number of fiber contacts. Accordingly, Pan [76] presented a modification on the number of fiber-to-fiber contacts, considering that fibers that are already in contact with a typical fiber occupy a proportion of the fiber length, so diminishing the chance of contact by a new fiber. However, there were some mathematical mistakes in developing the formulation, questioned by Komori and Itoh [50], a year later. Pan applied the modified theory in microstructural analysis of different fiber assemblies, including perfectly random spatial and plane structures and ideally twisted yarn. In 1994, Komori and Itoh [50] modified their former theory [52] by introducing steric hindrance between fibers, in which the effects of forbidden length and forbidden volume between fibers were considered. The first one diminished the chance of contact by restricting the free fiber length on which a new contact may be formed and the latter enhanced it by narrowing the free volume in the mass where a fiber can be located without touching the contact parts formed earlier [50]. Including these effects led to defining the basic fiber segments that could be treated as independent statistical elements. Using the steric exclusion concepts, they modified the probability of contacts between two fibers by introducing the hindrance factor.

Neckář [73] revised van Wyk's model by excluding the incompressible areas between

contact points in bearing macroscopic loads on the network. His theory was based on the fact that fiber contacts occupy a specific volume of the assembly which can not perform as a structural energy element to absorb the energy flow into the network; in other words, these contact volumes are forbidden volumes for bending of the fibers. Physically, since the fibers in the contact volumes cannot bend, these volumes should be excluded from the total volume resisting macroscopic pressure, as reformulated by Neckář:

$$P(V) = k_p E v^3 \left(\frac{1}{(V - W)^3} - \frac{1}{(V_0 - W_0)^3} \right) \tag{2.4}$$

in which W is the volume occupied by all the fiber contact points and the zero indices show the initial or zero stress state. It can be expressed in terms of volume fraction as:

$$P(v_f) = \frac{k_p E v_f^3}{\left(1 - \frac{v_f^3}{v_{f,m}^3}\right)^3} - \frac{k_p E v_{f0}^3}{\left(1 - \frac{v_{f0}^3}{v_{f,m}^3}\right)^3} \tag{2.5}$$

where $v_{f,m}$ is the critical volume fraction that is defined as the volume of the assembly when all air is squeezed out of the network, so behaves similar to a solid block. In developing the relation from equation 2.4, Neckář assumed that contact volume fraction w_f, which is defined as the volume of the fiber in all contact volumes divided by all contact volumes, is equal to critical volume fraction $v_{f,m}$; he did not explain the reason for this selection. Stamm [100] modified Neckář's theory by defining a target region for w_f, when attempting to get reasonable results for compressional behavior of some specific types of felt with relatively high volume fraction, for which the current models did not work well.

Compression analysis of nonwovens, in which the bending units are assumed to be curved beams, was studied by several researchers to generalize the former approach that the fiber elements were straight. Lee and Carnaby [56,57] established a theory to determine the energy developed within a wool fiber mass based on the energy stored in the fibers from changes in the curvature of the fiber. Lee et al. were not concerned with calculating the stress-strain response of the mass but rather sought to explore the influence of certain parameters on the compressional energy of the fiber assembly. They related the change in the curvature of a fiber, deformed from state 1 to 2, as shown in Figure 2.2, to the applied external uniaxial strain through the affine assumption. The change in curvature was determined from the chord lengths, b_1 and b_2, and total fiber lengths L_1 and L_2. They established a criterion to determine if a fiber would undergo bending, straightening, or slipping. The energy for each of these deformations could then be calculated based

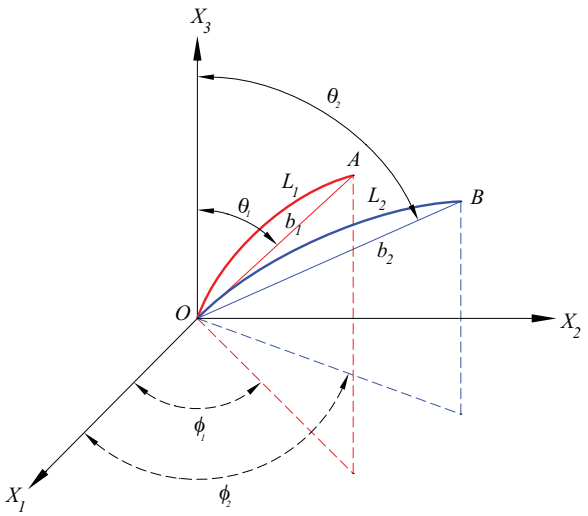

Figure 2.2: General deformation of a typical fiber (red is the initial state and blue is the deformed state).

on the fiber curvature. The total energy, Ψ, of the system equals the summation of all energy associated with the number of fibers undergoing bending, N_B, straightening, N_T, and slipping, N_S i.e.

$$\Psi = \sum_{i=1}^{N_B} E_{Bi} + \sum_{i=1}^{N_t} E_{Ti} + \sum_{i=1}^{N_S} E_{Si} \tag{2.6}$$

in which E_{Bi}, E_{Ti} , and E_{Si}, are structural energy stored in fibers due to bending, straightening, and slipping of the fibers respectively. Lee et al. [57] then minimized the energy for a given applied strain and Poisson's ratio to explore the effect of certain parameters on the developed compressional energy. A gamma distribution representing the distribution of fiber segment length and the fiber segment curvature was characterized, relating the crimp and the effective diameter of the crimped fiber configuration. Since the model was based on the relative change in the fiber segment curvature, the effect of initial curvature, or crimp, of the fibers in the overall behavior of the fiber network had been considered. They found the fibers with increased crimp resulted in a bulkier mass, so required greater energy to compress. Likewise, an increase in fiber density resulted in a higher required compressional energy. They also pointed out that the elastic energy tended to decrease with fiber diameter increase, but believed that further bivariate studies were necessary to determined more meaningful correlations between fiber mass properties and the bulk

behavior. In attempting to include crimp of the fiber segments, Komori et al. [49] defined the straight-line segment connecting the ends of the free length as the "skeleton" of a fiber segment. They further assumed that all the fiber elements whose skeletons are oriented equally along vector OA have the same length $b1$, the orientation-dependent mean free fiber length. Using the developed theories in their former work [47], they calculated the incremental energy along all the skeletons within a unit volume to evaluate the macroscopic stress, as obtained in the straight beam model.

In 1995, Toll and Manson [111] presented a constitutive equation for a statistically homogeneous planar fiber network under compression. They considered the fiber network as a layered system with fiber bending deflection between neighboring contacts, while no elongation, contraction, or torsion were involved. To have a positive-definite strain energy function in constructing their formulation, they had to merely consider elastic deformations, ignoring sliding and inelastic dissipation between fibers. They defined a node as a fiber segment that deflects between two supporting fibers, spaced at distance a apart, under the load of a third fiber, then characterized it towards evaluating the strain energy function as:

$$s = \frac{\mathrm{d}\delta_n}{\mathrm{d}p_c} \quad \Longrightarrow \quad \mathrm{d}U = \eta_n \frac{\overline{ps}}{\overline{s}} \overline{\mathrm{d}\delta_n} \tag{2.7}$$

which depends on geometry of the fiber segment and the end conditions at supporting points. In equation 2.7, s is the nodal compliance, p_c is the nodal force, δ_n is the node deflection, U is the stain energy function, η_n is the node density, and the overbar denotes the average value of the nonuniform parameters. Toll et al. assumed that on incremental compression of the assembly, the increase in uniaxial macroscopic pressure is evenly distributed among the existing nodes at the time. They derived the strain energy function, relying on the fact that the average incremental node deflection can be expressed in terms of average nodal compliance. The obtained stress-strain relation, derived from the energy function, was in term of the average node properties $\overline{s}(v_f)$ and $\overline{s}(a_f)$ that were functions of volume fraction (strain). For compliance estimation, they assumed a cylindrical beam supported with a no-rotation condition at each end and loaded at the midsection; for node spacing they utilized Toll's previous work [109] on the exact calculation of fiber contacts, also mentioned later in another paper [110]. They assumed the contact points along a fiber to be spaced at random, and modeled the contact points spacing by an exponential distribution. Finally, a linear relation between macroscopic applied pressure P and fifth power of volume fraction was obtained for planar fiber networks:

$$P(v_f) = \frac{512}{5\pi^4} E f^4 (v_f^5 - v_{f0}^5), \tag{2.8}$$

in which f is the orientation structural tensor as defined in equation 3.45

In continuum mechanics of solids, constitutive relations are used to establish mathematical expressions among the static and kinematic variables that describe the mechanical behavior of a material when subjected to applied loads. Narter et al. [72] developed a 3D model in which the elastic constants of anisotropic dense fiberwebs can be evaluated in terms of fiber linear density, fiber elastic modulus, fabric bulk density, and the spherical harmonic coefficients of direction distribution function. They further argued that when the assembly possessed symmetry about one or more reference planes of axes, the obtained relationship could be simplified, removing spherical-harmonic coefficients from the constitutive equations. They used the mechanistic approach introduced by Cox [17] and assumed the free fiber segments to be nearly straight, in the order of several fiber diameters, in case of dense fiber networks. They acknowledged Hamlen's findings on seeking dominant elemental deformation modes in bonded fiber networks, which was based on three-dimensional computer simulations along with matrix methods of structural analysis. Hamlen's research work revealed that fiber extension was the leading deformation scheme for both fibers and bonds, when compared to shear and bending deformations, in bearing macroscopic load on the fiber mass. Based on that, they established their micromechanical theory based on axial deformation of fiber elements and orientation of fiber segments, considering an imaginary fiber network in which slippage at contact points can be ignored due to a high coefficient of friction or firmly-bonded fibers as in woolen felt.

Rawal [92] developed a modified micromechanical model to study tensile behavior of needle-punched and thermally bonded nonwoven fiberwebs. The effect of the geometrical configuration of fibers, such as curl factor and fiber orientation angle, on the mechanical behavior of nonwoven structures was studies. By introducing the fiber curl factor and its distribution, defined as the relative frequency of the fibers having the same curl factor, along with relating the amount of extension in a typical fiber with specific orientation and curl factor to the web incremental extension, the stress-strain constitutive equations for the network were acquired. He presumed a nonlinear relation between stress and strain of the fibers, then extended it to the stress in each web layer according to the number of fibers in that layer. In addition, the distribution of fiber orientation within a nonwoven structure was estimated using Fourier series with which the analytical solutions for mechanical behavior of the fiber assemblies were derived.

In 2009, Rawal [93] examined the theory of compression in formulating the mechani-

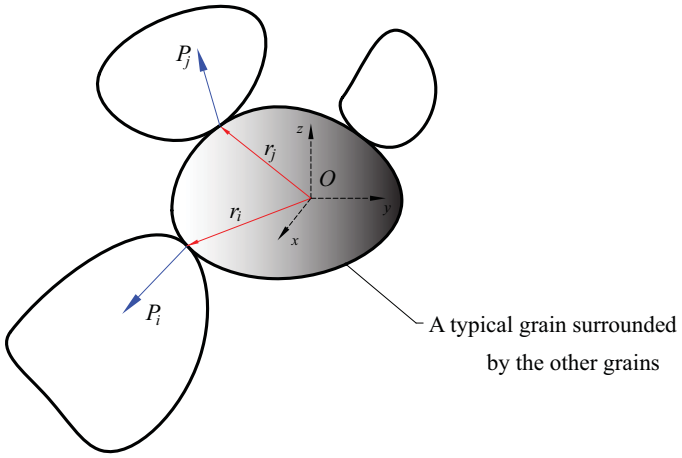

Figure 2.3: A schematic of a typical granular medium.

cal response of thermal bonded nonwoven networks to compression loading schemes. He developed a simple mechanistic model based on current models to study micromechanical behavior of two-dimensional thermally-bounded nonwovens. In the model, the basic fiber parameters and network properties were incorporated, including fiber volume fraction, proportion of free fiber length between two bonds, fiber modulus, and the orientation configuration of fibers. Furthermore, Rawal et al. [96] studied the morphological behavior of nonwoven fiber networks under compression in terms of of fiber orientation, fiber volume fraction, number of fiber-to-fiber contacts, distance between the contacts, porosity, and pore size distribution. They performed some experiments to validate pore size distribution obtained theoretically by updating the structural and morphological parameters of the thermally bonded nonwoven materials.

Alkhagen and Toll [1] developed a constitutive relation for a fiber mass using the rate theory of flexible granular solids. As illustrated in Figure 2.3, a granular solid consists of solid particles that interact by mechanical contacts. The macroscopic load on the assembly will be transferred across surfaces of contact between neighboring particles. A given particle is thus subjected to a Hertzian distribution of contact stresses over its contact surfaces. However, as long as the linear dimension of the contact surface is small compared to the distance between these surfaces, those surface tractions can be represented as pointwise acting forces. To be appropriate in modeling fiber networks, the assembly can thus be represented as a finite number of contact points interconnected by deformation units. The equilibrium conditions on each particle can be expressed as (refer to Figure 2.3)

$$\sum \boldsymbol{P} = \boldsymbol{0} \quad \text{and} \quad \sum \boldsymbol{r} \times \boldsymbol{P} = \boldsymbol{0} \tag{2.9}$$

where the summations are taken over all contact points of a particle. The theory is based on the affine average motion of interparticle contact points. In the model, bending and torsion of fibers were considered as structural deformation mechanisms, so it could also cover a large deformation range. According to fundamental concepts in granular materials theory, the strain energy function in the granular solids is strain path-dependent, still recovers all the energy in unloading, which signifies the lack of frictional slip dissipation in the medium. It reflects the hypoelastic behavior of the granular materials, so should be teated using a rate theory. To utilize the formulation for a fiber mass, constituent fibers were considered as particles that interact by mechanical contact; therefore, all stress will be transmitted through the assembly across contact interfaces. Alkhagen and Toll developed the differential equation governing the compression behavior of fiber assemblies in terms of structural tensors and basic properties of fibers such as volume fraction, Young's modulus of elasticity, and crimp ratio.

In another work [2], Alkhagen et al. discussed the effect of fiber diameter distribution on the elasticity of a fiber mass, applying the same statistical mechanics of bending and torsion of fiber segments as in their former paper. Statistical tools were utilized in order to account for a distribution of fiber diameters rather than just a single diameter, as assumed in their previous work. They accomplished uniaxial compressibility experiments on several fiberwebs with different bimodal fiber diameter distributions and compared to model predictions.

2.2.2 Microstructural models

Finite element approach has been gaining a widespread attention in various field of engineering; from structural mechanics and fluid dynamics to aeronautics and biomechanics. FEM, also known as finite element analysis (FEA), is a numerical technique for finding approximate solutions of partial differential equations in which the continuum will be discretized into a set of discrete sub-domains, then analyzed by mathematical formalism of the method.

Wu and Dzenis [120] proposed a model for estimating the elasticity of planar fiber networks in which linearly elastic straight rods, bonded rigidly at contacts, were dispersed evenly throughout the structure of the fiberweb, adopting a random arrangement process. Including fiber bending, elongation, and contraction, a constitutive model was developed

based on the strain energy dissipated by all possible fiber deformations in all directions. They performed a finite element method (FEM) analysis and compared the results obtained with the explicit expressions for the effective stiffness of random fiber networks.

Beil and Roberts applied the finite elements methods in creating a spatial micromechanical model based on general theory of the bending and twisting of thin rods [63]. Vector differential equations for the model were acquired from conservation of linear and angular momenta, derived respectively from a force and moment balance on a small segment of fiber. Fiber segments, which assumed to be a portion of a helix, were distributed randomly in the representative elementary volume. Crimp of the fibers could be controlled by helix radius while keeping the helix period unchanged. Interactions between fibers was simulated by repulsion forces normal to the centerlines of the contacting fibers and frictional forces, acted perpendicular to the normal forces, preventing fibers sliding. They used finite difference approximation to obtain a nonlinear system of algebraic equations along with appropriate boundary conditions to perform numerical simulation. Afterwards, they compared the simulation results with experiments and particularly van Wyk's model in which idealized bending elements played a key role in developing his mechanistic novel approach. In another research work [8], they used the same approach in the former paper to study the effect of fiber crimp, hysteresis, and fiber orientation in uniaxial compression behavior of spatial random fiberwebs.

Sherburn [98] accomplished a finite element method in studying mechanical behavior of textiles. He employed a multi scale (microscopic, mesoscopic and macroscopic) modeling approach in predicting mechanical properties of such fiber networks. Characterizing the geometry of the fiber assembly was a significant part of the research work. He considered yarn path as being defined by a series of nodes along with various cross sections for the constituent fibers. To validate the proposed theory, optical microscopy and scanning electron microscopy along with microtomography were utilized to extract three-dimensional volumetric data of the fabrics.

A comprehensive finite element model of cellulose fiber fluff, including generation and analysis of the network geometry, was accomplished by Heyden [34] in her doctoral thesis. Mechanical performance of the simulated bonded network, consisting of random-oriented fibers with arbitrary distribution in length, curvature, cross-section, stiffness and strength, was investigated based on microscale properties of the network. Sliding and non-sliding (stick-slip) conditions between contact points were established using non-linear coupling elements to simulate fiber interfaces bonds in the assembly. The fibers were modeled as beam elements in the finite element analysis and distributed randomly in the network with periodic boundary conditions; this enabled the study of the network to be confined to a unit cell with limited number of fibers. A systematic analysis was utilized to predict

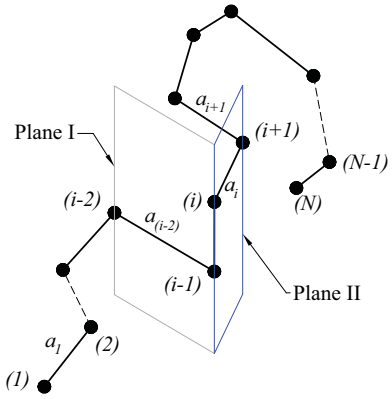

Figure 2.4: Schematic of a typical fiber modeled as a polymer chain.

geometric properties such as number of fiber contacts in the network.

Recently, Molecular Dynamics (MD), which can be categorized in energy-based techniques, has been widely used in modeling fiber assemblies. In addition to versatility, the advantage of being easy to implement along with creating high fidelity simulations makes molecular dynamics an appropriate approach to model polymer chains and biological membranes. Similarity in structures, as well as the capacity of interchanging structural forces (such as bending or torsion) and mutual interaction forces in molecular dynamics with that of in fiber masses, seems to be technically enough to apply molecular dynamics in simulating micromechanical behavior of fiber networks. Molecular dynamic simulations have been used widely in modeling entangled polymer chains [9, 10] or recently in micromechanics of fibrous materials [5, 6, 43].

Járai-Szabó [43] focused in his masters research work on computer simulation of entangled materials. Every single fiber in the network was modeled as a *bead-spring* polymer chain in which segments are small enough to be considered as straight elements, confined between two end nodes (Figure 2.4). Stretching of the fiber segments was modeled by a linear spring between nodes. Structural bending and torsion of the fiber were included by applying torsion springs on the planes of bending and torsion between consecutive fiber segments connected at end nodes in the chain, as illustrated in Figure 2.4. Planes I and II are bending planes of the fiber segments by which the planes have been defined. The plane perpendicular to the line of intersection of those planes specify the plane of torsion for the fiber placed between nodes $i-1$ and i. Accordingly, the potential energy for the whole system, ignoring the effect of fiber torsion, can be written as

$$E = \sum_{c} \frac{K_S}{2} \left(1 - \frac{s_{i,i+1}}{l}\right)^2 + \sum_{c} \frac{K_B}{2} \left(\theta_i - \pi\right)^2 + \sum_{nc} -K_I \ln\left(\frac{r_{i,j}}{r_{cut}}\right) e^{\frac{r_{i,j}}{r_{i,j} - r_{cut}}} \tag{2.10}$$

where the first term accounts for elongation energy of the fiber between two consecutive nodes along its axis, i.e. resistance of the fiber either to traction or compression, in which K_S is the spring constant for the linear spring between two consecutive nodes, $s_{i,i+1}$ is the elongation between the two nodes, and l is the undeformed fiber segment length. The second term includes bending of the fibers, which can be acquired based on the change in the angle θ_i between fibers that define the planes I or II, e.g. fibers connecting nodes $i-1, i$ and $i, i+1$ in plane II, and K_B is the bending spring constant. The last term models interaction between non-consecutive fiber segments, considering a network of non-penetrating fibers. This term signifies an imaginary volume around the fiber to avoid crossing of the fibers, i.e. a non-penetrating assumption. Moreover, the potential would vanish smoothly at the cut-off radius by the particular definition of the function. $r_{i,j}$ is the distance between centerlines of two non-consecutive imaginary fibers and r_{cut} is the cut-off distance between the fibers centerline at which the fiber interaction threshold is defined, i.e. fibers at larger distance have no contribution in the potential function.

Gradients of the potential energies, reflecting structural and interaction energies of the fibers, leads to forces applied on each node. Consequently, the nodes displacement, so its trajectories are obtained in each simulation step based on an integration method applied to numerically solve the obtained Newton's equations of motion. For instance, a first-order Euler integration algorithm [43] or velocity-Verlet integration scheme [10] have been used widely as common techniques in molecular dynamics. However, the latter is more efficient and stable in physical systems at no additional computation cost [3, 119]. Recognizing the interactions within and between the fibers as well as the induced single fiber topology, e.g. random walk or straight fiber, are extremely beneficial in predicting macroscopic properties of the fiber mass.

The entangled network structure can be produced by placing a large number of polymer-like chains of fiber, obtained using a random walk process, in a random fashion inside the simulation control volume (a cube cell) with periodic boundary conditions and packing them as uniformly as possible. This can be useful in defining a network with more realistic, initially random, configuration. The packing process performs the Monte Carlo simulations of randomly chosen geometric transformation — chain translation, rotation, or reflection — on a randomly chosen polymer chain to achieve a desired homogeneity in the network [10]. It should be noted that the fibers are uniformly distributed inside the network without any

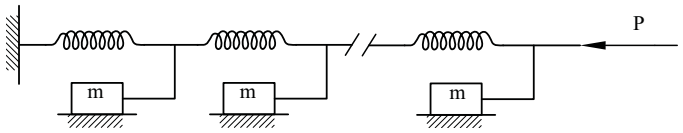

Figure 2.5: Schematic of Dunlop's rheological system in hysteresis modeling.

physical constraints on the fiber interpenetration. So, physically-inconsistent fiber overlap which would result in numerical instability have to be eliminated in an initial relaxation process. This is done by applying a pre-equilibrium molecular dynamic simulation in which the repulsive potential expression is replaced by a modified version with significantly less energy.

Barbier et al. [6] employed an alternative repulsive potential $\sum_{nc} \frac{K_I}{2} H(d_f - r_{i,j}) \left(1 - \frac{r_{i,j}}{d_f}\right)^{5/2}$, known as Hertz potential, that acts between non-consecutive springs when their distance becomes less than the fiber diameter d_f; it is implied by the Heaviside step function $H(x)$. $r_{i,j}$ is the distance between centerlines of two non-consecutive springs. To include hysteresis at the microscale, a Coulomb-like friction model was implemented at contact points to estimate sliding between fibers, i.e. a frictional force with a norm equal to the repulsive normal force between fibers multiplied by a friction coefficient. It was applied in the plane perpendicular to the repulsive normal force with a direction opposite to the relative velocity of the considered spring with respect to the other contact spring.

2.2.3 Hysteresis, anelasticity and stress relaxation

Dunlop [23] introduced three rheological models to capture the essence of the hysteresis phenomenon and irreversible deformation observed in his experimental work. The most successful model incorporated a series of elements composed of a nonlinear spring and a block sliding on a surface with Coulomb friction as shown in Figure 2.5. A slightly different series model was also considered, but did not capture the hysteresis effect smoothly. However it did do a better job of capturing the irreversible deformation that occurs during the first cycle. Although these models did reproduce hysteresis curves, based on dry friction in compression behavior of the network materials, they did not correlate the hysteresis loss directly to the individual fiber properties.

Stamm [100] utilized Dunlop's model for a typical fiber assembly (woolen felt) and showed that applying a more realistic spring equation in the model could fit experimental data better than using spring models developed by van Wyk or Neckář [73, 115]. According to the experimental results conducted on typical felts, he noticed that hysteresis in

consequent cycles do not follow the same loops, and that it shifts slightly depending on deformation velocities and relaxation times between loading cycles. This phenomenon, which is called hysteresis creep, was modeled by adding a Kelvin deformation model to Dunlop's model.

Carnaby and Pan [14] incorporated the fiber-fiber slippage in the deformation of fiber assemblies in both compression and recovery cycles. This provided the requirements to predict full hysteresis curves for compression and recovery stages, involving microscale properties of the network. They divided the contact points in the network into two categories, slipping and non-slipping, based on the Coulomb friction criterion and critical slipping angle. Carnaby and Pan used all the assumptions previously used by Lee and Lee [60] in structural force-deformation relations at microscopic level. It is to be noted that they ignored the effect of slipping contacts on the nonslipping contacts in developing the model. Referring to single fiber withdrawal experiments and theory [13,31,32,54], they argued that even in the absence of any external load applied to a mass of fibers, there were still significant nonzero contact forces between fibers in the assembly. This prevent the fibers from recovering to their lowest energy configuration because of mutual interference and frictional restraints to slippage [14] .

In 2006, Kabla and Mahadevan [45] investigated nonlinear behavior of low density soft fibrous networks. They believed that the mechanical response of the naturally curved constituent fibers under tensile load schemes is dominated by the unbending of the curved region. They set up experiments to characterize the geometry and mechanical response of the individual fibers in the felt. The fiber was estimated by a slender filament with a non-zero natural curvature, then a theoretical model was developed for the geometrically nonlinear deformations of the fiber based on the theory of elastica. In macroscale, they assumed a unit cell with minimal network connectivity inspired by similar models in polymer physics and developed a model to study the collective behavior of the network.

Stress relaxation occurs when fiber networks are exposed to constant deformation. When the load is low, some textile materials show an elastic and viscoelastic deformation. Elastic deformation is completely recoverable after loading and viscoelastic deformation is recoverable over time. The rate of decrease of stress is different during stress relaxation process, especially at the start point of relaxation, it is much greater than after a specific time interval [116]. This viscoelastic behavior of the material with respect to loading can be described using mechanistic models consisting of spring and dashpot elements. The spring represents the elastic properties of a linear solid material, whereas the dashpot represents the viscose properties of liquids. Mechanistic models can be obtained with different combinations of these basic elements, representing time-dependent nonlinear behavior of the fiber networks under compression loading schemes. Liu et al. [62] studied the stress-

relaxation behavior of wool fibers after a pretreatment with a chemical solution. They used different Maxwell deformation models to include various relaxation processes that govern the behavior of wool fibers under constant strain. To verify the feasibility of the models, stress-relaxation experiments for wool fibers were performed. Šajn et al. [116] presented some mechanistic models to study the stress relaxation behavior in fabrics with increased elasticity. Seeking to find the best model for predicting stress relaxation behavior in fabrics, they examined different well-established models such as Maxwell's models and Alfrey's model and introduced a modified Maxwell's model. The three-component Maxwell's model with parallel-connected nonlinear springs showed the best agreement compared to the experimental relaxation curve.

Dynamic properties of felt pads were investigated by Dunlop [24]. He measured the dynamic modulus and damping loss of the fiber mass using a reaction mass vibrating system in which the felt pad was statically loaded and then driven by small amplitude of vibrations. The dynamic modulus obtained from response curves was larger than the corresponding static modulus. Furthermore, he reported smaller dynamic modulus for greater vibration amplitude.

Stulov [103–107] conducted several investigations on theoretical and experimental modeling in estimating dynamic behavior and mechanical features of wool felt. Based on the obtained results, he developed a nonlinear hysteretic model for compression behavior of a typical piano hammer felt. In his piano hammer felt model [103], a static felt model was developed based on introducing the geometrical domain of interaction between hammer and string and calculating the deformation energy of the interpenetrated volume of felt. He assumed that this energy was concentrated mainly on the region of interaction between these two cylindrical bodies and was constant over the volume of interaction. These assumptions enabled him to calculated the amount of force needed to reproduce this energy. Assuming that the hammer felt is a microstructure material possessing history-dependent properties, Stulov [104–106] proposed two different mathematical hysteretic models and evaluated them in describing dynamic behavior of the hammer felt experimentally. In the first integral-form four-parameter hereditary model represented by equation 2.11, instantaneous stiffness F_0 and compliance nonlinearity exponent $\hat{J}$ were the elastic parameters of the felt, and hysteresis amplitude $\imath$ and the relaxation time τ_0 were hereditary parameters.

$$F(\varepsilon_p(t)) = F_0 \left[\varepsilon_p^{\hat{J}}(t) - \frac{\imath}{\tau_0} \int_0^t \varepsilon_p^{\hat{J}}(\xi) \exp\left(\frac{\xi - t}{\tau_0} \right) \mathrm{d}\xi \right] \tag{2.11}$$

$F(\varepsilon_p(t))$ is the force exerted by hammer in terms of felt compression ε_p. The parameters for the second differential-form three-parameter model, equation 2.12, were static hammer

stiffness F_0, compliance nonlinearity exponent $\hat{J}$, and the retarded time parameter $\hat{\alpha}$. The influence of string diameter on the hammer parameters and also humidity on the dynamic force-compression behavior of the felt were studied in those works.

$$F(\varepsilon_p(t)) = F_0 \left[\varepsilon_p^{\hat{J}}(t) + \hat{\alpha} \frac{\mathrm{d}(\varepsilon_p^{\hat{J}}(t))}{\mathrm{d}t} \right] \tag{2.12}$$

2.3 Multibody dynamics of piano action mechanisms

Theoretical

In 1921, Pfeiffer [79] conducted an analytical kinematic and kinetic analysis of the dynamic behavior of various piano actions and components. A decade later, in 1937, Matveev and Rimsky-Korsakov [68] introduced an abstract design of the piano action in which the whole action was modeled by a one-dimensional mechanism consisting of two masses: a key and a whippen assembly that interacts with the hammer through a spring. To be applicable for the upright piano action, Oledzki [75] improved the dynamic model proposed by Matveev and Rimsky-Korsakov, allowing the mass of the key to vary with the key position. A more sophisticated two-body model was presented by Topper and Wills [112] in which the key interacts with the hammer through whippen, which was modeled with a spring. To increase the fidelity of the model, they estimated the model parameters by direct measurements of the action components. Gillespie [27] developed a four-body dynamic model consisting of the key, whippen, jack, and hammer as kinematically constrained rigid bodies. He extended the model in another research work [28], including some contact effects from friction, damping, and compliance, gave reasonable agreement with experimental observations of a real action. However, as with previous models, the parameters could not be derived successfully through physical measurement and these had to be adjusted arbitrarily to achieve a realistic response. Van den Berghe, de Moor, and Minten [19] applied Newton-Euler equations in constructing a complex bond graph model of grand piano action dynamics with component bodies represented by macros interacting through dampers and springs.

Recently, in 2006, Hirschkorn et al. [35, 36] developed a dynamic model of a grand piano action, including all five main bodies in the action, and validated the simulated

model experimentally using a prototype model. Graph-theoretic modeling (GTM) was used in order to represent the interconnection topology of the bodies in the mechanistic model and to generate dynamic equations of motion. The procedure for symbolic equation formulation was automated using DynaFlexPro, software developed by MotionPro Inc. [42], running in a Maple environment [64]. Contact dynamics was included using a continuous model that relates the normal contact force between the bodies to the penetration depth and rate. The approach is similar to that of Hunt and Crossley [38] except that the power function is supplanted by a curve fit calculated from the specific load profile of each contact surface pair obtained experimentally. Hirschkorn's model was extended by Izadbakhsh et al. [40, 41], incorporating hammer shank flexibility into the dynamic model of the action. The effect of the more complicated component model on the motion of the other parts was studied and evaluated experimentally. The fidelity of the model was increased by using a revolute-prismatic joint for the key pivot to represent key lift-off, which is known to occur during the key stroke. Vyasarayani et al. [117, 118] coupled the piano action mechanism to a flexible string model, providing more realistic dynamics during and after the hammer impact than could be achieved with the previously used rigid stop. The partial differential equations for the string were combined with the ordinary differential equations of the mechanism to achieve the overall dynamic equations for whole system.

Including interaction between various components in the action requires studying different continuous contact models. Lankarani and Nikravesh [55] developed a continuous contact force model for impact analysis of multibody systems. The model was based on the general trend of the Hertz contact law in conjunction with a hysteretic damping function in which the unknown parameters are determined in terms of a coefficient of restitution and the impact velocity. Gilardi and Sharf [26] presented a literature survey on different contact dynamics modeling. This overview of impact and contact modeling methodologies described the general model principles, specifically the energy loss mechanism, friction model, and any accomplished experimental validation scenarios.

Experimental

There has been some systematic experimental researches into the grand piano action mechanisms in the past decades. Gillespie [28], and Gillespie and Cutkosky [29] constructed a grand piano model consisting of four main bodies using Kane's dynamics. Symbolic manipulation utilized for formulation of the equations of motion increased the ability of the model in the simulation of different action mechanisms. Under a known force applied on the key, the simulation results were compared with the experimental high-speed video recording. They utilized digitization techniques in extracting information regarding angular and

translational velocities of different bodies in the action.

Hirschkorn [35] accomplished a distinguished experimental work on the grand piano action including the five main bodies in the mechanism. The experimental setup was based around a keyboard from a Boston GP-178 grand piano action. As the actuation mechanism, he utilized a DC brushless rotary motor, a Kollmorgen MT308A1, attaching a small interchangeable aluminium arm to the output shaft to convert the rotary motion of the motor to linear motion on the key for small rotations. The motor was controlled by a "National Instruments PCI-7342 Motor Control" board to reproduce the inputs representing the general shape of a typical force input by a pianist measured at the key surface. A light Sensotec load cell was fastened to the key front to measure the force applied by the pianist and the actuator on the key. The rotary position measurements of the bodies in the system were done by a modular encoder system, the MicroE Systems, encoder optical sensors that were used in conjunction with different shaped scales. The encoders and scales were not physically connected, so there was no friction added to the system. In his experiments, the optical sensors were mounted on fixed stands, and only the small scales were attached to the bodies in the system.

Izadbakhsh et al. [40] introduced hammer shank flexibility and studied its effect on the motion of the other parts. They utilized a strain gauge for measuring the strain on the hammer shank, which is an octagonal wooden rod. According to the geometry, only a very narrow strain gauge could be mounted on one of the shank edges. To this end, the strain gauge type EA-06-062DN-350 from Intertechnology Inc. was employed. The strain gauge was incorporated in a Wheatstone bridge. Three passive 350-ohm resistors were added to the bridge to complete its electric circuit. The National Instruments SCXI-1520 signal conditioning module and PCI-6034E multifunction DAQ card were used for reading this strain gauge.

Stulov [103–106] conducted several investigations on theoretical and experimental modeling of dynamic behavior and mechanical features of wool felt. He applied the models in developing a nonlinear hysteretic model of piano hammers.

Masoudi et al. [65] constructed a multibody dynamic model of a typical vertical piano action using computerized symbol manipulation in the formulation of the equations of motion. All five main bodies in the action had been considered as rigid components and a rigid stop was utilized for hammer-ground contact point. Preliminary experimental results from high-speed video imaging were compared qualitatively with the simulation results.

Piano actuator mechanism

There has not been much research work on the modeling actuator mechanisms applied to duplicate pianist's finger force to the piano actions, particularly from dynamics and vibrations points of view. This is important to generate precisely repeatable input on the action prototype in multiple trials when studying experimental aspects of the piano action. Moreover, it should reflect the flexibility and damping properties of the pianist's finger as well as body reaction. To this end, some actuator mechanisms have been proposed, mostly consisting of an arm attached to a rotary motor using a hub. Particularly, Hirschkorn [35] constructed and instrumented such an actuator mechanism which has been utilized by some other researchers [40]. High-speed imaging from the actuator prototype revealed significant vibrations in the arm during the key stroke, which may affect the actual dynamic response of the action. This motivates the development of a dynamic model of the hub-beam actuator mechanism in which the arm flexibility possess a key role in replicating the real finger force profile.

Modeling flexible links using different dynamic criteria besides appropriate discretization methods has been noticed by many researchers in the past several decades, especially in robotics applications. Actuator model realism is enhanced by including an eccentric tip mass at the end of the flexible beam. Cai et al. [12] considered a dynamic system of a rigid hub and a flexible cantilever beam with a tip mass and characterized it based on Hamilton theory and FEM. The obtained equations included axial beam extension and the second-order coupling term, i.e. the axial shrinking quantity caused by transverse displacement. Chapnik et al. [15] utilized FEM in modeling a single-link flexible robotic arm, including the effects of beam damping and also hub inertia in the dynamic equations, then simulated the motion of the arm under impact loading. The dynamics of a radially rotating beam with impact was also studied by Yigit, Ulsoy, and Scott [121]. In their impact model, the vibration behavior of the system after impact was determined by the momentum balance method and a coefficient of restitution. In another paper [123] a different impact model based on Hertzian contact and damping was used to predict the rigid-body motion as well as the elastic motion of the arm during and after impact. In the both papers, the governing equations of motion were formulated by the extended Hamilton's principle and Euler-Bernoulli beam theory.

2.4 Chapter summary

In this chapter, several techniques for micromechanical modeling of fiber assemblies were examined; microstructural approaches in which the response of every single fiber is used to predict macroscale behavior of the network, and statistical micromechanical models that borrow statistical tools to estimate micromechanical response of the fiber mass, considering fiber bundles with same structural and physical characteristics. Theoretical ideas, experimental procedures, and technical tools in characterizing the structure of fiber networks were introduced. Well-approved statistical approaches in micromechanics of fiber assemblies, built on the number of fiber contacts in random structures, along with their performance in different applications were discussed. Molecular dynamics and finite element method were briefly described to illustrate their application in multibody dynamic simulations. Physical sources of hysteresis in compressive behavior of fiber networks, including several techniques in mechanistic and mathematical modeling of this irreversible phenomenon, were reviewed. Furthermore, previous works in multibody dynamic modeling of piano action mechanisms were summarized in this chapter, and technical works appropriate in modeling the actuator mechanism of the piano action, by which the pianist's finger force is replicated, were introduced.

Chapter 3

Hysteretic Micromechanical Modeling of Nonwoven Fiber Assemblies

Micromechanical behavior of fiber assemblies has been gaining widespread attention in extensive fields of engineering applications due to their unique properties. Specifically, textile industries, paper making companies, and composite material manufacturers are interested in estimating mechanical properties of such assemblies under various loading schemes. There have been various challenging issues in micromechanical modeling of nonwoven fiber assemblies: highly nonlinear compliance, nonlinear hysteretic phenomena, random network structure, complex morphologies, and dominant microstructural deformation schemes.

In micromechanical approaches, response of the fiber mass to external loads at the macro level is evaluated based on the reaction of its constitutive fibers at the micro level. To investigate macrostructural behavior of fiber assemblies properly and precisely, one has to characterize the network microscopically, including the way that the fibers are distributed in a typical control volume of a continuum media and interacting with other fibers, as well as mechanical and geometrical characteristics of each individual fiber. Hysteresis, stress relaxation, and anelasticity can be involved in more sophisticated models depending on the structure and type of the fiber network and its components.

Felt, as a typical fiber mass, is defined by Lehmberg [61] as "a fibrous material built up of interlocked wool fibers by mechanical and chemical action, moisture and heat". Due to its distinguished damping properties, felt has been used widely in contact between interacting bodies of mechanical systems. Musical instruments, particularly piano mechanisms, use

felt-covered contact interfaces in suppressing mechanical impact, vibrations, and the most tangibly, undesired noises from component wear and tear. There are numerous mechanistic models developed based on response of the fibers at the micro level, but none of them are suitable for studying compression behavior of felt [100]. The applicability of some more complicated recent theories to micromechanical modeling of felt will be extensively discussed.

In this chapter, the major focus is on studying compressive behavior of felt, considering the nonlinear compliance observed in both loading and unloading curves along with nonlinear hysteresis. The developed micromechanical model should be simplified enough to be applicable in multibody dynamic simulations, which is another key objective in this research. In other words, to keep the simulation time tractable in multibody dynamic models, interaction between components has to be modeled mechanistically, accurately, and still simplified enough so that in each step of simulation time, contact forces can be efficiently calculated as a function of penetration depth between colliding objects.

3.1 Geometrical microstructure of nonwovens

Generally speaking, the response of nonwoven fiber networks to prescribed loading schemes depends on geometrical and mechanical parameters of their structure and constituent fibers at the microscale. The shape, dimension, porosity, mechanical and surface properties of the fibers, as well as architectural parameters like the distribution of fiber segment length and fiber orientation, crimp, predominant deformation mechanisms, and type of fiber interaction — sliding or non-sliding contacts — are essential factors in determining the macroscopic response of the assembly.

In Section 3.1, the geometry and structure of felt will be visually analyzed using SEM images from a piano hammer felt at different scales. Afterwards, several established approaches are presented to estimating the number of fiber contacts, which is utilized in the calculation of mean free fiber length when parameterizing the virtual structure of the network. In addition, generating a random network consisting of straight fiber elements, distributed randomly over the orientation space, is explained at the end of this section.

3.1.1 SEM and structure characterization

Scanning Electron Microscopy (SEM), which has been an indispensable tool in a broad range of scientific and engineering applications since 1960, images the sample surface by

scanning it with a narrow high-energy beam of electrons. Topography of a very wide range of organic and inorganic materials, from nanometer (nm) to micrometer (μm) scale, can be characterized by SEM. One of the most valuable characteristics that makes SEM predominant, in comparison to other imaging instruments in that scale, is its capability in getting 3D images from the surface of a wide range of materials [30]. Secondary electrons and backscattered electrons, which are the most frequent signals produced from the interaction of finely focused electron beams with the sample, are the sources of information for the surface topography of the sample. Its ability to extract information in the third direction is due to the large depth of field along with the shadow relief effect of the secondary and backscattered electron contrast [30]. To have a better three-dimensional appearance useful for characterizing the surface architecture of the sample, a greater depth of field will be required.

Since the SEM specimen chamber is at high vacuum, the sample has to be clean, dry, and electronically conductive. In characterizing the structure of fiber assemblies, contaminants produced by the sample in such an environment will degrade image quality or damage the instrument. Moreover, nonconducting specimens will be electrostatically charged at the surface during the scanning process in SEM. There are several procedures to prevent the accumulation of charge in nonconducting samples; an option is to cover the surface of the sample with a very thin film, between 1 and 10 nm thick, of highly conductive material such as gold [30]. Sputter coating is the method used to apply such a coating layer. According to [30], in the sputtering method, "a negatively charged conductive metal target is bombarded by positive ions in a low-vacuum gas discharge and the eroded metal atoms land on the specimen surface".

3.1.2 Experimental results from scanning electron microscopy

Figure 3.1 shows SEM images at different scales for a typical felt sample. The acquired depth of field is acceptable for extracting information such as mean fiber diameter, mean free fiber length, or crimp ratio. Based on a superficial analysis from the images, the following results can be obtained:

1. The fibers are highly crimped and interlocked in some regions.
2. The fiber cross sections are not necessarily circular.
3. Assuming circular cross sections for fibers, the fiber diameters are not identical.

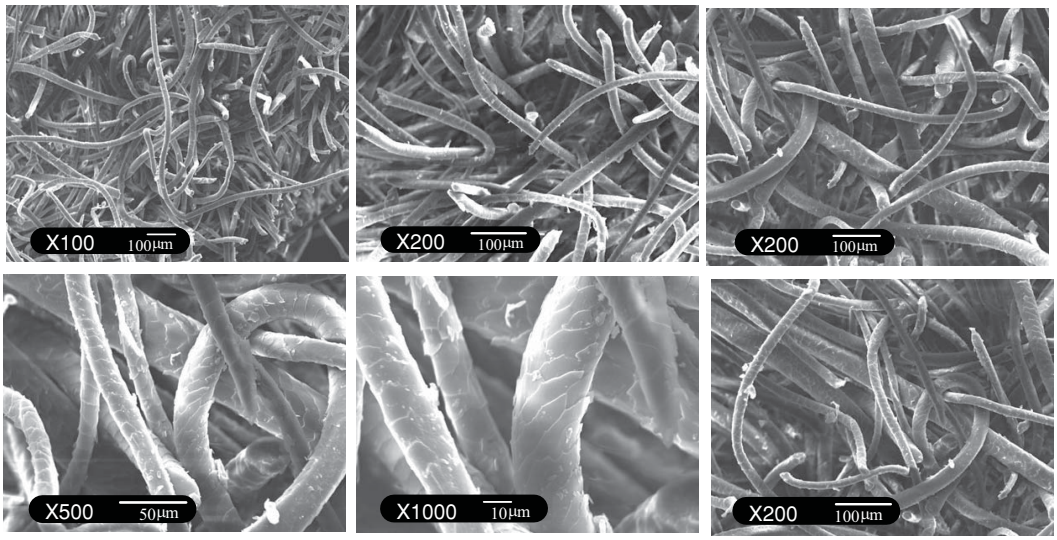

Figure 3.1: Scanning Electron Microscopy (SEM) of a typical gold-coated felt sample.

4. Fiber surface seems to be rough enough to cause considerable friction between interacting fibers.

5. The fibers are not dispersed evenly over the whole structure.

Estimating an orientation distribution function in nonwoven fiber assemblies can be done using different criteria such as Direct Tracking, Fourier Transform, and Flow Field Analysis. Image analysis tools are strong enough for evaluating the distribution of fiber length and diameter. However, characterizing behavior of felt during a deformation process needs tracing the response of the network dynamically. It can help us in finding the predominant elemental deformation modes or gradual changes in structural parameters during loading and unloading when the assembly is under repeated loading schemes. Performing in-situ testing on fiber networks using conventional SEM is currently impossible since the sample should be fixed to ensure that it does not move during image acquisition.

The other alternative would be Environmental Scanning Electron Microscopy (ESEM). Environmental SEM has several advantages over conventional SEM; the most explicit ones are [4]:

1. The sample can be conductive or nonconductive. In ESEM, gas ionization eliminates the charging artifact due to non-conductivity of the sample.

2. Contamination produced by the sample, especially samples like felt which are porous, will not damage the instrument or degrade the image quality.

3. ESEM can observe and record various deformation processes including compression, tension, and crack propagation, dynamically.

ESEM has been recently used to study the behavior of a typical fiber assembly under a dynamic deformation pattern, utilizing a micro-compression stage and considering the possibility of performing in-situ mechanical testing along with the visual observations [95]. It should be noted that these attempts are confined to the surface or outermost layers rather than the actual bulk of the assembly.

Such a quantitatively precise experimental analysis will be in itself a major research project; primarily, the current work is motivated towards a qualitative microstructural analysis of the network confined to the captured SEM images.

3.1.3 Theoretical architecture of random fiber networks

The crucial step in micromechanical analysis of fiber assemblies is to construct a network based on statistical and geometrical properties of the fiber mass.

There have been numerous microstructural models since van Wyk in 1946 introduced the possibility of developing a micromechanical prototype in his pioneering work [115], which was based on the bending of straight fibers in resisting macroscopic loads. The straight fibers were a portion of the long filaments between contact points of interacting fibers inside the whole network. Many researchers utilized this distinctive idea, and developed, expanded, and modified it to achieve a desired simulation fidelity. Particularly, the number of fiber to fiber contacts, distribution of fiber orientation, predominant deformation schemes, and geometrical shape of fibers have been the most influential topics to investigate.

Number of fiber contacts - Mean free fiber length

Independent of the deformation schemes considered for microstructural response of the network in bearing macroscopic loads, the mean free fiber length, which is defined as the fiber portion between two adjacent contact points, has a key role in representing the stress-strain relation. It is the number of fiber-to-fiber contacts that directly determines the mean length, so this number is studied in the first place.

van Wyk [115] proposed two procedures to determine the mean fiber element length, assuming that there is some length scale on which the fibers can be recognized as straight fiber elements. In such a phantom network, the fibers are disposed at random positions inside a control volume, to a prescribed volume fraction, but at orientations according to a statically homogeneous orientation distribution. Accordingly, the mean fiber length can be estimated by:

1. Considering the number of times that a vertically moving spherical particle of diameter d_f, equal to that of the fibers, encounter fibers with total length l_f, randomly dispersed in a vertical container of volume V and unit area of cross section. It results in:

$$\overline{\lambda} = \frac{2v_f}{\pi l_f d_f} \tag{3.1}$$

   in which $\overline{\lambda}$ is the mean distance between contact points, v_f is fiber volume fraction, d_f is fiber diameter, and l_f is the total fiber length in the assembly.

2. Placing a cylindrical tube of diameter $2d_f$ vertically in the container and counting the number of obstacles encountered by the spherical particle, which moves with its center along the axis of the tube, i.e. the total length of fiber passing through the tube divided by mean of fiber portions inside the tube. It will give

$$\overline{\lambda} = \frac{64v_f}{2\pi^3 l_f d_f} \tag{3.2}$$

van Wyk assumed straight fibers of uniform cross section; however, there are several generalized models for curved fibers and fibers with non-uniform cross sections [11, 49, 56, 57]. It is to be noted that mutual intersection is not considered in van Wyk's model when placing the fibers in the volume space of the network, i.e. the number of contacts in the network of non-penetrating fibers had been estimated by the number of volume intersections in a random network of interpenetrating ones [110].

A more sophisticated and precise general formula was derived to estimate the number of fiber contacts in general fiber masses with arbitrary distribution of orientation and fiber length, based on the previous geometrical considerations [52]. An imaginary fiber with arbitrary orientation (θ, ϕ) is placed in the network control volume, so the probability $p_{_{2\to1}}$ of its interaction with other random fibers of orientation (θ', ϕ') can be evaluated as

$$p_{2\to1} = \frac{2d_f\delta_f^2 \sin\hat{\kappa}_{(\theta,\phi;\theta',\phi')}}{V} \tag{3.3}$$

where δ_f is the length scale on which the fiber can be considered straight and $\sin\hat{\kappa}_{(\theta,\phi;\theta',\phi')} = \left[1-\left(\cos\theta\cos\theta'+\sin\theta\sin\theta'\cos(\phi-\phi')\right)^2\right]^{\frac{1}{2}}$ is a measure of the angle between the axes of interacting fibers. Summing up the probability over the orientation space leads to a formulation for the average number of contacts on an arbitrary fiber, N_{fc}

$$N_{fc} = \frac{2d_f N_f \delta_f^2}{V}\int_0^\pi\int_0^\pi J(\theta,\phi)\Omega(\theta,\phi)\sin\theta\,\mathrm{d}\theta\,\mathrm{d}\phi \tag{3.4}$$

where N_f is the number of fibers in V, the total volume of the assembly, and

$$J(\theta,\phi) = \int_0^\pi\int_0^\pi \sin\hat{\kappa}_{(\theta,\phi;\theta',\phi')}\ \Omega(\theta',\phi')\sin\theta'\,\mathrm{d}\theta'\,\mathrm{d}\phi' \tag{3.5}$$

Utilizing this stochastic approach, the number of contacts between all fibers in a general fiber assembly can be obtained as

$$N_v = d_f l_v^2\int_0^\pi\int_0^\pi J(\theta,\phi)\Omega(\theta,\phi)\sin\theta\,\mathrm{d}\theta\,\mathrm{d}\phi \tag{3.6}$$

N_v is the number of fiber-fiber contacts per unit volume of the assembly and l_v is the total fiber length per unit volume. It should be noted that *steric hindrance* between fibers has been ignored in the models. It has two effects on the probability of fiber interaction in a more realistic fashion (taken almost verbatim from the pioneering work introduced by Komori et al. [50]):

- The chance of contact is diminished by restricting the free fiber length on which a new contact may be formed.
- The chance of contact increases by narrowing the free volume in the mass where a fiber can be located without touching the contact parts formed earlier.

Pan [76] proposed a modification to the probability of fiber contacts by introducing the constraints of mutual obstruction on the chance of interaction between fibers with respect

to fibers that are already in contact with a test fiber. Accordingly, the probability of interaction for the $(i+1)$th fiber is

$$p_{i+1\to 1} = \frac{2d_f\delta_f^2 \sin\hat{\kappa}_{(\theta,\phi;\theta',\phi')}}{V} \times \left(1 - \frac{\frac{d_f}{\sin\hat{\kappa}_1} + \frac{d_f}{\sin\hat{\kappa}_2} + \cdots + \frac{d_f}{\sin\hat{\kappa}_i}}{\delta_f}\right) \tag{3.7}$$

which excludes the proportion of fiber length that has been already occupied by the i interacting fibers. In statistically-simplified form, it can be expressed as

$$p_{i+1\to 1} = \frac{2d_f\delta_f^2 \sin\hat{\kappa}_{(\theta,\phi;\theta',\phi')}}{V} \times \left(1 - \frac{id_f\Theta(\theta,\phi)}{\delta_f}\right) \tag{3.8}$$

in which

$$\Theta(\theta,\phi) = \int_0^\pi \int_0^\pi \frac{1}{\sin\hat{\kappa}_{(\theta,\phi;\theta',\phi')}} \Omega(\theta',\phi') \sin\theta' \,\mathrm{d}\theta' \,\mathrm{d}\phi' \tag{3.9}$$

The mean distance between neighboring contact points, in case of 3D random fiber assemblies, can be acquired as

$$\overline{\lambda} = \frac{(2+\pi v_f)d_f}{4v_f} \tag{3.10}$$

The mentioned approaches in number of fiber contacts have been validated mostly in fiber assemblies with low volume fraction. Making these models applicable in highly-compressed fiber masses with higher volume fraction requires more precise considerations in estimating the number of fiber contacts. Particularly, felt has not shown any acceptable accordance with any of the above approaches [100].

Binomial distribution of the number of contact points on a particular fiber is a promising idea that leads to a complicated, but more accurate model [74]. In general, due to the random distribution of contacts, the distribution of the number of contacts on any arbitrary fiber with direction (θ,ϕ) can be expressed according to the Poisson distribution:

$$P(k;\vartheta) = e^{-\vartheta}\frac{\vartheta^k}{k!}, \quad \vartheta = \frac{8v_f\delta_f J(\theta,\phi)}{\pi d_f} \tag{3.11}$$

with the mean value of ϑ and number of exact occurrences k, the probability of which is given by the function. In this statistical approach, there are no constraints imposed by the fibers that are already in contact with the arbitrary fiber. So, the following modification is introduced to achieve a more realistic model [74]:

1. The probability defined in equation 3.11 is now the probability of being very near to the test fiber, i.e. being in interaction with the fiber.

2. If υ_m is the maximum number of contact points that could be created on a fiber length δ_f, the probability that the ith fiber interacts with the test fiber will be

$$p_{i\to 1} = 1 - \frac{(i-1)}{\upsilon_m}, i = 1, 2, \ldots, m \leq \upsilon_m + 1 \tag{3.12}$$

Accordingly, the distribution of the number of contact points on the fiber can be estimated by the binomial distribution [74]

$$B(k; \upsilon_m, S(\vartheta)) = \binom{\upsilon_m}{k} S(\vartheta)^k (1 - S(\vartheta))^{\upsilon_m - k}, \quad S(\vartheta) = 1 - e^{-\frac{\vartheta}{\upsilon_m}} \tag{3.13}$$

with the mean value of $\bar{m} = S(\vartheta)\upsilon_m = \upsilon_m(1 - e^{-\frac{\vartheta}{\upsilon_m}})$. Integrating over the orientation space results in the probability of number of contact points on the random fiber. For the spatial isotropic orientation in which $J(\theta, \phi) = \frac{\pi}{4}$, it will be

$$B_s(k; \upsilon_m, S(\vartheta)) = \binom{\upsilon_m}{k} (1 - e^{-2v_f\gamma})^k (e^{-2v_f\gamma})^{\upsilon_m - k} \tag{3.14}$$

in which $\hat{m} = (1 - e^{-2v_f\gamma})\upsilon_m$ is the mean value of contact points and $\gamma = \frac{\delta_f}{\upsilon_m d_f}$. Consequently, the number of contacts per unit volume, N_v, and mean free fiber length, $\overline{\lambda}$, can be acquired as [74]

$$N_v = \frac{2v_f(1 - e^{-2v_f\gamma})}{\pi d_f^3 \gamma}, \qquad \overline{\lambda} = \frac{\gamma d_f}{(1 - e^{-2v_f\gamma})} \tag{3.15}$$

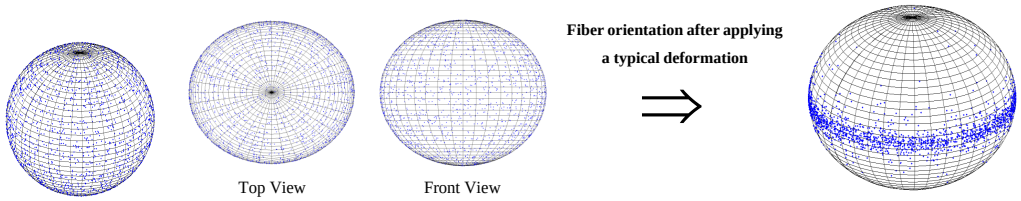

Figure 3.2: Random points on a unit sphere, applying Monte-Carlo algorithm.

Statistical modeling of the fiber network

Structural parameters, which are defined according to the assumptions and criteria considered in constructing a micromechanical model, strictly depend on the architecture and topography of the network. In this research, the general focus is on statistically homogenous networks in which the fibers disperse in the sense that there is no correlation between the spatial and orientation distributions. There is as well a length scale on which the fibers can be considered straight. Moreover, the fiber diameters are constant and their mechanical properties do not change during the compression.

The key point in constructing such a random network is to distribute fibers with an orientation pattern such that the structure behaves like an initially isotropic fiber mass. To this end, the orientation space can be discretized by introducing numerous orientation vectors placed in random fashion over the orientation space, i.e. a set of randomly oriented unit vectors, directed from the center of a unit sphere to a random point on its surface.

The Monte-Carlo approach is one of the most promising algorithms to generate such uniformly distributed random points on a unit sphere. In this method, which is also referred to as rejection method, a large number of points should be picked randomly inside a cube space, i.e. $(x, y, z) \in \mathbb{R} \,|\, x, y, z \in [-1, +1]$, then all points that are at a distance greater than one from the center of the cube are discarded; this gives random points inside a unit sphere. Afterward, the random points are projected onto the surface of the unit sphere by normalizing all the obtained vectors. However, this requires a fairly large number of directions to get a truly isotropic distribution. To improve the random distribution with a limited number of unit vectors, a simple diffusion algorithm has been developed to spread the points more evenly on the unit sphere [20].

A simulated result of this process is shown in Figure 3.2, which visually confirms the acceptable performance of the algorithm. Moreover, it demonstrates the change in the orientation of the random vectors due to a typical uniaxial compression load in the third

direction, as will be discussed in the following sections.

3.2 Continuum mechanics of random fiber networks

Introducing structural parameters can be considered as the key point in developing a continuum model of fiberwebs. It is based on the type of the model, simplification assumptions, and the degree of complexity. In this research, we do not regard microstructural complex models based on the Finite Element Method, Molecular Dynamics Criteria, or Discrete Element Procedures, since application of such approaches in multibody simulation, which is the main goal of the research, is not computationally justifiable. To construct a micromechanical prototype in studying mechanical behavior of three dimensional fiber assemblies, statistical approaches are the most reliable tools to reduce the degree of complexity in the models. Averaging the number of fiber-to-fiber contacts, distribution of free fiber length and fiber diameter, location of contact points, and critical angle for sliding contacts have been utilized by many researches in mechanistic model of nonwovens. Moreover, some simplifying assumptions are required to make the development of the model feasible at a microscopic scale.

In Section 3.2, three continuum models for the compression behavior of fiber assemblies, applicable to networks with relatively high volume fraction, are examined. The first model is based on the elongation of constituent fibers at the micro level, introduced by Narter et al. [72], for small deformation ranges. Incorporating a binomial distribution of fiber contacts along with the structural evolution, we extended the model to a micromechanical approach for larger deformation ranges. The second model, presented by Alkhagen et al. [1], uses a rate theory for granular solids to develop a micromechanical model, based on bending and torsion of the fibers, for predicting compression behavior of felt. The last model, derived by Neckář et al [74], uses a mechanistic approach based on fiber bending at the microscale, along with a binomial distribution of fiber contacts, to determine the mechanical behavior of felt in compression. Parameter identification for the models helped us in estimating the predominant deformation schemes in uniaxial compression of felt, as well as the model performance and accuracy.

3.2.1 Micromechanics of bonded nonwoven structures - Axial microstructural deformation

Nonwoven fabrics are defined as a web of randomly oriented fibers, bonded by friction, mechanical, or chemical treatments. According to Rawal et al. [94], nonwoven fabrics

are formed by putting the fibers with desired orientation characteristics together (web formation), and then binding them by several means, depending on the type of the fabric, e.g. carded, air laid, spunbonded, meltblown, needlepunched, hydroentangled, adhesive bonded, thermal bonded, stitch bonded fiberwebs.

To develop a constitutive model for such fiberwebs, for the case that axial deformation of fibers is the only deformation scheme in response to macroscopic loads, the following assumptions, taken almost verbatim from Narter's paper [72], need to be considered:

1. There are a large number of fibers bonded at every crossover point by mechanical and chemical action as well as heat and moisture. The bonds are assumed to be non-deformable within the range of loadings characterized by the small-strain theory.

2. The average bond-to-bond distance along a fiber in the assembly is small enough to approximate the fiber path between successive bonds by a straight line.

3. In the stress-strain and bond-to-bond distance range considered, the compressive loads developed in the fibers do not exceed their critical buckling loads. As such, during small-strain range deformation of the structure, no additional contacts between the fibers are expected to occur.

4. The fiber elastic modulus under compression is the same as the fiber elastic modulus under extension. The fibers have circular cross section with the same diameter.

5. In the context of fiber-reinforced composite theories, the matrix is considered to be void, and hence, in the range of static or quasi-static loadings, no fibermatrix interactions are considered.

6. The fiberweb is assumed to be homogeneous in structure. In this case, the orientation distribution function defines the structure completely. Alternatively, at some small enough scale, somewhat larger than the bond-to-bond distance, all cubic elements of the fiberweb exhibit statistically, more or less, the same properties. That is, at this scale level and above, the web behaves as a homogeneous continuum.

This model is a generalized framework of the pioneering work done by Cox [17] which was confined to spatial isotropic network in the small-strain range.

Constitutive equations are achieved considering a representative volume in which the orientation distribution function defines a statistically equivalent homogeneous structure. Consequently, a continuum mechanics approach can be utilized in a unit cell, relying on the

above assumptions. In the small-strain range, it is reasonable to consider the fiber element elongation as the predominant structural deformation; its application for micromechanical modeling of felt is going to be studied in this section. Figure 2.1 shows such a representative volume, on a scale somewhat larger than the fiber segment length between contact points, and a random fiber with arbitrary directions θ and ϕ. θ is the azimuthal angle between the third axis, X_3, and the axis of the fiber and ϕ is the polar angle between the first axis, X_1, and the normal projection of the fiber axis on the horizontal plane.

Referring to Figure 2.1, the fiber segment deforms exactly in the same way as a line element of the same orientation in the representative volume. This affine deformation of the fiber may be regarded as a strong simplification. Accordingly, strain ε_f on a random fiber element can be expressed in terms of strains imposed on the volume according to second-order strain transformations [72]:

$$\begin{aligned}\varepsilon_f = \varepsilon_{33}\cos^2\theta + \varepsilon_{11}\sin^2\theta\cos^2\phi + \varepsilon_{22}\sin^2\theta\sin^2\phi + \gamma_{23}\cos\theta\sin\theta\sin\phi + \\ \gamma_{12}\sin^2\theta\cos\phi\sin\phi + \gamma_{13}\cos\theta\sin\theta\cos\phi\end{aligned} \tag{3.16}$$

in which $\varepsilon_{ij,\ i=j}$ are normal strains and $\gamma_{ij,\ i\neq j}$ are shear strains. Utilizing Hooke's law of elasticity, the axial force imposed on the fiber will be:

$$P_f(\theta,\phi) = A_f\sigma_f(\theta,\phi) = A_f E\varepsilon_f(\theta,\phi) \tag{3.17}$$

where σ_f and E are the stress and Young's modulus of elasticity of the fiber element, and A_f is the cross section area of the fiber. To find the components of stress on the representative volume, the total contribution of all fibers of orientation (θ,ϕ) should be calculated and then summed up over the orientation space $\theta \in [0,\pi]$ and $\phi \in [0,\pi]$. If $\Omega(\theta,\phi)$ is the density function of orientation of fibers and N_{fv} is the number of straight fiber segments per unit volume, $N_{fv}\times\Omega(\theta,\phi)$ will be the total number of fibers with orientation (θ,ϕ) per unit volume. $\Omega(\theta,\phi)$, also called Orientation Distribution Function, is subjected to the normalization condition:

$$\int_0^\pi\int_0^\pi \Omega(\theta,\phi)\sin\theta\,\mathrm{d}\theta\,\mathrm{d}\phi = 1 \tag{3.18}$$

Accordingly, the number of fibers of orientation (θ,ϕ) crossing the unit areas perpendicular to the coordinate axes is given by

$$N_{fv}\Omega(\theta,\phi)\Upsilon_{x_i} \tag{3.19}$$

in which $\Upsilon_{x_1} = \sin\theta\cos\phi$, $\Upsilon_{x_2} = \sin\theta\sin\phi$, and $\Upsilon_{x_3} = \cos\theta$

The corresponding normal and shear forces on each plane per unit area, associated with all fibers with the same orientation, can be obtained by multiplying equations 3.19 and 3.17 in each specific direction, then summed up over the orientation space. So, the resulting stresses will be in the form

$$\sigma_i = A_f E N_{fv} \int_0^{\pi}\int_0^{\pi} \varepsilon_f f_i(\theta,\phi)\Omega(\theta,\phi)\sin\theta\,\mathrm{d}\theta\,\mathrm{d}\phi \tag{3.20}$$

where $\{\sigma_1,\sigma_2,\sigma_3,\sigma_4,\sigma_5,\sigma_6\}^T = \{\sigma_{11},\sigma_{22},\sigma_{33},\tau_{12},\tau_{13},\tau_{23}\}^T$ and $f_i(\theta,\phi)$ are functions of trigonometric coefficients obtained based on multiplication of equations 3.19 and 3.17 in developing the stress tensor. Considering the generalized Hooke's law for linear elastic materials, the stress and strain tensors, $\boldsymbol{\sigma}$ and $\boldsymbol{\epsilon}$, are related as

$$\boldsymbol{\sigma} = [S]\boldsymbol{\epsilon} \Rightarrow \boldsymbol{\epsilon} = [C]\boldsymbol{\sigma} \tag{3.21}$$

where the stiffness tensor, $[S]$, can be obtained by substituting ε_f from equation 3.16 into equation 3.20:

$$S_{ij} = A_f E N_{fv} \int_0^{\pi}\int_0^{\pi} f_{ij}(\theta,\phi)\Omega(\theta,\phi)\sin\theta\,\mathrm{d}\theta\,\mathrm{d}\phi, \quad i,j = 1,2,...,6 \tag{3.22}$$

in which $f_{ij}(\theta,\phi) = \cos^m\theta\sin^n\theta\cos^k\phi\cos^l\phi$ where m, n, k, and l are constant exponents for each i,j combination. It is worthwhile to note that the compliance tensor $[C] = [S]^{-1}$, holds on the space of symmetric 4th-order tensors.

Referring to the SEM images captured from felt, it is obvious that the fibers have been dispersed through the network with no specific orientation, so it can be considered as a random fiberweb at the initial state. If the network deforms at small-strain ranges so that all contact points can be categorized as non-sliding bonds, then the mentioned model can be applied to felt as a bonded nonwoven fiber mass excluding compression hysteresis. In this case, the orientation distribution function is independent of θ and ϕ, so utilizing the normalization condition described by equation 3.18 gives:

$$\Omega(\theta,\phi)\int_0^{\pi}\int_0^{\pi}\sin\theta\,\mathrm{d}\theta\,\mathrm{d}\phi = 1 \Rightarrow \Omega(\theta,\phi) = \frac{1}{2\pi} \tag{3.23}$$

The corresponding compliance tensor, obtained using equation 3.22, is given by:

$$(C_{ij}) = \begin{pmatrix} \frac{6}{K} & -\frac{3}{2K} & -\frac{3}{2K} & 0 & 0 & 0 \\ -\frac{3}{2K} & \frac{6}{K} & -\frac{3}{2K} & 0 & 0 & 0 \\ -\frac{3}{2K} & -\frac{3}{2K} & \frac{6}{K} & 0 & 0 & 0 \\ 0 & 0 & 0 & \frac{15}{K} & 0 & 0 \\ 0 & 0 & 0 & 0 & \frac{15}{K} & 0 \\ 0 & 0 & 0 & 0 & 0 & \frac{15}{K} \end{pmatrix} \tag{3.24}$$

where $K = A_f E N_{fv}$. Macroscopic modulus of elasticity in the principal directions is acquired based on the procedure presented by Love [63]:

$$E_1 = \frac{\det[S]}{S_m[1,1]} \quad \rightarrow \quad E_1 = \frac{1}{6K} = E_2 = E_3 \tag{3.25}$$

in which $S_m[1,1]$ is the minor determinant corresponding to $S[1,1]$.

For larger deformations in the case of uniaxial compression, we extended the model presuming the following simplifications:

1. Each step of deformation is assumed to be in the small-strain range, so the number of fiber-to-fiber contacts is constant in every deformation step, but changes during transition from one step to the next one.

2. Macroscopic modulus of elasticity can be considered constant in each deformation step, but it changes based on variance in the number of contacts through transition stages, which in turn depends on bulk strain or volume fraction.

3. Distribution of fiber orientation starts from a random spatial state, but evolves according to affine transformation of the network.

4. We introduce an uncertainty parameter, K_E, accounting for all modeling errors due to ignoring fiber buckling and sliding in the considered deformation range, so that $K = K_E A_f E N_{fv}$

Considering the specific case of uniaxial deformation in the third direction,

$$\varepsilon_f = \varepsilon_{33}\cos^2\theta \quad \text{and} \quad f_3(\theta,\phi) = \cos^2\theta \tag{3.26}$$

consequently,

$$\sigma_3 = K_E A_f E N_{fv} \Phi, \quad \Phi = \int_0^{\pi}\int_0^{\pi} \varepsilon_{33}\cos^2\theta\cos^2\theta\ \Omega(\theta,\phi)\sin\theta\,\mathrm{d}\theta\,\mathrm{d}\phi \tag{3.27}$$

For the number of straight fibers per unit volume N_{fv}, which is directly related to the number of fiber to fiber contacts N_v, the binomial distribution of number of fiber contacts presented in equation 3.15 is utilized. It is more precise than the other methods and as we will see in the following sections, it is more promising in micromechanical modeling of wool felt.

In each deformation step during the compression, the orientation evolution is modeled using an affine rotation of the individual fibre segments imposed by equation 3.57. By applying the equation to each unit vector in the initially-random fiber assembly, an orientation distribution function can be estimated to be used in calculating the structural tensors. Hence, Φ, which is the structural parameter for the model, can be evaluated according to the mentioned procedure. N_v is a function of volume fraction and contains the parameter γ; this parameter is identified by minimizing (numerically) the difference between simulated and experimental results. Simulation results for a typical felt used in piano mechanisms is shown in Figure 3.3

Although the resultant curve obtained in the process of parameter identification seems acceptable, the optimized parameter γ is physically unrealistic and cannot be negative. It signifies that axial deformation of fibers cannot be a predominant structural deformation scheme for micromechanical modeling of felt in large deformation schemes. However, it may work for other fiber assemblies.

3.2.2 Micromechanics of bonded nonwoven structures - Granular media approach

A rate theory for granular solids

A granular solid, as defined by Alkhagen and Toll [1], "consists of solid particles which interact by mechanical contact; all stress being transmitted across contact surfaces from

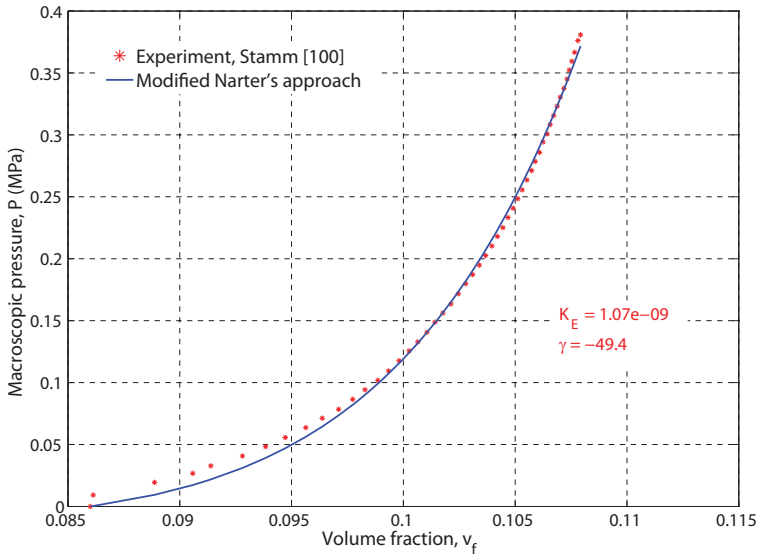

Figure 3.3: Modified Narter's equation 3.27 and the experimental data for moderate red felt with $v_{f0} = 0.086$.

one particle to another". They developed a formulation for the rate modeling of flexible granular solids based on the affine average motion of the contact points.

To represent a granular continuum model, a Representative Elementary Volume (REV) will be used such that the macroscopic velocity gradient can be considered constant on the scale of the volume. In quasi static conditions, Love [63] developed the average macroscopic stress $\boldsymbol{\sigma}$, based on Cauchy's theory as:

$$\boldsymbol{\sigma} = \frac{1}{V} \sum \boldsymbol{P}\boldsymbol{r} \tag{3.28}$$

where the symbol $\sum$ indicates summation over all contact points on all particles in the representative volume V, $\boldsymbol{P}$ is the contact force between solid particles, and $\boldsymbol{r}$ is the position of the contact points. It should be noted that $\boldsymbol{r}$ can be defined locally for each particle. Depending on the structure of the assembly, the configuration of contacts can be described by a limited number of contact variables. To find the average stress over the representative volume, a contact between two particles is considered, with one of them called the test particle, and a statistical approach is utilized in the form [1]

$$\boldsymbol{\sigma} = N_v \oint \oint \overline{\boldsymbol{P}\boldsymbol{r}} \zeta(\boldsymbol{r}, \boldsymbol{n}, \dots) \, \mathrm{d}\boldsymbol{r} \, \mathrm{d}\boldsymbol{n} \tag{3.29}$$

in which N_v is the number of contact points per unit volume, the overbar denotes the average over all contact points with configuration $(\boldsymbol{r}, \boldsymbol{n}, \dots)$, and $\zeta(\boldsymbol{r}, \boldsymbol{n}, \dots)$ is the probability density of configuration $(\boldsymbol{r}, \boldsymbol{n}, \dots)$, satisfies the normalized condition

$$\oint \oint \zeta(\boldsymbol{r}, \boldsymbol{n}, \dots) \, \mathrm{d}\boldsymbol{r} \, \mathrm{d}\boldsymbol{n} = 1 \tag{3.30}$$

It is to be noted that the contact variables should at least include $\boldsymbol{r}$ and $\boldsymbol{n}$, in which $\boldsymbol{n}$ is the outward unit normal vector to the test particle surface at the point of contact with the other fibers. Accordingly, the contact force $\boldsymbol{P}$ will be a stochastic function of these variables.

In granular solids, the work done by stresses during the deformation process is path dependent. Constitutive equations for this type of material, which are called hypoelastic materials, depend on the path followed in a deformation process and hence require a rate theory. It is worthwhile to note that this path dependency is not due to frictional dissipations. In developing the rate equation, two main assumptions have been considered as follows [1]:

1. The contact force between interacting grains is generated by the normal force, without which the contact force approaches zero.

2. The contact displacement rate is affine for a given set of values of the contact variables:

$$\overline{\dot{\boldsymbol{r}}} = \overline{\dot{\boldsymbol{r}}}(\boldsymbol{r}, \boldsymbol{L}) = \boldsymbol{L} \cdot \boldsymbol{r} \tag{3.31}$$

   in which $\boldsymbol{L} = (\nabla \boldsymbol{V})^T$ is the spatial velocity gradient.

The first one assumes that there is no adhesion at the smooth contact surfaces, i.e. ideal friction. In other words, contacts in the process of being formed or broken must be force free. The second assumption implies that the average displacement of contacts with a certain configuration only depends on the macroscopic velocity gradient.

The time differentiation of equation 3.28 will be

$$\frac{\mathrm{d}\boldsymbol{\sigma}}{\mathrm{d}t} = -\frac{1}{V^2}\frac{\mathrm{d}V}{\mathrm{d}t}\sum \boldsymbol{P}\boldsymbol{r} + \frac{1}{V}\frac{\mathrm{d}}{\mathrm{d}t}(\sum \boldsymbol{P}\boldsymbol{r}) \tag{3.32}$$

Considering the above-mentioned assumptions along with the statistical stress tensor represented in equation 3.29, the stress rate tensor will be

$$\dot{\boldsymbol{\sigma}} + (\boldsymbol{\delta} : \boldsymbol{L})\boldsymbol{\sigma} = N_v \left(\langle \overline{\boldsymbol{P}}\boldsymbol{r} \rangle_c \cdot \boldsymbol{L}^T + \langle \overline{\dot{\boldsymbol{P}}}\boldsymbol{r} \rangle_c \right) \tag{3.33}$$

where $\langle \cdot \rangle_c = \oint \oint (\cdot)\zeta(\boldsymbol{r}, \boldsymbol{n}, \dots)\, \mathrm{d}\boldsymbol{r}\, \mathrm{d}\boldsymbol{n}$ denotes an average over all possible values of contact variables. The second term represents a double-dot product in which $\boldsymbol{\delta}$ is the Kronecker delta. Since $\boldsymbol{r}$ is a contact variable, it does not need an overbar in the averaging integral. $\overline{\dot{\boldsymbol{P}}}$, which is the time derivative of the average contact force vector over all contact points with the configuration $(\boldsymbol{r}, \boldsymbol{n}, \dots)$, can be considered as a function of the contact variables and also macroscopic field variables such as $\boldsymbol{L}$:

$$\overline{\dot{\boldsymbol{P}}} = \boldsymbol{\phi}(\boldsymbol{r}, \boldsymbol{n}, \dots, \boldsymbol{L}, \dots) \tag{3.34}$$

In constitutive modeling of the continuum, the invariant property of the stress tensor with respect to frame of reference should be satisfied. Accordingly, to verify that equation 3.33 is material frame indifferent (objective), the necessary and sufficient conditions on $\overline{\dot{\boldsymbol{P}}}$ can be obtained as [1]

$$\overline{\dot{\boldsymbol{P}}}(\hat{\boldsymbol{Q}} \cdot \boldsymbol{r}, \hat{\boldsymbol{Q}} \cdot \boldsymbol{n}, \dots, \dot{\hat{\boldsymbol{Q}}} \cdot \hat{\boldsymbol{Q}}^T + \hat{\boldsymbol{Q}} \cdot \boldsymbol{L} \cdot \hat{\boldsymbol{Q}}^T, \dots) - \hat{\boldsymbol{Q}} \cdot \overline{\dot{\boldsymbol{P}}}(\boldsymbol{r}, \boldsymbol{n}, \dots, \boldsymbol{L}, \dots) - \dot{\hat{\boldsymbol{Q}}} \cdot \overline{\boldsymbol{P}} = \boldsymbol{0} \tag{3.35}$$

$\hat{\boldsymbol{Q}}$ is the orthogonal time-dependent second-order tensor of rigid body motion of the type $\boldsymbol{x}^* = \hat{\boldsymbol{Q}}(t)\boldsymbol{x} + \hat{\boldsymbol{C}}(t)$, which is referred to as a Euclidean transformation. $\boldsymbol{x}$ is the position vector relative to a coordinate system, $\boldsymbol{x}^*$ is the mapped position vector relative to another frame of reference, and $\hat{\boldsymbol{C}}(t)$ is the rigid body translation between two frames.

Granular media - Fiber network

To employ the rate theory of granular solids in mechanistic modeling of a fiber assembly, each fiber segment can be regarded as a particle. As before, we assumed that each fiber

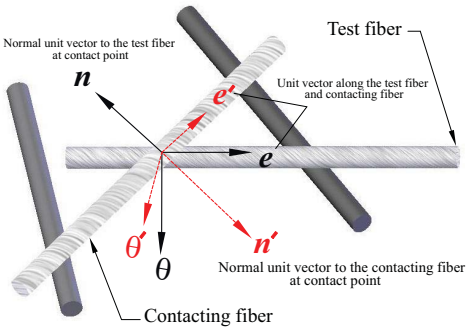

Figure 3.4: A typical contact point between interacting fibers, along with axes definition in a Cartesian coordinate system.

segment, which is located between two adjacent contact points, is approximately straight and also slippage between fibers can be ignored. The validity of such description also requires that the mean free fiber length, which is defined as the distance between two adjacent contact points, should be smaller than the crimp spacing of the fiber, which is defined as the length scale on which the fibers can be considered straight. This is a reasonable assumption according to image analysis obtained by SEM. Under these conditions, the contact stress on the segment will be much larger than the stress due to the internal load from the rest of the fiber.

As demonstrated in Figure 3.4, a set of orthonormal basis vectors $\boldsymbol{n}$, $\boldsymbol{e}$, and $\boldsymbol{\theta}$ will be attached to each contact point between interacting fibers so that $\boldsymbol{e}$ is aligned in the direction of fiber axis and $\boldsymbol{n}$ is the normal vector at the contact. Therefore,

$$\boldsymbol{r} = r_n\boldsymbol{n} + r_e\boldsymbol{e} + r_\theta\boldsymbol{\theta} \quad \text{and} \quad \boldsymbol{P} = p_n\boldsymbol{n} + p_e\boldsymbol{e} + p_\theta\boldsymbol{\theta} \tag{3.36}$$

The contact variables space is expanded by $(\boldsymbol{e}, \boldsymbol{e}', \boldsymbol{r}, \boldsymbol{r}')$, which are the axis orientations and position vectors of the two contacting fibers. In addition, a convected force rate, which satisfies the frame indifference condition obtained in equation 3.35, has been selected as [1]

$$\overline{\dot{\boldsymbol{P}}} = (\overline{\dot{p_n}}\boldsymbol{n} + \overline{\dot{p}_e}\boldsymbol{e} + \overline{\dot{p}_\theta}\boldsymbol{\theta}) + \boldsymbol{L}\cdot\overline{\boldsymbol{P}} \tag{3.37}$$

Although it is inconsistent with maintaining orthonormality of the basis vectors, this force rate should work for the case that compressive deformation is of primary interest. By

substituting equation 3.36 and equation 3.37 into equation 3.33, the constitutive relation will be [1]:

$$\overset{\triangle}{\boldsymbol{\sigma}} = N_v \langle \overline{\dot{p_n}} r_n \boldsymbol{nn} + \overline{\dot{p_e}} r_e \boldsymbol{ee} + \overline{\dot{p_\theta}} r_\theta \boldsymbol{\theta\theta} \rangle_c : \boldsymbol{L} \tag{3.38}$$

in which

$$\overset{\triangle}{\boldsymbol{\sigma}} = \dot{\boldsymbol{\sigma}} + (\boldsymbol{\delta} : \boldsymbol{L})\boldsymbol{\sigma} - \boldsymbol{\sigma} \cdot \boldsymbol{L}^T - \boldsymbol{L} \cdot \boldsymbol{\sigma} \tag{3.39}$$

$\overset{\triangle}{\boldsymbol{\sigma}}$ is an objective stress rate tensor called the Truesdell stress rate [113]. Neglecting the slip between fibers, the force rates can be related to the principal displacement rates through the average compliances of all contacts as [1]

$$\overline{\dot{p_n}} = \frac{\overline{\dot{r_n}}}{\overline{\langle s_n \rangle_c}}, \ \overline{\dot{p_e}} = \frac{\overline{\dot{r_e}}}{\overline{\langle s_e \rangle_c}}, \ \text{ and } \ \overline{\dot{p_\theta}} = \frac{\overline{\dot{r_\theta}}}{\overline{\langle s_\theta \rangle_c}} \tag{3.40}$$

where s_n, s_e, and s_θ are the local compliance of a particular contact defined as

$$s_n = \frac{\partial r_n}{\partial p_n}, \ s_e = \frac{\partial r_e}{\partial p_e}, \ \text{ and } \ s_\theta = \frac{\partial r_\theta}{\partial p_\theta} \tag{3.41}$$

Particularly, it should be noticed that $\overline{\langle s_i \rangle_c} \approx \frac{dr_i}{dp_i} \neq \frac{\partial r_i}{\partial p_i}$. Substituting force rate equations 3.40 into equation 3.38 results in:

$$\overset{\triangle}{\boldsymbol{\sigma}} = N_v \left(\frac{\langle r_n \overline{\dot{r_n}} \boldsymbol{nn} \rangle_c}{\overline{\langle s_n \rangle_c}} + \frac{\langle r_e \overline{\dot{r_e}} \boldsymbol{ee} \rangle_c}{\overline{\langle s_e \rangle_c}} + \frac{\langle r_\theta \overline{\dot{r_\theta}} \boldsymbol{\theta\theta} \rangle_c}{\overline{\langle s_\theta \rangle_c}} \right) : \boldsymbol{L} \tag{3.42}$$

Assuming that the principal displacement rates are equal to the stretch rates in the $\boldsymbol{n}$, $\boldsymbol{e}$, and $\boldsymbol{\theta}$ directions, results

$$\overline{\dot{r_n}} = r_n \boldsymbol{nn} : \boldsymbol{L}, \ \overline{\dot{r_e}} = r_e \boldsymbol{ee} : \boldsymbol{L}, \ \text{ and } \ \overline{\dot{r_\theta}} = r_\theta \boldsymbol{\theta\theta} : \boldsymbol{L} \tag{3.43}$$

In case of random orientations, r_n, r_e, and r_θ are independent of $\boldsymbol{n}$, $\boldsymbol{e}$, and $\boldsymbol{\theta}$, so

$$\overset{\triangle}{\boldsymbol{\sigma}} = N_v \left(\frac{\langle r_n^2 \rangle_c}{\overline{\langle s_n \rangle_c}} \langle \boldsymbol{nnnn} \rangle_c + \frac{\langle r_e^2 \rangle_c}{\overline{\langle s_e \rangle_c}} \langle \boldsymbol{eeee} \rangle_c + \frac{\langle r_\theta^2 \rangle_c}{\overline{\langle s_\theta \rangle_c}} \langle \boldsymbol{\theta\theta\theta\theta} \rangle_c \right) : \boldsymbol{L} \tag{3.44}$$

in which $\langle \boldsymbol{nnnn} \rangle_c$, $\langle \boldsymbol{eeee} \rangle_c$, and $\langle \boldsymbol{\theta\theta\theta\theta} \rangle_c$ are fourth-order structure tensors.

Assuming that the structure is statically homogeneous and the contacts are dispersed uniformly over the network, there will be no correlation between spatial and orientation distributions. Let the overall probability density of finding a fiber with configuration $\boldsymbol{e}$ be $\boldsymbol{\psi}(\boldsymbol{e})$. Also, the probability density of intersection of two fibers of orientation $\boldsymbol{e}$ and $\boldsymbol{e}'$ is proportioned to the sine of the spatial angle between the two fibers or $|\boldsymbol{e} \times \boldsymbol{e}'|$, independent of $\boldsymbol{r}$. So, it is fairly straightforward to show that a quantity $q(\boldsymbol{e}, \boldsymbol{e}')$, which is independent of position variables, can be averaged over all contact configurations as [1]:

$$\oint\oint\oint\oint q(\boldsymbol{e}, \boldsymbol{e}') \zeta(\boldsymbol{r}, \boldsymbol{r}', \boldsymbol{e}, \boldsymbol{e}') \, \mathrm{d}\boldsymbol{e} \, \mathrm{d}\boldsymbol{e}' \, \mathrm{d}\boldsymbol{r} \, \mathrm{d}\boldsymbol{r}' = \frac{1}{f} \oint\oint q(\boldsymbol{e}, \boldsymbol{e}') |\boldsymbol{e} \times \boldsymbol{e}'| \boldsymbol{\psi}(\boldsymbol{e}) \boldsymbol{\psi}(\boldsymbol{e}') \mathrm{d}\boldsymbol{e} \, \mathrm{d}\boldsymbol{e}' \tag{3.45}$$

in which $f = \oint\oint |\boldsymbol{e} \times \boldsymbol{e}'| \boldsymbol{\psi}(\boldsymbol{e}) \boldsymbol{\psi}(\boldsymbol{e}') \mathrm{d}\boldsymbol{e} \, \mathrm{d}\boldsymbol{e}'$. Structure tensors, which are functions of $\boldsymbol{e}$ and $\boldsymbol{e}'$, can be evaluated using the general equation 3.45.

Orientation evolution of the fibers will be modeled by affine rotation of the fiber axes. It is expressed as a function of deformation gradient [1]:

$$\boldsymbol{e} = \frac{\boldsymbol{F} \cdot \boldsymbol{e}_r}{\sqrt{\boldsymbol{e}_r \cdot \boldsymbol{F}^T \cdot \boldsymbol{F} \cdot \boldsymbol{e}_r}} \tag{3.46}$$

where $\boldsymbol{F} = \dfrac{\partial \boldsymbol{x}}{\partial \boldsymbol{X}_r}$ is the deformation gradient with respect to a given reference configuration denoted by index r, in which $\boldsymbol{x}$ and $\boldsymbol{X}_r$ are position vectors in current and reference configuration, respectively.

To evaluate the compliances defined in equation 3.41, two sources of contact force have been considered: fiber bending and fiber torsion. The normal compliance s_n is governed by bending of the test fiber (unprimed fiber), based on Euler-Bernoulli beam theory [1]

$$\overline{s_n} = \frac{\overline{\partial r_n}}{\partial p_n} = \frac{\overline{\lambda^3}}{6\pi k_b E {r_f}^4} \tag{3.47}$$

where E is the Young's modulus of elasticity, r_f is the fiber radius, $\overline{\lambda}$ is the mean free

fiber length, and k_b is the geometric constant that will be 1 if the beam is loaded at its midsection and fixed at its end sections. The transverse compliance is governed by torsion and bending of the test fiber

$$\overline{s_\theta} = \overline{\frac{\partial r_\theta}{\partial p_\theta}} = \frac{\overline{16\lambda}}{3\pi k_t E {r_f}^2} + \frac{\overline{\lambda^3}}{6\pi k_b E {r_f}^4} \tag{3.48}$$

in which k_t is unity for a simple torsion bar loaded by a moment $r_f p_\theta$ at its midsection and fixed at its end sections. The axial compliance is governed by torsion and bending of the contacting fiber

$$\overline{s_e} = \overline{\frac{\partial r_e}{\partial p_e}} = \frac{\overline{16\lambda'}}{3\pi k_t E' {r'_f}^2} + \frac{\overline{\lambda'^3}}{6\pi k_b E' {r'_f}^4} \tag{3.49}$$

By fixing a local coordinate system on the fiber, the position vector of the contacts will have the components $r_n \sim r_\theta \sim r_f$ and a random distribution of contacts along the fiber $r_e \sim \hat{x}\ell_c$, where ℓ_c is half the crimp spacing and $\hat{x}$ is a stochastic variable randomly distributed in the interval $0 \leq \hat{x} \leq 1$. The crimp spacing can also be related to the fiber size as $\ell_c = \beta r_f$ which β is called the crimp ratio. Assuming that the distribution of contact spacing is exponential, representing a Poisson distribution, it can be proved that $\overline{\lambda^3} = 6\overline{\lambda}^3$.

The average contact spacing, $\overline{\lambda}$, can be obtained as [110]

$$\overline{\lambda}(\boldsymbol{e}) = \frac{\pi r_f}{4\hbar(\boldsymbol{e}) v_f} \quad \text{where} \quad \hbar(\boldsymbol{e}) = \oint |\boldsymbol{e} \times \boldsymbol{e}'| \boldsymbol{\psi}(\boldsymbol{e}') \mathrm{d}\boldsymbol{e}' \tag{3.50}$$

where v_f is the fiber volume fraction and $\hbar(\boldsymbol{e})$ signifies the average number of fibers that contact the fiber with direction $\boldsymbol{e}$. The average number of contacts per unit volume, N_v, can be expressed as [110]

$$N_v = \frac{4 f v_f^2}{\pi^2 {r_f}^3} \quad \text{where} \quad f = \oint\oint |\boldsymbol{e} \times \boldsymbol{e}'| \boldsymbol{\psi}(\boldsymbol{e}) \boldsymbol{\psi}(\boldsymbol{e}') \, \mathrm{d}\boldsymbol{e} \, \mathrm{d}\boldsymbol{e}' \tag{3.51}$$

It is identical to the results represented in equation 3.6.

Substituting equations 3.47 - 3.51, the average compliances in equation 3.44 will be obtained as [1]

$$N_v \frac{\langle r_\theta^2 \rangle_c}{\overline{\langle s_\theta \rangle}_c} = \frac{E}{\left(\frac{3}{\pi^2} k_t f^2 v_f^3\right)^{-1} + \left(\frac{256}{\pi^4} k_b f^4 v_f^5\right)^{-1}} \quad \text{and} \quad N_v \frac{\langle r_e^2 \rangle_c}{\overline{\langle s_e \rangle}_c} = \frac{E\beta^2}{\left(\frac{1}{\pi^2} k_t f^2 v_f^3\right)^{-1} + \left(\frac{256}{3\pi^4} k_b f^4 v_f^5\right)^{-1}}$$

$$N_v \frac{\langle r_n^2 \rangle_c}{\overline{\langle s_n \rangle}_c} = \frac{256 k_b E}{\pi^4} f^4 v_f^5 \tag{3.52}$$

Provided that $\beta^2 \gg 1$, the transverse component may be neglected. Finally, the macroscopic Cauchy stress will be [1]

$$\overset{\triangle}{\boldsymbol{\sigma}} = \left[\frac{256 k_b E}{\pi^4} f^4 v_f^5 \langle \boldsymbol{nnnn} \rangle_c + \frac{E\beta^2}{\left(\frac{1}{\pi^2} k_t f^2 v_f^3\right)^{-1} + \left(\frac{256}{3\pi^4} k_b f^4 v_f^5\right)^{-1}} \langle \boldsymbol{eeee} \rangle_c \right] : \boldsymbol{L} \tag{3.53}$$

The Cauchy equations are strictly dependent on the architecture of the fiber network, which is governed by the orientation distribution function, and accompanied by the evolution equations 3.57 for fiber orientation.

Evaluation of the model

To evaluate the simulation model, we followed the same process as Alkhagen et al. [1] introduced in their pioneering paper. In case of uniaxial compression in the third direction, the macroscopic velocity gradient can be expressed as [1]

$$L_{33} = -\frac{\dot{v}_f}{v_f} \tag{3.54}$$

Substituting the velocity gradient into equation 3.53, the average stress (pressure P) in the third direction will be

$$\frac{dP}{dv_f} + \frac{P}{v_f} = E f^4 v_f^4 \left(\frac{256 k_b}{\pi^4} \langle n_3 n_3 n_3 n_3 \rangle_c + \frac{\beta^2}{\left(\frac{1}{\pi^2} k_t f^{-2} v_f^{-2}\right)^{-1} + \left(\frac{256}{3\pi^4} k_b\right)^{-1}} \langle e_3 e_3 e_3 e_3 \rangle_c \right) \tag{3.55}$$

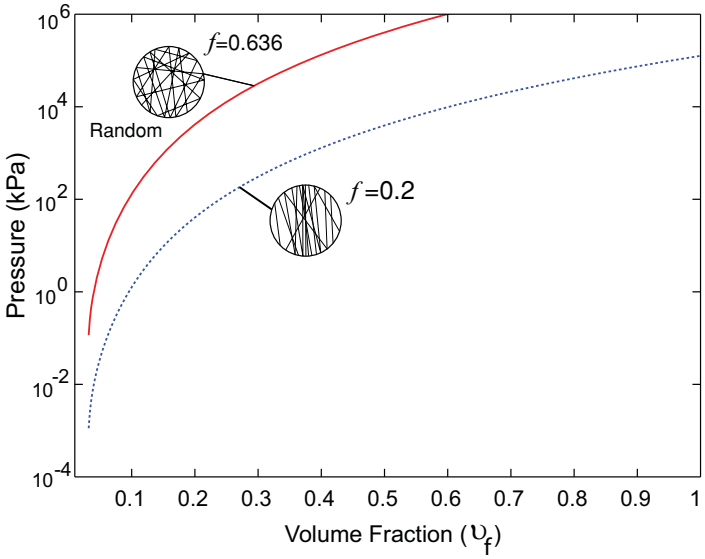

Figure 3.5: Uniaxial compression of planar fiber masses with different fiber orientation distribution.

For a planar fiber mass, in which $\langle n_3 n_3 n_3 n_3 \rangle_c = 1$ and $\langle e_3 e_3 e_3 e_3 \rangle_c = 0$, it yields

$$P = \frac{128}{3\pi^4} k_b E f^4 \upsilon_f^5 \tag{3.56}$$

which coincide with the results obtained by Toll and Mason [111] for a planar fiber network with $k_b = 2.4$. Figure 3.5 shows pressure-volume fraction for a typical glass fiber mass with Young's modulus $E = 75\,\text{Gpa}$ for two different distributions of fiber orientation. As expected, compression load in each level of volume fraction is higher for the network with greater value of f, in which fiber orientations approach to a fiber structure with higher degree of randomness.

To apply the model for a 3D fiber network like felt, a reference configuration, in which the fibers are dispersed randomly over the structure, should be considered. Then, a general case with non-random initial orientation distribution of fibers is modeled by a fictitious initial deformation $\boldsymbol{F}_0$ relative to the reference configuration $\boldsymbol{F}_r = \boldsymbol{I}$, which $\boldsymbol{I}$ is the identity matrix. The deformation gradient tensor for the uniaxial compression of a random fiber network in terms of the current and reference volume fraction is

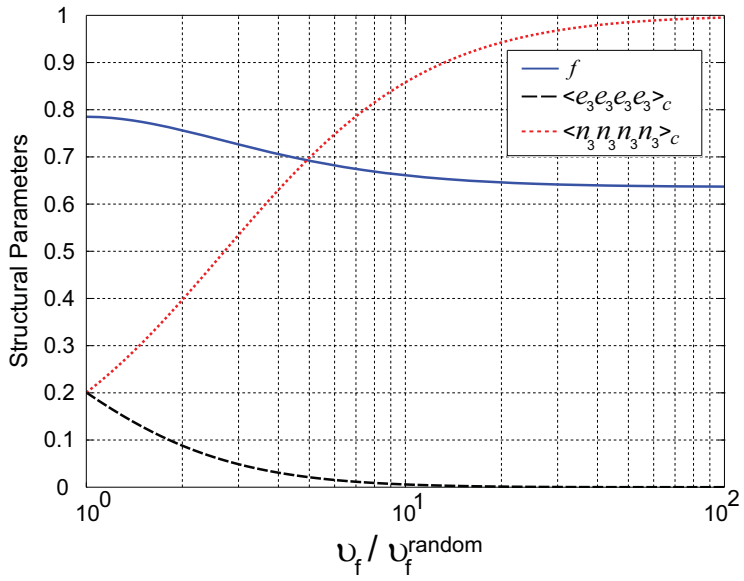

Figure 3.6: Structural parameters with respect to relative volume fraction in uniaxial compression.

$$\boldsymbol{F} = \text{diag}\left(1, 1, \upsilon_f^{random}/\upsilon_f\right) \tag{3.57}$$

where υ_f^{random} is the volume fraction for the initial random state. Considering a 3D initially random fiber mass and applying the deformation tensor on each fiber of the assembly, the orientation distribution function and structural tensors associated with the specific deformation can be calculated according to equation 3.45.

Orientation dynamics is modeled using equation 3.57, which is applied to each vector in the initially random network. Thereupon, orientation distribution function can be estimated and used in calculating f and the structural tensors $\langle n_3n_3n_3n_3\rangle_c$ and $\langle e_3e_3e_3e_3\rangle_c$ associated with the relative deformation. It should be noted that the simulation starts from a random state and the deformation is considered relative to this initial state. Numerical results for these calculations are shown in Figure 3.6.

In this case, 6000 random fibers were selected and demonstrated very good results in comparison to the boundary values of the parameters, which can be calculated exactly. Analytically, the values of f for three-dimensional random networks, $\upsilon_f/\upsilon_f^{random} = 1$, and the planar random ones, $\upsilon_f/\upsilon_f^{random} \gg 1$, are respectively $\frac{\pi}{4}$ and $\frac{2}{\pi}$ which are in excellent

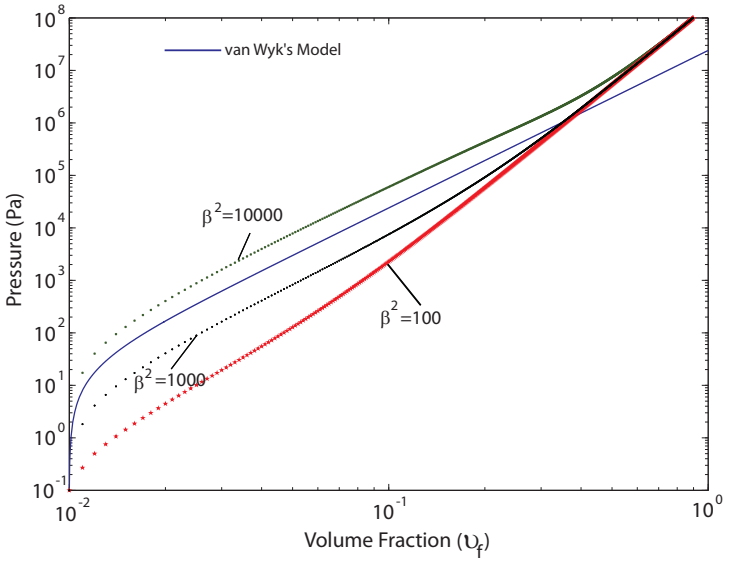

Figure 3.7: Comparison of van Wyk's and granular media-based model in case of spatial networks.

agreement with the obtained numerical results, i.e. 0.785 and 0.637. Change in orientation distribution of fibers for a typical deformation relative to the random initial state is depicted in Figure 3.2.

If the fiber segments are assumed to be loaded at their midspan in both torsion and bending deformation schemes, i.e. $k_b = k_t = 1$, the results can be compared with van Wyk's equation for different values of the crimp ratio β, as shown in Figure 3.7.

It is obvious that the obtained results are in relatively good agreement in comparison to van Wyk's model (equation 2.1) for $k_p = 0.01$, especially for volume fractions less than 0.1. For higher volume fractions, they follow distinct paths which can be justified by the change in the behavior of structure from a 3D assembly to a planar network. Figure 3.8 shows the comparison for the granular media-based model (equation 3.55) and Toll's model for 2D cases (equation 3.56) [110]. It demonstrates that they are in good agreement for high relative volume fractions in which the structure behaves like a planar assembly.

To examine applicability of the model in micromechanical modeling of felt, the parameters of the differential equation 3.55 should be identified by minimizing the root-mean-square error between the predicted macroscopic pressure and measured experimental data as the objective function. This can be done by an optimization method like Nelder-Mead Simplex algorithm in which the objective function is the mean squared error between the

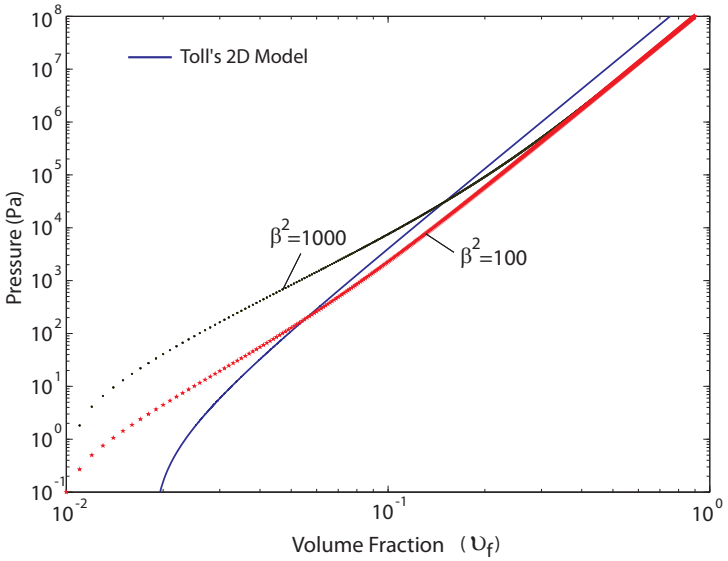

Figure 3.8: Granular media-based model in comparison to Toll's model in case of planar networks.

differential equation values and the experimental data.

For some experimental data, collected by Stamm [100] on different types of felt with various volume fractions, optimized parameters were estimated by minimizing the root-mean-square error between the observed experimental data and the predicted values from the differential equation 3.55. There is a good agreement between theory and experiment for the acquired set of parameters.

As shown in Figures 3.9 - 3.11, the identified parameter $k_t \simeq 0$ implies that effect of fiber torsion is negligible. In other words, bending of the fibers is the predominant deformation scheme in absorbing the external work done on the network. The value of k_b increases for felt with lower volume fraction, which means that bending elements have less compliance in case of lower volume fraction. It does not seem reasonable that the network behaves softer, but what is extremely important is that the assembly response depends not only on the mechanical properties of the energy elements but also on geometrical information like number of fibers, mean free fiber length, and fiber orientation distribution, which play key roles in resisting the external load on the fiber mass. Furthermore, lack of experimental data about the geometrical structure of the samples led us to use the same diameter and elasticity modulus for all of the felt samples, which will result in some error.

Note that the magnitudes of k_b and β are not realistic compared to other fiber assemblies

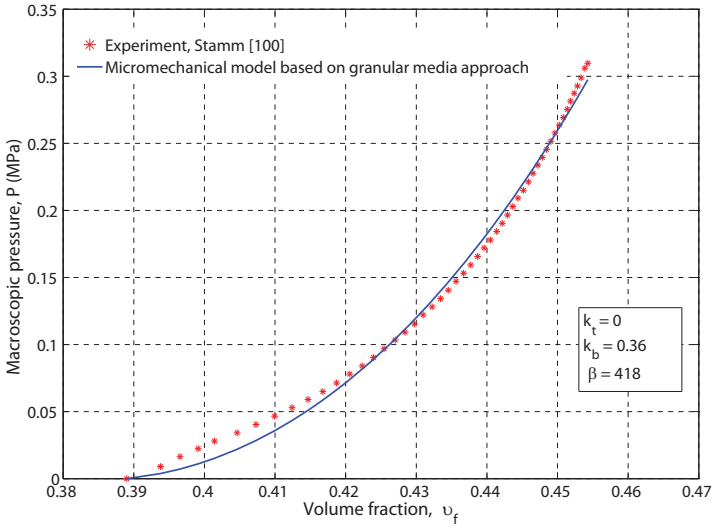

Figure 3.9: Compression of the piano hammer felt with $v_{f0} = 0.389$ in comparison to the granular media model.

with considerably lower volume fraction [1]. This supports the conclusion that all well-known mechanistic models, which have been effectively applied to many types of fiber masses, do not work for felt compression analysis [100].

3.2.3 A mechanistic approach based on binomial distribution of fiber contacts in random networks

As described thoroughly in Section 3.1.3, a binomial distribution of contacts in a fiber network can be a promising approach in constructing a micromechanical model for felt, as an alternative to the other procedures that were not able to reasonably follow the compression behavior of felt.

The relation between macroscopic pressure and bulk deformation in fiber networks was originally developed by van Wyk, based on fiber bending as the dominant microscale deformation scheme [115]. The general idea is to consider fiber segments as Euler-Bernoulli beam elements supported at numerous points of contact with other fibers, in which the segments could be straight [100, 110] or curved [11, 49, 56, 57] and boundary conditions at contact points could be estimated as simply supported, free [60], or built-in [74, 110, 115] ends.

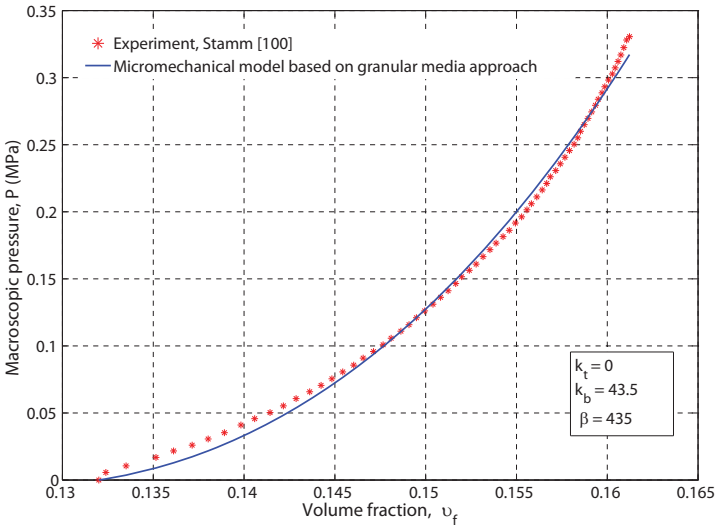

Figure 3.10: Compression of the soft red felt with $v_{f0} = 0.132$ in comparison to the granular media model.

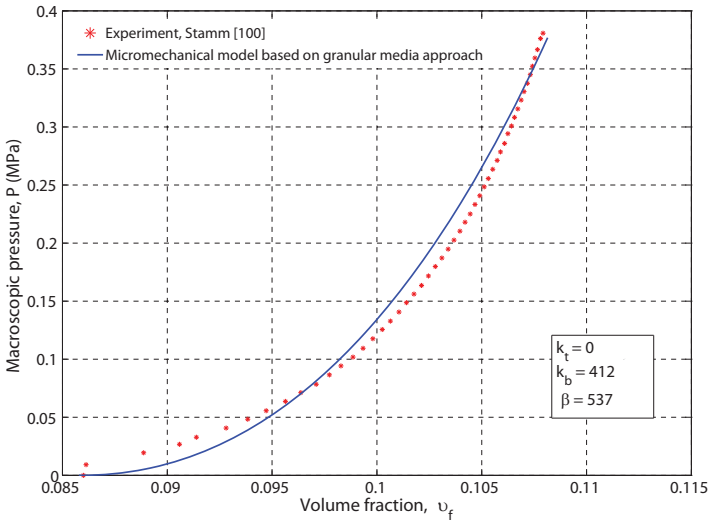

Figure 3.11: Compression of the moderate red felt with $v_{f0} = 0.086$ in comparison to the granular media model.

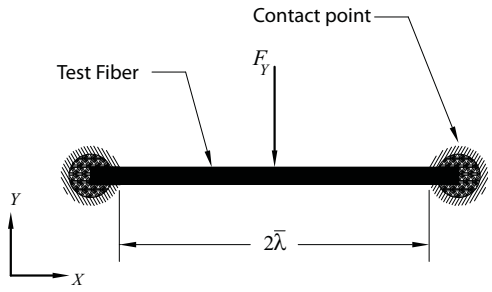

Figure 3.12: An equivalent fiber element model in microscale deformation of the network.

To develop a mechanistic model, a horizontal beam supported at contact points equally spaced at distance $2\overline{\lambda}$ apart is considered, along with built-in ends at non-sliding contact points, as shown in Figure 3.12. A transverse contact force F_Y acting at the midspan of the beam results in a deformation δ_Y according to beam formulas, based on infinitesimal strain theory, as

$$F_Y = \frac{192EI}{(2\overline{\lambda})^3}\delta_Y \tag{3.58}$$

where E is the modulus of elasticity of the fiber and I is the second moment of area of the fiber cross section.

If we consider a control volume with unit cross section area confined between two planes, both normal to X_3, at a distance equal to vertical projection of a random fiber, the pressure flowed into the network transfers to the contact forces between all interacting elements in the volume. Mathematically, the pressure P can be expressed as

$$dP = n_{\overline{\lambda}_j}\, dC_j = N_v\, V_{\overline{\lambda}_j}\, dC_j, \quad j = 3 \tag{3.59}$$

in which $n_{\overline{\lambda}_j}$ is the number of contact points in the volume $V_{\overline{\lambda}_j}$ with unit cross section area and the height $\overline{\lambda}_j$ equal to the mean projection of the random fiber length on direction j, and C_j is the contact force between interacting fibers in direction j. $V_{\overline{\lambda}_j}$ can be calculated simply as

$$V_{\overline{\lambda}_j} = 1 \times \overline{\lambda}_j = \overline{\lambda} \times K_j, \quad K_j = \int_0^{\pi}\int_0^{\pi} \Omega(\phi,\theta)\cos(\theta)\sin(\theta)\,\mathrm{d}\theta\,\mathrm{d}\phi \;\text{ for }\; j = 3 \tag{3.60}$$

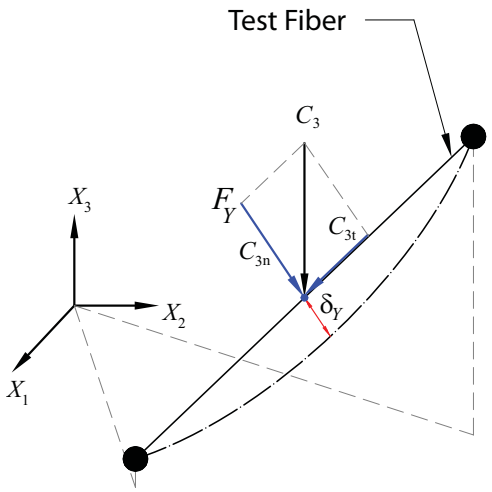

Figure 3.13: Deformation of a fiber beam model under contact forces.

where K_j is a structural parameter that averages the projection of mean fiber length in the third direction. The value of $\overline{\lambda}$ can be particularly expressed in terms of N_v as

$$\overline{\lambda} = \frac{\frac{l_f}{2}}{N_v V} \quad \rightarrow \quad \overline{\lambda} = \frac{2\, v_f}{N_v\, \pi d_f^2} \tag{3.61}$$

Consequently, $n_{\overline{\lambda}_j}$ in equation 3.59 will be

$$n_{\overline{\lambda}_j} = \frac{2 v_f}{\pi d_f^2} K_j, \quad j = 3 \tag{3.62}$$

The mean free fiber length $\overline{\lambda}$ in equation 3.58 can be evaluated by applying one of the procedures mentioned in Section 3.1.3, depending on the performance in different applications. It should be noticed that there is a relation between N_v and $\overline{\lambda}$ in terms of the structural features of the network, as proved in equation 3.61.

Finally, connection between bulk deformation and average contact force in the j direction, assuming an affine deformation rule, can be acquired using equation 3.58 and by matching Figures 3.12 and 3.13:

$$\delta_j = \frac{C_j \overline{\lambda}^3}{24EI} M_j, \quad M_j = \int_0^{\pi} \int_0^{\pi} \sin^2\theta\, \Omega(\phi,\theta) \sin(\theta)\, \mathrm{d}\theta\, \mathrm{d}\phi \quad \text{for} \quad j = 3 \tag{3.63}$$

Using the idea of a binomial distribution of the number of fiber contacts mentioned in Section 3.1.3 and the blocked fiber length (the length of fiber that has been already blocked by present contacts and is not available for a new contact to be formed), along with the theoretical differential relation between macroscopic pressure and bulk deformation 3.59, Neckář et al. [74] developed a modified pressure-volume fraction relation as follows:

$$P = K_p \left(\frac{\eta}{Q\gamma(1-\eta)} \right)^3 \left\{ (1-\eta) \left[2 + (3/2)\frac{\eta}{1-\eta} \right] - \frac{\eta}{Q\gamma v_f} \right\}, \quad \eta = 1 - e^{-Q\gamma v_f} \tag{3.64}$$

in which K_p is an uncertainty parameter, containing fiber modulus of elasticity, that accounts for all assumptions, approximations, and averaging errors that appear in the mechanistic model. $Q = 2$ for spatial random fiber networks [74]. As discussed in the next section, and to the knowledge of the author, it is the only model that is able to represent the compression behavior of felt and which gives realistic optimized parameters obtained in the process of the parameter identification problem.

3.3 Nonlinear hysteretic modeling of contacts in compressible interfaces

Hysteresis is an inevitable phenomenon in the compressional behavior of fiber assemblies, which has been confirmed by many experiments done on different types of fiber networks [80, 100]. The source of hysteresis can be friction between fibers sliding during network deformation, or structural damping in fiber deformation. Sliding between fibers is likely to happen, particularly in the compression of fiber assemblies at large deformations. It is crucial to note that due to friction, the evolution of network structure in loading and unloading stages would be fairly different, which indirectly contributes in generating hysteresis.

Recent experiments on a typical felt sample, presented by Masoudi et al. [66], reveals the existence of nonlinear hysteresis that is independent of speed of deformation, as shown in Figure 3.14. It means that a viscoelastic relation to include hysteresis is not suitable for felt compression analysis. Thus, the focus should be on the friction between interacting fibers, assuming to be Coulomb type in which the frictional force is proportional to the applied normal force, independent of the contact area.

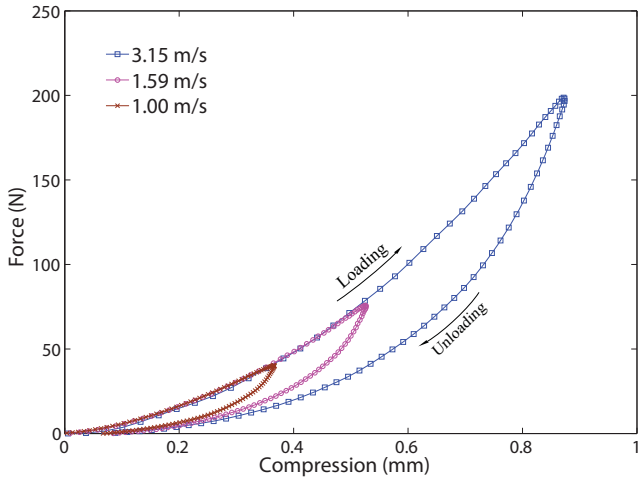

Figure 3.14: Loading and unloading curves for dynamic force-compression of a piano hammer impacting a rigid stop at various speeds [66].

In Section 3.3, a nonlinear hysteresis model for the compression of a fiber network, derived by Carnaby et al. [14], is presented. A novel technique, which is a creative combination of the mechanistic model presented by Neckář and the hysteretic approach proposed by Carnaby, is introduced to estimate the compression behavior of felt during the simulation of multibody systems with felt-lined interacting bodies.

To develop a mechanistic model of felt compression including nonlinear hysteresis, some key assumptions should be considered [14], referring to the schematic of frictional fiber interaction at a typical contact point as depicted in Figure 3.15:

1. There exist two types of fiber contacts: *sliding and non-sliding*. Depending on the orientation configuration of the fibers and the magnitude of normal force between interacting fibers, a criterion for fiber sliding can be established.

2. A subnetwork of fibers with non-sliding contacts absorb a proportion of the external work done on the bulk network as fiber bending elastic energy, discussed in Section 3.2.3.

3. Sliding contacts account for the remaining portion of the energy flow into the fiber mass in an irreversible form.

4. There is some withdrawal force on fibers, even in the absence of any external load

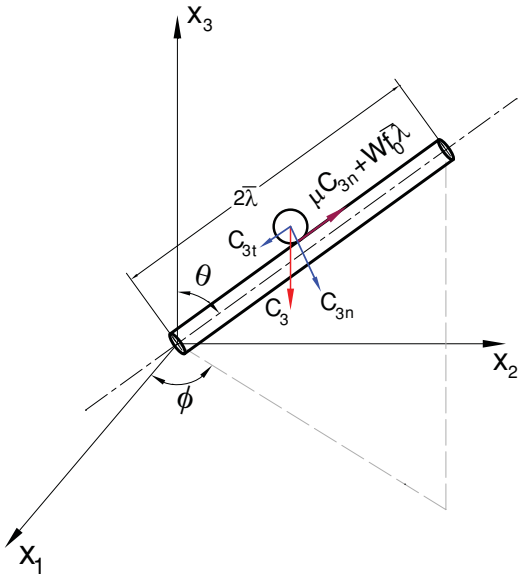

Figure 3.15: Contact forces developed in fiber contacts.

applied to the fiber mass, due to mutual interference and friction between interacting fibers.

5. The fibers slide when the tangential force exceeds friction force and withdrawal force between interacting fibers.

According to Coulomb's dry friction rule, the contacting fiber in Figure 3.15 starts to slide on the test fiber if the tangential force exceeds the microscopic resisting force between the interacting surfaces that are in atomically close contact. That is [14], when:

$$C_{jt} \geq \mu C_{jn} + W f_0 \overline{\lambda} \quad \Rightarrow \quad C_j \cos(\theta) \geq \mu C_j \sin(\theta) + W f_0 \overline{\lambda} \tag{3.65}$$

where C_{jt} is the tangential force on the test fiber, C_{jn} is the normal force, C_j is the contact force in direction j, μ is the coefficient of friction, and Wf_0 is the withdrawal force per unit length of fiber in the absence of external loads on the fiber mass.

The main source of withdrawal force comes from the fact that due to fiber interaction and friction, the fibers still have some residual bending energy in the absence of external loads on the fiber network [31, 32]. In fact, interactions between fibers prevent them

from reaching their lowest energy level. This interaction can be detected by single fiber withdrawal experiments. There are some experiments done by Grosberg and Smith [32] to estimate fiber withdrawal force. Theoretically, they proved that the withdrawal force Wf per unit length of fiber is approximately proportional to the external pressure P; Wf_0 is its finite value at $P = 0$.

According to equation 3.65, the critical angle θ_{crj} at which sliding occurs can be calculated:

$$\sin(\theta_{crj}) = \frac{-\frac{\mu W f_0 \overline{\lambda}}{C_j} \pm \left\{ \frac{\mu^2 W f_0^2 \overline{\lambda}^2}{C_j{}^2} - (1+\mu^2)\left(\frac{W f_0^2 \overline{\lambda}^2}{C_j{}^2} - 1 \right) \right\}^{\frac{1}{2}}}{1+\mu^2} \tag{3.66}$$

So, the fibers with polar angle less than θ_{crj}, which is a function of mean contact force C_j, slide. There is no slippage for the fibers with $\theta \geq \theta_{crj}$.

In general, the macroscopic external load on the network must flow through fiber contact points. If r_{sc} is the proportion of contact points that slide, the equation 3.59 can be rewritten in case of loading as[1] [14]

$$P_{loading} = (1 - r_{sc}) n_{\overline{\lambda}_3} C_{ns} + r_{sc} n_{\overline{\lambda}_3} C_s \quad \Rightarrow \quad P_{loading} = \sigma_{el} + r_{sc} n_{\overline{\lambda}_3} C_s \tag{3.67}$$

in which C_s is the average contact force per sliding contact point, C_{ns} is the the average contact force per non-sliding one, and σ_{el} is the elastic stress developed in the network during loading. For the unloading stage, it will be

$$P_{unloading} = (1 - r_{sc}) n_{\overline{\lambda}_3} C_{ns} - r_{sc} n_{\overline{\lambda}_3} C_s \quad \Rightarrow \quad P_{unloading} = \sigma_{eu} - r_{sc} n_{\overline{\lambda}_3} C_s \tag{3.68}$$

in which σ_{eu} is the elastic stress developed in the network during unloading. It is obvious that all parameters in equations 3.67 and 3.68 are different in the cases of loading and unloading, i.e. $\sigma_{el} \neq \sigma_{eu}$, and the effect of friction is not the same during loading and unloading.

Estimating θ_{cr} using equation 3.66, it is easy to find the proportion of fibers that slide:

[1] For simplicity in mathematical notations, we consider uniaxial compression in the third direction and ignore j in our formulations.

$$r_{sc} = \int_0^{\theta_{cr}} \int_0^{\pi} \Omega(\phi, \theta) \sin(\theta) \, \mathrm{d}\theta \, \mathrm{d}\phi \tag{3.69}$$

Contacting fibers slide when motion between the interacting fibers is impending; at this point, the magnitude of contact force approaches its threshold value, also called limiting friction:

$$C_s \cos(\theta_{cr}) = \mu C_s \sin(\theta_{cr}) + W f_0 \overline{\lambda} \tag{3.70}$$

Averaging all resistances per sliding contact points over the orientation space results

$$C_s = \int_0^{\theta_{cr}} \int_0^{\pi} \frac{W f_0 \overline{\lambda}}{\cos(\theta) - \mu \sin(\theta)} \Omega(\phi, \theta) \sin(\theta) \, \mathrm{d}\theta \, \mathrm{d}\phi \tag{3.71}$$

Furthermore, the corresponding mean non-sliding contact force can be evaluated as

$$C_{ns} = \frac{(P \pm r_{sc} n_{\overline{\lambda}_3} C_s)}{(1 - r_{sc}) n_{\overline{\lambda}_3}} \tag{3.72}$$

in which P can be either $P_{loading}$ or $P_{unloading}$, depending on the sign of macroscopic load rate that signifies the state of loading.

3.3.1 A general simulation of hysteresis in micromechanics of fiber networks

According to the algorithm presented by Carnaby and Pan [14], applying the above-mentioned procedure needs incremental and decremental approaches to cope with the large deformation of fiber masses. It is to be noticed that the goal is to simulate the relation between macroscopic pressure on the network and bulk deformation, which can be in the form of strain or volume fraction (equation 2.2).

In the compression stage,

- The parameters μ and $W f_0$ in equation 3.66 are constant and predefined; $\overline{\lambda}$ is a function of deformation.

- The value of critical angle θ_{cr} is calculated based on the current value of C_j, which is increased by successive incremental loading ΔC_j.
- Having θ_{cr} and the orientation distribution function, the proportion of contacts that slide (r_{sc}) is obtained using equation 3.69.
- The mean value of resistance per slipping contact points C_s (with incremental ΔC_s) is evaluated with equation 3.71.
- $n_{\overline{\lambda}_3}$, as introduced by equation 3.62, is a function of deformation or volume fraction and the structural parameter K_3. The dynamics of the network due to the deformation gradient tensor is estimated using the approach proposed in the granular media-based model (equation 3.57).
- Increments in macroscopic pressure ΔP can be achieved, considering $\Delta C_{ns} = \Delta C_j$, using equation 3.67 revised in incremental fashion:

$$\Delta P_{loading} = (1 - r_{sc}) n_{\overline{\lambda}_3} \Delta C_{ns} + r_{sc} n_{\overline{\lambda}_3} \Delta C_s \tag{3.73}$$

- Note that only non-sliding contact points control the microscale, and thus the bulk deformation of the network. Assuming affine deformation, the strain due to an increase of average force per non-slipping contact point can be calculated based on equation 3.63 in incremental form:

$$\Delta \delta_j = \frac{\Delta C_j \overline{\lambda}^3}{K_p EI} M_j, \quad j = 3 \tag{3.74}$$

  in which K_p is the uncertainty parameter that compensates for the unrealistic assumption that the test fiber is loaded at the midspan by the contacting fiber.

In the unloading stage, a decremental process should be used, i.e., with successive decreasing changes in contact force ΔC_j, using the same framework as for the compression stage. However, sliding contact points behave in a significantly different way due to principal changes in interaction forces at contact points, as explained next.

During unloading, the bending energy stored in the test fiber causes the contacting fiber to recover; it applies a normal force to the slipping fiber. Even in the absence of normal force, the contacting fiber does not move back up to the test fiber. So, it is fairly reasonable to use the same logic that Carnaby and Pan [14] assumed in the recovery stage,

namely that the sliding force C_s carries the resistance $Wf_0\overline{\lambda}$ at the interfaces. In other words,

$$C_s \cos(\theta_{cr}) = Wf_0\overline{\lambda} \tag{3.75}$$

This is in agreement with the withdrawal experiments that show that, in the absence of macroscopic load on the fiber mass, there exists some finite contact force at contact points. Consequently, the resistance force per slipping contact during unloading, averaged over the orientation space will be:

$$C_s = \int_0^{\theta_{cr}} \int_0^{\pi} Wf_0\overline{\lambda} \sec(\theta)\, \Omega(\phi,\theta) \sin(\theta)\, \mathrm{d}\theta\, \mathrm{d}\phi \tag{3.76}$$

along with the decremental unloading pressure

$$\Delta P_{unloading} = (1 - r_{sc}) n_{\overline{\lambda}_3} \Delta C_{ns} - r_{sc} n_{\overline{\lambda}_3} \Delta C_s \tag{3.77}$$

Carnaby and Pan [14] conducted some extensive investigations in applying the model to simulate compression hysteresis of several fiber networks with different volume fractions in various range of deformations. In the obtained stress-strain diagrams, non-sliding contact points (which reversibly absorb macroscopic energy applied on the network) produce different curves in compression and recovery stages. The proportion of contacts that slide and, particularly, asymmetry in structural parameter values during compression and recovery stages, were the main sources of hysteresis in the network.

Application of the iterative model in multibody dynamic simulations requires a different simulation procedure, considering that

1. In the simulation model by Carnaby and Pan [14], the start point of simulation is the incremental loading at microscale level, i.e. increasing or decreasing average contact force ΔC_j. This provides the required information to proceed to the next step, including calculation of critical angle of sliding, proportion of sliding contacts, value of resistance per sliding contact point, structural parameters, and finally pressure-deformation relation at the macroscale level.

2. Parameter identification using the current procedure requires an optimization scheme which is fairly complicated and computationally expensive. The lack of enough unknown parameters to be optimized reduces the chance of having reasonable numerical values for the identified parameters.

3. In multibody dynamic simulations, particularly in mechanistic modeling of piano action mechanisms, there exist two or more interacting bodies lined with fiber assemblies at interfaces. Hence, penetration of the two felt-covered contacting bodies at the point of contact, i.e. bulk deformation of the covering material, is the input and contact forces between the bodies should be evaluated and returned to the dynamic equations of the multibody mechanism to advance the simulation.

4. To keep the simulation time tractable in multibody dynamic models, interaction between components has to be modeled in a mechanistic fashion as well as simplified enough so that in each step of simulation time, contact forces can be calculated as a function of penetration depth between colliding objects at low computational cost and time.

3.3.2 A simulation of hysteresis in micromechanics of fiber networks, applicable in multibody dynamics

The micromechanical model presented in Section 3.2.3, based on a binomial distribution of the number of fiber contacts, combined with the compression hysteresis model built on fiber to fiber friction and structural parameter difference in loading-unloading stages, can be a promising approach in mechanistic modeling of multibody systems considering interactions between bodies lined with fiber networks. In fact, an algorithm has been developed to incorporate the hysteresis phenomenon into the micromechanical model using the experimental data for felt, thereby the generated model can be utilized in multibody dynamic simulations.

Experimental data extracted by Stamm [100], for compression tests on wool felt samples with different volume fractions, have been used as reference data in this research. According to the compression hysteresis model discussed in Section 3.3.1, the fiber network can be estimated by two subnetworks in resisting the load on the fiber mass, considering small deformations in each loading step:

- A subnetwork consisting of non-sliding contact points, for which the elastic behavior of the fiber assembly can be justified. Under these circumstance, there can be considered a phantom network with bonded contact points such that its compression response can be estimated by any of the methods described in Section 3.2.

- In contact points for which the tangential force exceeds friction plus the withdrawal force, the fibers slide and have no contribution in absorbing the energy flow into the network, produced by external work done on the fiber mass, in a reversible form.

Consequently, we need a framework to construct the nonlinear hysteretic model based on the experimental results, then apply it in dynamic modeling of multibody systems. As demonstrated in Figure 3.16, this is a two-step process:

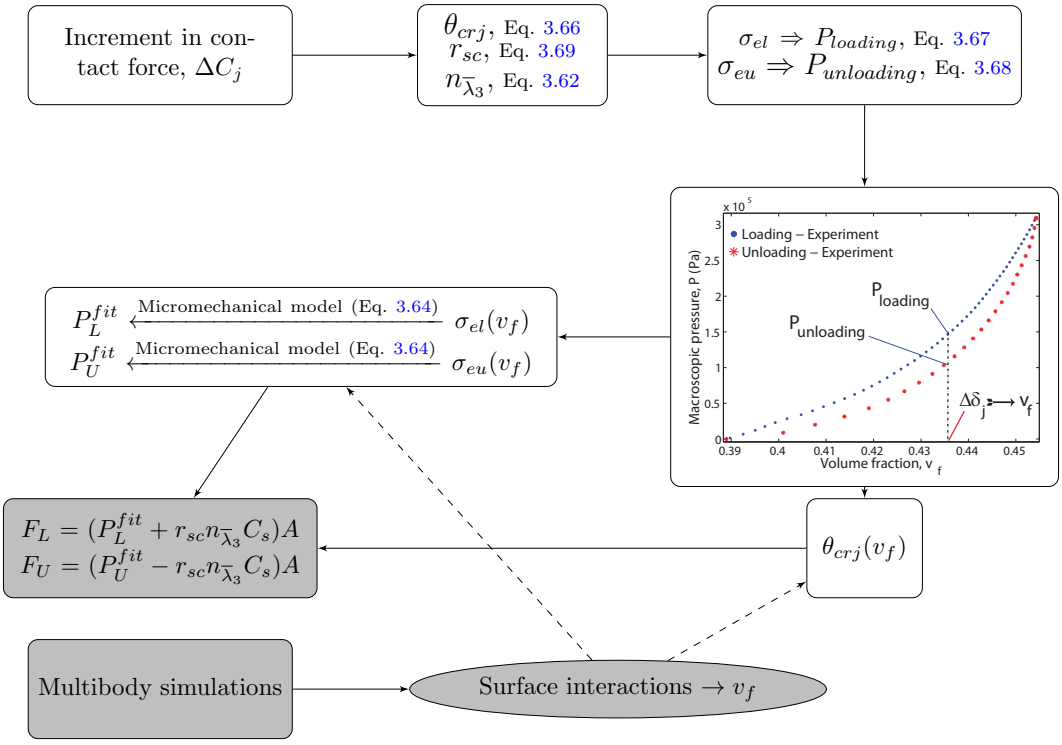

Figure 3.16: The procedure developed in applying the proposed micromechanical model for multibody dynamic simulations.

Micromechanical simulation:

A load increment of the mean value of contact force, ΔC_j, is considered, and the proportion of contact points that slide is calculated using equation 3.69. Accordingly, the loading pressure $P_{loading}$ and the elastic response σ_{el} can be calculated using equation 3.67. At this point, we use the deformation information from experimental data to update the network dynamics according to the volume fraction associated with the simulated pressure $P_{loading}$ on the network. The same process is followed for the recovery stage in evaluating $P_{unloading}$ and σ_{eu}, employing equation 3.68. This also gives the critical angle of fiber sliding θ_{crj} in

terms of volume fraction during loading and unloading, which will be used in the multibody simulations as a structural parameter.

Continuing the load increment, the elastic portion of macroscopic pressure in the experimental data is acquired so that we can treat the network as a bonded nonwoven one. The micromechanical model based on a binomial distribution of number of fiber contacts, represented by equation 3.64, is used to identify K_p and γ for the obtained elastic pressure data. Different optimized parameters signify different structural behavior of the network in compression-recovery stages. It is to be mentioned that the model is completely a mechanistic model based on bending of the network constituent fibers at the microscale. θ_{crj} is stored as table lookup to avoid iterations at each time step.

Multibody dynamic simulation:

In multibody simulations, the penetration between interacting bodies or change in volume fraction is calculated in each step. So, the elastic portion of bulk pressure can be acquired by the micromechanical model with identified parameters. Expressing the critical angle θ_{crj} of sliding as a function of volume fraction from our former analysis, the effect of friction and contribution of sliding points in the loading-unloading bulk pressure will be included by adding $r_{sc}n_{\overline{\lambda}_3}C_s$ to the obtained elastic portion σ_{el} in case of loading, and subtracting $r_{sc}n_{\overline{\lambda}_3}C_s$ from the elastic portion σ_{eu} in case of unloading, referring to equations 3.67 and 3.68. The procedure has been demonstrated in Figure 3.16; the above part of the flowchart (white blocks) shows the way that the elastic portion of loading and unloading curves is calculated for a specific range of deformation, and then the parameters of the micromechanical model equation are extracted, performing a parameter identification. The critical angle of sliding is evaluated at each volume fraction and attributed uniquely to the contact interface as a structural parameter for use in the next step. The obtained result is utilized in multibody dynamic simulations (grey blocks) to achieve the overall macroscopic loading (P_L) and unloading pressures (P_U), including the elastic portions (P_L^{fit} and P_U^{fit}) and the fiber to fiber friction contribution ($+r_{sc}n_{\overline{\lambda}_3}C_s$ and $-r_{sc}n_{\overline{\lambda}_3}C_s$), when deformation or volume fraction is known.

Simulation results obtained by minimizing the error between equation 3.64 and the elastic portion of the experimental data, extracted using the above-mentioned procedure, for four different samples of fiber assemblies, along with the identified parameters are shown in Figures 3.17 - 3.20. It is important to note that structural properties of the networks are different, from diameter and surface property of the fibers to manufacturing process and bulk properties. For instance, due to lack of information about fiber diameter in different samples, we considered fiber diameter for all samples to be the same as that of piano

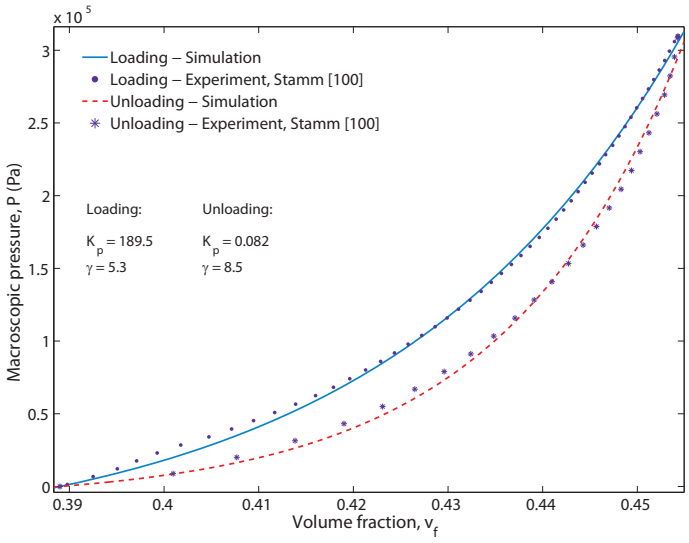

Figure 3.17: Loading and unloading experimental data for piano hammer felt with $v_{f0} = 0.389$, along with the identified parameters of the micromechanical model.

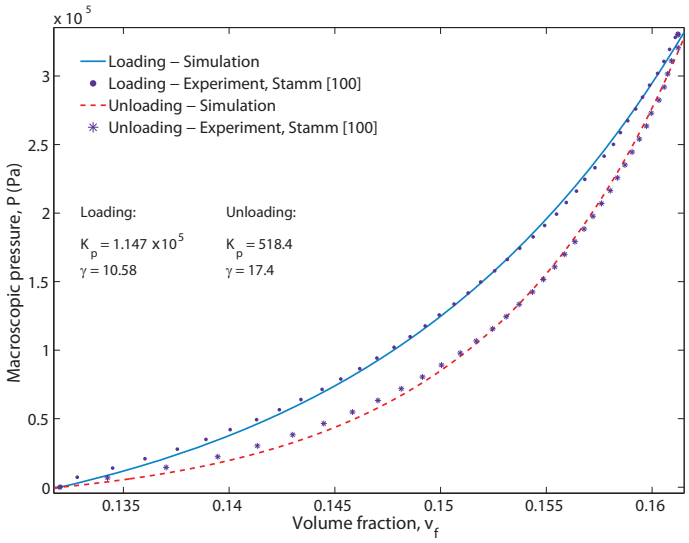

Figure 3.18: Loading and unloading experimental data for soft red felt with $v_{f0} = 0.132$, along with the identified parameters of the micromechanical model.

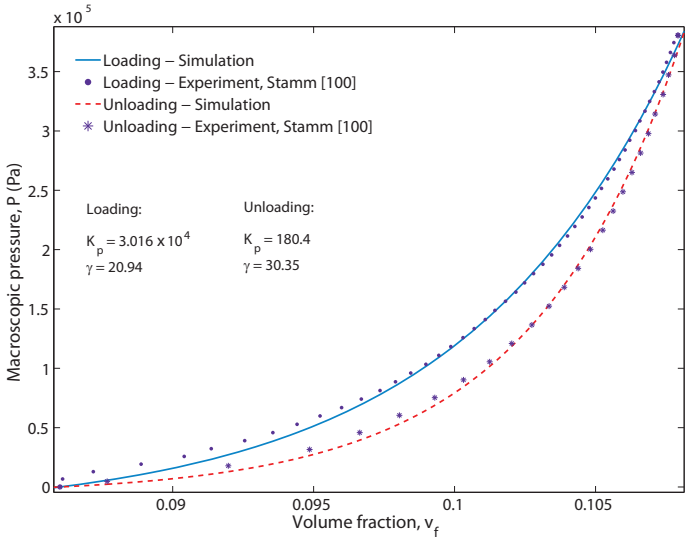

Figure 3.19: Loading and unloading experimental data for moderate red felt with $v_{f0} = 0.086$, along with the identified parameters of the micromechanical model.

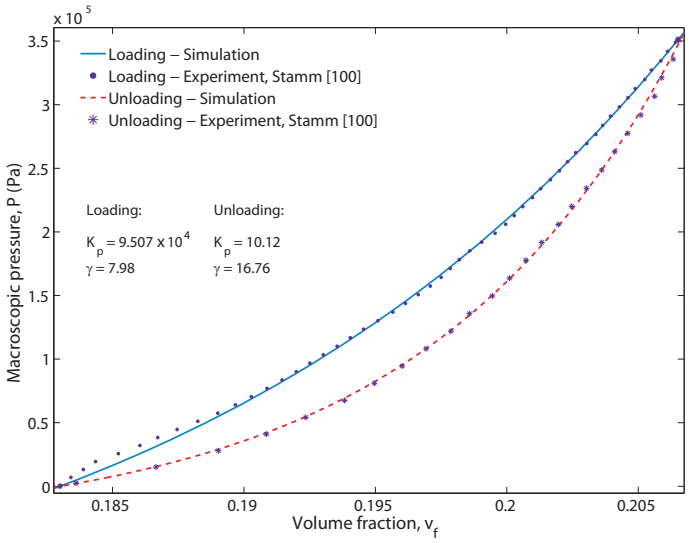

Figure 3.20: Loading and unloading experimental data for leather with $v_{f0} = 0.183$, along with the identified parameters of the micromechanical model.

hammer felt, which has been measured by SEM in our experiments. Therefore, comparing the results to find a traceable trend of the optimized parameters does not seem logical in this case. However, performing systematic experiments on different fiber assemblies with known geometrical and mechanical features is essential to analyze the physical significance of the identified parameters. The value of K_p and γ is relatively reasonable when compared to the other models that have been examined on different fiber assemblies [110, 115]. It is to be noticed that preforming complicated and detailed experiments to understand the structure and properties of different felts are required for high fidelity modeling.

3.4 Chapter summary

In this chapter, experimental and theoretical aspects of the micromechanical modeling of nonwoven fiber assemblies were discussed and investigated using different approaches. The microstructure of felt, as a typical fiber assembly, was examined by SEM to identify the structure of the fiber network and to measure some required parameters in developing a mechanistic model.

Microscopically, the number of fiber contacts plays a key role in constructing micromechanical models, based on the deformation of imaginary straight fibers at the micro level, independent of the predominant deformation schemes. Accordingly, different statistical techniques in determining the number of fiber-to-fiber contacts were introduced and validated for specific types of felt samples that have been applied in piano action mechanisms. Moreover, the effect of some deformation schemes in resisting macroscopic loads was studied, confirming that bending of the fibers is the main structural deformation in storing the energy flows into the network.

A granular media model, along with an initially random network, has been applied and validated experimentally using a typical optimization procedure called Nelder-Mead Simplex algorithm. Nonlinear hysteresis was included in the micromechanical model, considering two subnetworks during compression of the fiber mass. In each deformation stage, the proportion of fibers that do not slide behave like a bonded fiber network, reversibly absorbing the energy flowing into the network. Fiber sliding, considering Coulomb friction criterion, is one of the sources of nonlinear hysteresis in compressional behavior of such networks, which was incorporated based on fiber to fiber friction. It is particularly important to note that the change in structural parameters during loading and unloading stages was the main source of hysteresis in the network.

A binomial distribution of fiber contacts in conjunction with the Coulomb friction assumption in fiber sliding has been examined for different samples to affirm the applicability

of the micromechanical model for felt. Furthermore, an experimental-based procedure was introduced to apply the model in multibody dynamic simulations, in which the tractability of simulation time during interactions between colliding bodies has been a challenging issue.

In the next chapter, dynamic simulation and experimental validation of a vertical piano action will be thoroughly presented.

Chapter 4

Mechanistic Model for the Dynamic Simulation of a Vertical Piano Action

A piano action is a mechanism that transmits the force applied on a piano key to the felt-covered hammer that strikes the strings and produces a desired sound. The hammer flies freely from the mechanism immediately before making contact with the strings so that it can rebound freely, thereby allowing the strings to continue vibrating. The interconnected bodies of the action must satisfy geometric and dynamic requirements in order to transfer the expected motions. The connections between bodies are formed by contact surfaces lined with felt to provide a softer feel and reduce mechanical noise in the action. Consequently, an accurate simulation model must include the contact mechanics in order to accurately study the mechanism.

Modern pianos are categorized into two main configurations: the grand piano and the upright piano. In grand pianos, the frame and strings are oriented *horizontally* and the strings, extending away from the keyboard, are struck from *below*. A vertical, or upright, piano is more compact because the frame and strings are oriented *vertically* behind the keyboard, requiring an action with hammers that strike the strings from the *front*. It is considered to be more difficult to produce a sensitive piano action with horizontally moving hammers, possibly because the hammer return is dependent on springs, which are prone to wear. The development of a simulation model for the vertical action will provide a tool for exploring these factors and investigating why pianists seem to feel better control with a good grand piano action than with a vertical action.

The research presented here is based on the configuration of two well-established commercial vertical piano actions: the Steinway Model 45 (Figure 4.3) and the Essex EUP-123

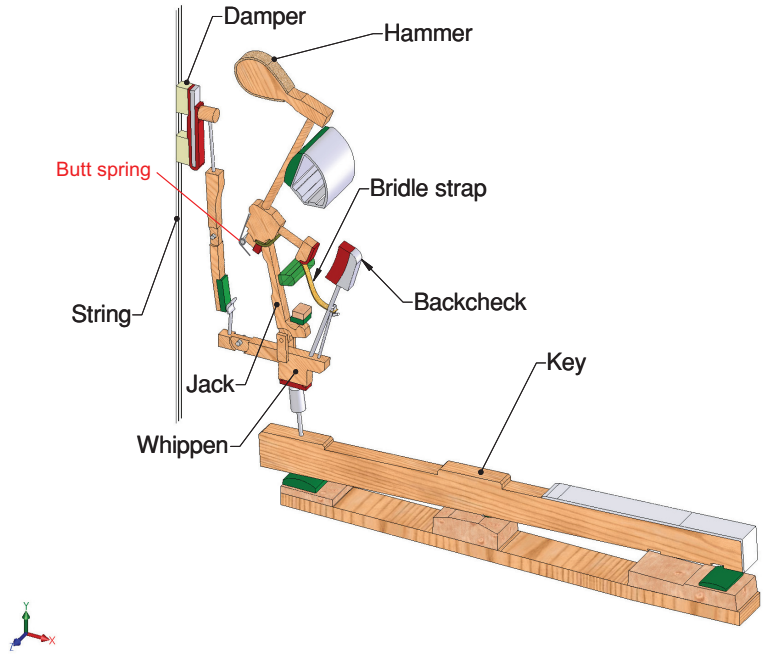

Figure 4.1: SolidWorks 3D model, components, and configuration of a typical upright piano action mechanism (Essex EUP-123).

(Figure 4.1). The results will generally apply to other vertical actions with similar geometry and components as those shown in Figure 4.1.

The motivation for this modeling project includes several applications that are of interest, for instance, to piano manufacturers:

1. Measuring the effect of mechanism parameters, such as component masses, geometry, and materials, on the feel of the action.

2. Understanding action designs better for improving manufacturing process of the action components and mechanism in a more effective fashion.

3. Increasing the life of the action components by predicting the amount and type of force exerted on them.

To achieve these goals, the velocities and accelerations of each body, especially when they are in contact, must be calculated. In order to design components, the magnitudes

of forces and torques on each body must be determined. Therefore, a dynamic analysis of the system will be the first step. Since the kinematic constraints of the mechanism at the contact surfaces are not simple ones (i.e., the different bodies are not always in contact during the action of the mechanism and allow for the bodies to separate), a continuous analysis method has been used to model the impact, treating the contacts as coupled applied forces during the contact period.

Previous investigations have focused on grand piano actions; the vertical mechanism has been ignored by researchers. This work presents a model of a typical vertical piano mechanism. The effect of introducing realistic model considerations, like hammer shank and backcheck wire flexibility, in the dynamic response of the action is examined. The dynamic equations of motion are derived using parameters obtained from a real action mechanism. The results of simulations with prescribed input force profiles applied at the key front are presented and discussed to verify the accuracy of the regulation process. Moreover, experimental data obtained from high-speed videos of real action behavior are used to understand the precise duties of each body in the action. The functions of the butt spring and bridle strap, two components that are not present in the grand piano action, are analyzed through simulation and will be evaluated through experiments. Incorporating a micromechanical contact model into the dynamic modeling of multibody systems is presented, and its application to the development of a fully mechanistic vertical action model will be discussed.

4.1 Dynamic model of a vertical piano action

4.1.1 Vertical piano action mechanism

A schematic of the vertical piano action is shown in Figure 4.2. The mechanism consists of five main bodies (the key, whippen, jack, hammer, and damper), all of which perform important functions during the key strike. All of these bodies are made of wood, typically hard maple or a similar species, and softwood for the key. Different types of felt or leather are used at the various locations where bodies come into contact.

When pressed, the key rotates clockwise (in Figure 4.2) about the balance rail pin and causes the capstan located at the other end of the key to move upward. The capstan pushes the whippen at the whippen cushion, causing the whippen to rotate counterclockwise about its ground-fixed pin. The pin joint of the jack is mounted on the whippen. The top of the jack is in contact with the hammer at the leather surface on the butt, so the motion

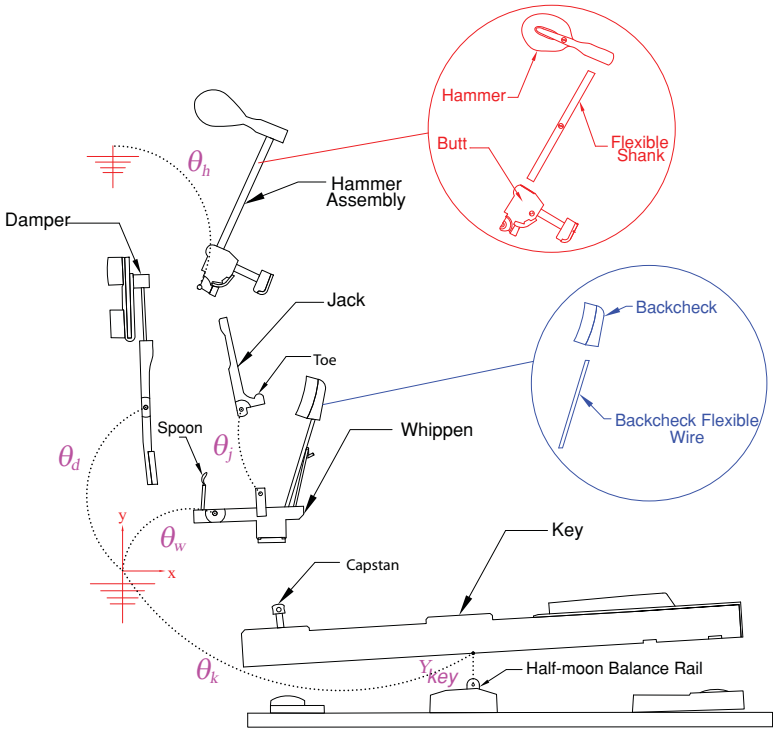

Figure 4.2: Schematic of the vertical piano action and its components, including rigid-body generalized coordinates, and exploded views of the hammer and whippen assemblies.

of the whippen causes the hammer to rotate counterclockwise toward the vertical string. At a pre-determined location of the hammer before it strikes the string, the toe of the jack comes into contact with the let-off button, causing the jack to rotate clockwise in the whippen frame, thereby releasing the contact with the hammer so that it (the hammer) can fly freely. The hammer strikes the string, rebounds back, and is captured on the backcheck with a high coefficient of friction to prevent it from re-striking the string. Furthermore, when the key is pressed, the damper spoon on the whippen comes into contact with the damper lever, causing it to rotate clockwise to remove the damper from the string. This motion allows the string to vibrate freely until the key is released and the damper resumes its contact with the string. The bridle strap (shown in Figure 4.1) is loosely attached between the hammer butt and the bridle strap wire mounted on the whippen close to the back check wire. This component prevents the jack from slipping underneath the hammer butt felt when the key is removed; however, under some conditions, the bridle strap may also briefly be involved in the dynamics of the key strike. Another component of great importance in the vertical action is the butt spring, which applies a clockwise torque to

the hammer butt.

4.1.2 Multibody dynamic model

To study the dynamic behavior of the vertical piano action, a typical mechanism was selected: that of the Steinway Model 45 vertical piano action. In this chapter, the motion dynamics of the five main bodies in the action, along with the physical interaction between components, will be developed and thoroughly analyzed. Some simplifications have been adopted in the past to reduce the complexity of the initial modeling attempt [65]:

- All five main bodies are considered to be rigid.
- In reality, pin joints are felt bushings exhibiting friction, which is included in the model, as well as some minor translational movement, which is ignored. In other words, the joints are approximated by ideal revolute joints with friction.
- The key pivot in the real action is a free contact on a felt pad, guided by a pin that prevents lateral motion. This joint is approximated by a simple revolute joint in the first modeling attempt, as presented in [65].
- Hammer shank and backcheck wire are assumed to be rigid.
- Following the same simplifications used in [36, 41], the flexible string is initially considered to be a rigid stop to avoid the inevitable complexity involved in modeling and incorporating the vibrating string.

To increase the fidelity of the model developed in the current work, the interaction between the hammer and a real string is included in the overall dynamic equations, which allow us to evaluate the effect of the string oscillations on the dynamic behavior of the action mechanism. In an attempt to build a more realistic model, the flexibility of the hammer shank and backcheck wire will be introduced and compared with experiments, as significant vibrations due to the flexibility of these components were visually confirmed in the high-speed videos obtained during the experiments. Furthermore, a sophisticated key pivot model is considered, capturing the rotational motion as well as the vertical translation of the key when it lifts off the balance rail during certain key strokes. The key pivot model adopted herein is a modified version of the revolute-prismatic joint introduced by Izadbakhsh [40].

The governing equations of motion in multibody systems can be formulated by applying several common methods in dynamics, such as the virtual work approaches and the techniques developed by Lagrange and Kane [46]. The graph-theoretic method (GTM) is a simple and systematic approach to produce mathematical models of multibody systems [69]. The GTM is based on a very methodical approach, which can be used to construct the dynamic equations of the vertical action mechanism using the topological graph of the system. This technique is particularly appropriate for multibody dynamics formulations, as very efficient computer algorithms can be designed by separating the topological equations of the mechanism from the constitutive equations.

Graph-theoretic approach

The GTM uses linear graph theory to represent the interconnections between objects in a given system, using mathematical structures. The physical characteristics of the bodies in a multibody system are related to the edges of the graph according to terminal equations that define the physical behavior of the components. In the graph of the action shown in Figure 4.3, the ground is assumed to be an inertial reference frame, and the motion of each body is tracked relative to a Cartesian reference frame attached to the ground datum node. Various types of graph edges are employed to represent the action components: edges assigned to rigid bodies, starting from the datum node and ending at the node representing the center of mass of a body, describe masses, moments of inertia, and gravitational forces acting on the body; edges at significant points on each body are used to represent the interactions between bodies at their contact locations, including forces and kinematic relations; edges representing kinematic revolute/prismatic joints connect the points at which the bodies are pinned; and edges that define contacts between bodies at the points of collision (not shown in Figure 4.3).

Referring to Figure 4.3, the "body-fixed vector" edges (rigid-arm elements), which represent the location of specific points on each body with respect to the center of mass node, are defined to determine the positions and velocities of all contact locations. These quantities are required in order to calculate the forces resulting from the contacts. Moreover, note that the key, whippen, hammer, and damper are attached to the ground by simple revolute joints; the jack is similarly attached to the whippen. An external time-dependent force, called the blow force, is applied on the key front at the approximate location where a pianist's finger would strike.

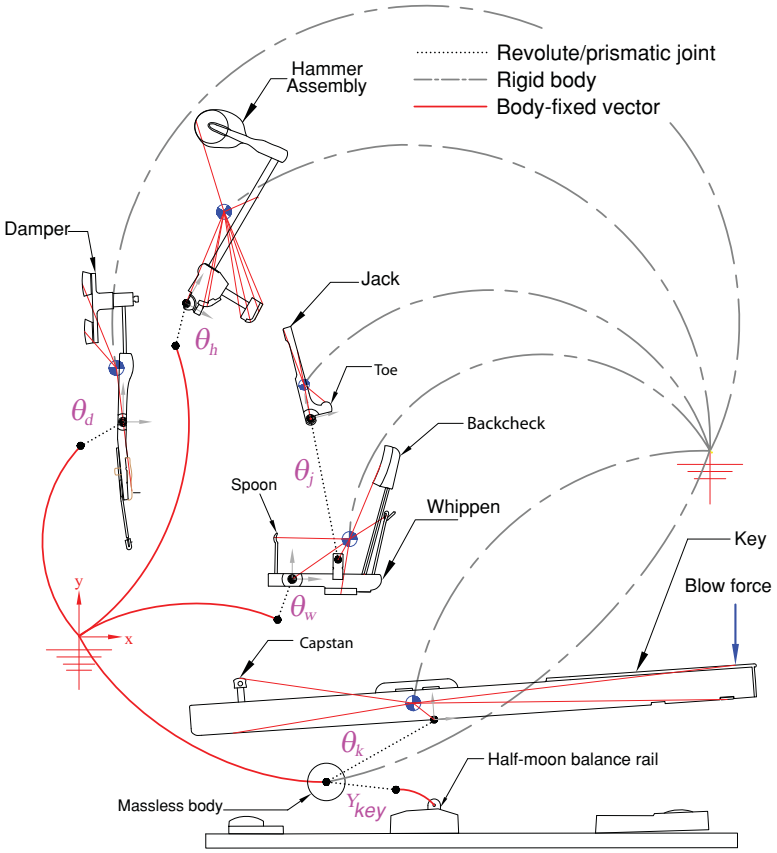

Figure 4.3: Graph of a typical vertical piano action mechanism (Steinway Model 45), including generalized coordinates for rigid-body motions of its main components.

Flexibility in backcheck wire and hammer shank

According to preliminary experimental results presented by Masoudi et al. [65], it can be concluded that the flexibility of the backcheck wire has a significant effect on the dynamic behavior of the hammer, especially when it strikes the string and bounces back on the backcheck. In this case, due to the flexibility of the backcheck wire, the angular rotation profile of the hammer reveals a damped harmonic motion before it is stopped completely by the backcheck. To represent this phenomenon, the backcheck wire was modeled as a flexible shank and considered as a separate body in DynaFlexPro, the symbolic GTM-based software used in this work. The partial differential equations (PDEs) obtained, which govern the dynamic behavior of the flexible backcheck wire as a continuous system, were converted to ordinary differential equations (ODEs) by a discretization method (the

Rayleigh–Ritz approach) in the software. In this work, Taylor polynomials have been used in the following Rayleigh–Ritz scheme:

$$U_{fw}(x,t) = \sum_{n=1}^{n_U} u_{fw}^n(t) x^n \tag{4.1}$$

$$V_{fw}(x,t) = \sum_{n=1}^{n_V} v_{fw}^n(t) x^{n+1} \tag{4.2}$$

where x corresponds to the distance along the centerline axis of the flexible wire measured from its connection point with the whippen, as shown in Figure 4.2; $u_{fw}^n(t)$ and $v_{fw}^n(t)$ are elastic generalized coordinates in the longitudinal and lateral directions, respectively; and n_U, n_V are the number of elastic generalized coordinates used for the two deformation variables. Increasing the number of elastic coordinates used in the formulation increases the number of vibration modes that can be captured in the motion of the flexible beam.

A precise analysis using a high-speed video camera and tracking specific points on the hammer and its shank confirmed the existence of significant vibrations in the hammer head. These vibrations are particularly noticeable at the beginning of the key stroke, where the components are accelerating rapidly, and during hammer-string impact, after which point the hammer butt strikes the backcheck very quickly. This vibration could be due to flexibility in the hammer shank, or could be a result of all the components (including whippen and key) reacting to the hammer-backcheck impact. Vyasarayani et al. [118] have studied the effect of vibrations due to hammer shank flexibility on the hammer-string interaction and subsequent string motion in a typical grand piano action. The simulation results from the vertical action revealed that the hammer shank flexibility could affect the impact speed of the hammer butt and backcheck, thereby the stop position of the hammer on the backcheck. Accordingly, we use the same approach to include the hammer shank flexibility, considering the same continuous system assumptions as for the backcheck wire in the action dynamic model:

$$U_{fs}(x,t) = \sum_{n=1}^{n_U} u_{fs}^n(t) x^n \tag{4.3}$$

$$V_{fs}(x,t) = \sum_{n=1}^{n_V} v_{fs}^n(t) x^{n+1} \tag{4.4}$$

where the variables are defined as in equations 4.1 and 4.2, but for the hammer shank.

Bridle strap and butt spring models

A bridle strap tension test using an Instron micro-testing machine indicates that the force-displacement behavior of this component is nonlinear. The bridle strap restrains the motion of the hammer when more violent blow inputs are applied, such as repeated or staccato (short and detached) notes. Thus, the bridle strap can be represented in the dynamic model as a nonlinear one-sided actuator, and implemented using the following nonlinear stepwise function:

$$f_{bs}(t) = \begin{cases} f_{fit}(\Delta_{bs}), & \text{if } D_{bs} > L_{bs} \\ 0, & \text{if } D_{bs} \leq L_{bs} \end{cases} \tag{4.5}$$

where f_{bs} is the bridle strap force, f_{fit} is the cubic fit to the experimental data generated by the tension test, D_{bs} is the distance between the points on the bridle strap wire and hammer butt check to which the strap is attached (shown in Figure 4.1), L_{bs} is the undeformed length of the strap, and $\Delta_{bs} = D_{bs} - L_{bs}$ is the elongation of the strap. In terms of modeling, the force applied by the bridle strap can be generated by attaching a spring between the attachment points in the DynaFlexPro action model, defining its nonlinear compliance according to equation 4.5.

The butt spring, supported at the ground and acting on the hammer butt, is represented by a simple torsion spring element. The butt spring helps the hammer fall back to its rest position at the hammer rest rail, particularly when the hammer must overcome friction in its ground-fixed joint. The nonlinear behavior of the spring has been characterized by estimating the torque-angular deformation relation using an Instron micro-testing machine.

Key-balance rail joint model

There is a translational degree-of-freedom between the key pivot and the ground along the balance rail pin, which makes the joint model more complicated than a simple revolute joint. According to [119], "this is a perfectly round pin driven firmly in the balance rail. The bottom of the hole in the key fits closely around the balance pin; at the top, it is the shape of a mortise, parallel with the key, which allows the key to move only in the direction intended. The mortise in the wooden cap on top of the key at this point is lined with bushing cloth which holds the key in position laterally, and prevents looseness and rattling, yet allows the key to move easily".

To model the atypical joint between the key and ground, two distinct motions must be considered: rotation about the z-axis and translation along the y-axis (see Figure 4.5).

In the simulation model, the joint is added by attaching the key to a massless body at its pivot position with a simple revolute joint, and confining the massless body to move vertically with respect to the center of the balance rail pin (using a prismatic joint). In addition, the key interacts with the balance rail through a contact interface.

4.1.3 Governing differential equations including hammer-string interaction

The differential equations governing the dynamic behavior of the whole system consist of ordinary differential equations (ODEs) describing the motion of the action mechanism, which are highly nonlinear and also in hybrid form, in the sense that rigid body motions are described by time-varying coordinates and the elastic motions are represented by time- and space-varying coordinates, and partial differential equations (PDEs) describing the behavior of the string. Interaction between the hammer and the string is realized by introducing the obtained string equations into the dynamic equations of the mechanism. A finite-time impact between the hammer and the string is considered as the input excitation of the string.

Multibody dynamic equations for the action mechanism

DynaFlexPro (DFP) [42] is GTM-based software designed for facilitating the dynamic simulation of mechanical multibody systems. DFP utilizes a graphical user interface for defining the component parameters and interconnections of the system. The GTM method is used to automatically generate symbolic equations governing the dynamic behavior of the system. The equations generated by DynaFlexPro are optimized, and the resulting code is suitable for real-time simulations. Furthermore, flexibility of the components can be introduced simply by adding a flexible body to the mechanism in the software GUI. The system of equations obtained for the vertical action model is a highly nonlinear system of twelve ODEs in the following form:

$$\boldsymbol{M}\ddot{\boldsymbol{q}} = \boldsymbol{F}(\boldsymbol{q}, \dot{\boldsymbol{q}}, t) \tag{4.6}$$

where $\boldsymbol{q}$ is the column matrix of generalized coordinates, $\boldsymbol{M}$ is the mass matrix, and $\boldsymbol{F}(\boldsymbol{q}, \dot{\boldsymbol{q}}, t)$ is the column matrix of generalized forces containing quadratic velocity terms, gravitational terms, contact forces, and friction torques. As illustrated in Figure 4.3 for the multibody system, the generalized coordinates are defined as follows:

$$\boldsymbol{q} = \begin{bmatrix} \boldsymbol{q}_{\text{rigid}} & \boldsymbol{q}_{\text{flex}} \end{bmatrix}^T \tag{4.7}$$

where $\boldsymbol{q}_{\text{rigid}}$ are the time-dependent generalized coordinates associated with rigid-body motions of the five main bodies in the action:

$$\boldsymbol{q}_{\text{rigid}} = \begin{bmatrix} Y_{key}(t) & \theta_d(t) & \theta_k(t) & \theta_h(t) & \theta_w(t) & \theta_j(t) \end{bmatrix} \tag{4.8}$$

$Y_{key}(t)$ is the translational displacement of the key on the half-moon balance rail bearing; $\theta_d(t)$, $\theta_k(t)$, $\theta_h(t)$, and $\theta_w(t)$ are the counterclockwise rotation angles (in radians) of the damper, key, hammer, and whippen, respectively, as measured from the ground frame; and $\theta_j(t)$ is the angle of the jack with respect to the whippen rigid body-frame, as measured counterclockwise. $\boldsymbol{q}_{\text{flex}}$ are the time-dependent generalized coordinates representing the flexible motion of the hammer shank and backcheck wire:

$$\boldsymbol{q}_{\text{flex}} = \begin{bmatrix} u_{fw}(t) & v^1_{fw}(t) & v^2_{fw}(t) & u_{fs}(t) & v^1_{fs}(t) & v^2_{fs}(t) \end{bmatrix} \tag{4.9}$$

in which $u_{fw}(t)$ and $u_{fs}(t)$ are the longitudinal elastic coordinates and $v^i_{fw}(t), {}_{i=1,2}$ and $v^i_{fs}(t), {}_{i=1,2}$ are elastic coordinates in the lateral direction for the flexible backcheck wire and flexible hammer shank.

The symbolic equations, assuming the string is replaced with a rigid, stationary body, were solved directly in Maple using a Livermore stiff ODE solver based on backward differentiation formulas and using chord iteration with an internally generated (difference quotient) full Jacobian [64]. The interaction between the hammer and a real string is then introduced by coupling the mechanism's ODEs and the string's PDEs, as discussed in the next section, to study the effect of string rigidity and its oscillations on the general behavior of the action. To include contact mechanics in the governing differential equations, a graph edge is introduced in the model for each contact interface; contact forces are determined at each time step based on the calculated position and velocity information of the contact surfaces.

Formulation of string dynamic equation

Dynamic modeling of the interaction between the hammer and string follows the method presented by Vyasarayani et al. [118]. The partial differential equation governing the

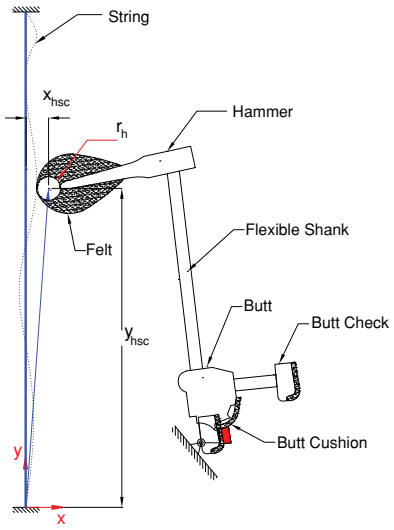

Figure 4.4: Schematic of hammer-string interaction in the vertical action model.

dynamic behavior of a vertical elastic stiff string, modeled as a continuous system, when excited by an impulse force at a specified location along the string, is as follows:

$$\mu_s \frac{\partial^2 x}{\partial t^2} + E_s I \frac{\partial^4 x}{\partial y^4} - T \frac{\partial^2 x}{\partial y^2} = f_n(t)\delta(y - y_{hsc}) \tag{4.10}$$

in which μ_s is the linear mass density, E_s is the Young's modulus of elasticity of the string, I is the second moment of area of the cross section, T is the tension in the string, x is the lateral deformation of the string, y is the distance from one end of the string along its axis in the initial (undeformed) state, and δ is the Dirac delta function. $f_n(t)$ is the normal impact force produced by the hammer-string interaction at the point of contact, and (x_{hsc}, y_{hsc}) is the spatial coordinate of the center of the hammer head virtual circle with respect to the string reference frame, as shown in Figure 4.4. The contact force is determined using the novel contact force model developed in this work, which will be discussed in detail in Section 4.1.4:

$$f_n(t) = \begin{cases} F_{contact}(\Delta, \nu_n, C_{params}), & \text{if } \Delta > 0 \\ 0, & \text{if } \Delta \leq 0 \end{cases} \tag{4.11}$$

where $\Delta = x(y_{hsc}, t) - (x_{hsc} - r_h)$ is the dynamic penetration depth of the string in the

hammer head felt, which is obviously a function of time; r_h is the equivalent radius of the hammer head virtual circle required to detect and evaluate the contact force; ν_n is the relative normal speed between the hammer and string, which determines the phase of loading and unloading between the contact surfaces; and C_{params} are the contact parameters for loading and unloading fitting curves, which were obtained through compression hysteresis experiments for hammer-string interaction.

To build the the dynamic equations for the whole system, the string equation must be discretized and converted into ODEs to be coupled with the dynamic equations of the action mechanism. To this end, the elastic displacement of the string can be expressed as follows:

$$x(y,t) = \sum_{j=1}^{N_m} \phi_j(y)\eta_j(t) \tag{4.12}$$

in which $\phi_j(y)$ is the jth undamped mass-normalized mode shape of the pinned-pinned string, $\eta_j(t)$ is the jth modal coordinate of string vibration, and N_m is the number of modes considered in modeling the string vibrations. The second-order ODEs governing the dynamic behavior of the string can be obtained by applying orthogonality conditions between mode shapes, then simplified to obtain the following [118]:

$$\ddot{\eta}_j + 2\xi_j w_j \dot{\eta}_j + w_j^2 \eta_j = \phi_j(y_{hsc}) f_n(t) \tag{4.13}$$

in which ξ_j is the modal damping. The closed-form expressions for natural frequencies and mass-normalized mode shapes given by Fletcher [25] are as follows:

$$w_j = \frac{\pi j}{L_s}\sqrt{\frac{T}{\mu_s}(1+\varepsilon\pi^2 j^2)} \tag{4.14}$$

$$\phi_j(y) = \sqrt{\frac{2}{\mu_s L_s}}\sin\left(j\pi\frac{y}{L_s}\right) \tag{4.15}$$

where $\varepsilon = \pi d^4 E_s/64L_s^2 T$ is called the inharmonicity index, d is the string diameter, and L_s is the string speaking length. Pinned-pinned boundary conditions for the string are given by $x(0,t) = x(L,t) = 0$ and $x_{yy}(0,t) = x_{yy}(L,t) = 0$ ($x_{yy} \triangleq \frac{\partial^2 x}{\partial y^2}$). Numerical values for all string parameters used in the simulation are provided in Table 4.1.

Table 4.1: String parameters (Steinway & Sons 45 upright piano, note 40)

Parameter	Description	Numerical value
d	diameter	0.99 mm
T	tension	654 N
L_s	speaking length	0.6315 m
ξ_j	modal damping	0.07
μ_s	linear density	5.98 g/m
E_s	Young's modulus of elasticity	2E+11 N/m^2

Coupled equations of motion

In our model, considering flexibility in the backcheck wire and hammer shank, the obtained highly-optimized simulation code consisting of twelve ODEs can be written in state-space form as follows:

$$\dot{\hat{\boldsymbol{\Phi}}} = \boldsymbol{A}_{\boldsymbol{M}}\hat{\boldsymbol{\Phi}} + \boldsymbol{F}_{\boldsymbol{M}} \tag{4.16}$$

in which

$$\boldsymbol{A}_{\boldsymbol{M}} = \begin{bmatrix} \boldsymbol{0}_{12\times12} & \boldsymbol{I}_{12\times12} \\ \boldsymbol{0}_{12\times12} & \boldsymbol{0}_{12\times12} \end{bmatrix} \quad \text{and} \quad \boldsymbol{F}_{\boldsymbol{M}} = \begin{Bmatrix} \boldsymbol{0}_{12\times1} \\ \boldsymbol{M}^{-1}\boldsymbol{F} \end{Bmatrix} \tag{4.17}$$

$\hat{\boldsymbol{\Phi}} = \left\{\boldsymbol{q}^T \dot{\boldsymbol{q}}^T\right\}^T$ is the state vector of the generalized positions and velocities and $\boldsymbol{I}$ is the identity matrix.

Hammer-string interaction for the vertical piano action can be included by reformulating the method presented by Vyasarayani et al. [118] for the vertical action. The dynamic equations governing the behavior of the string, excited by the impulse force produced by the hammer, $f_n(t)$, and introducing the string lateral displacement as $x(y,t) = \boldsymbol{\phi}^T\boldsymbol{\eta}$ (equation 4.12), can be written in state-space form as follows:

$$\dot{\hat{\boldsymbol{\Psi}}} = \boldsymbol{A}_{\boldsymbol{S}}\hat{\boldsymbol{\Psi}} + \boldsymbol{F}_{\boldsymbol{S}} \tag{4.18}$$

in which $\boldsymbol{\phi}$ is the column matrix of string undamped mass-normalized mode shapes, $\boldsymbol{\eta}$ is the column matrix of string modal coordinates, $\hat{\boldsymbol{\Psi}} = \left\{\boldsymbol{\eta}^T \ \dot{\boldsymbol{\eta}}^T\right\}^T$,

$$\boldsymbol{A_s} = \begin{bmatrix} \boldsymbol{0}_{N\times N} & \boldsymbol{I}_{N\times N} \\ -\boldsymbol{R}_{N\times N} & -\boldsymbol{P}_{N\times N} \end{bmatrix} \quad \text{and} \quad \boldsymbol{F_s} = \begin{Bmatrix} \boldsymbol{0}_{N\times 1} \\ \boldsymbol{F}_{\text{norm}} \end{Bmatrix} \tag{4.19}$$

where

$$\begin{gathered} \boldsymbol{R} = \text{diag}(w_1^2,\ \ldots,\ w_N^2), \qquad\qquad \boldsymbol{P} = \text{diag}(2\xi_1 w_1,\ \ldots,\ 2\xi_N w_N), \\ \boldsymbol{F}_{\text{norm}} = \left\{\phi_1(y_c) f_n(t),\ \ldots,\ \phi_N(y_c) f_n(t)\right\}^T \end{gathered} \tag{4.20}$$

The two sets of ODEs — the symbolic equations derived for the action mechanism using the GTM method (equation 4.16) and those from the discretized string PDE (equation 4.18) — are coupled to form the overall dynamic equations for the whole system. The obtained equations, optimized in Maple for efficiency, are exported to MATLAB for numerical simulation. We use a stiff, variable-order, multi-step ODE solver, ode15s, which is based on the numerical differentiation formulas (NDFs). Absolute and relative tolerances of 10^{-6} were used in the simulations.

4.1.4 Mathematics-based contact mechanics

As shown in Figure 4.5, there are 16 contact locations in the vertical piano action, where the contact surfaces are lined with compressible materials such as felt or leather. Incorporating an accurate representation of contact in piano action models plays a key role in achieving high-fidelity simulations.

There are two major steps to predicting the dynamics of contact between interacting bodies in piano actions: contact detection and contact force calculation. A fully geometrical technique is applied to detect contacts, or the extent of penetration between colliding bodies. This calculation obviously depends only on the geometry, location, and (in some cases), the curvature of the contact interfaces. Estimating the force associated with the obtained penetration depth between the contacting bodies is a separate issue.

For the vertical action model, we utilize two geometry types applied in the grand piano action [35], line-circle and hybrid-circle, and introduce a third geometry type, line-concave

circle. These three geometries are used to represent all contact surfaces in the action. The hybrid surface is a geometry that consists of an arc segment and two lines extending infinitely from the tangents at the starting and ending points of the arc [35]. For a more realistic contact between the hammer butt check and the backcheck, three small circles have been placed in different positions on the butt check, as shown in Figure 4.5, to cover all the possible contact regions in their interaction. Note that the calculation of each contact force is independent of the geometry of contact surfaces—i.e., the geometry visualization is merely used to recognize contact occurrence, subsequently predicting the penetration depth between the corresponding bodies. A list of contact points in the action and their idealized geometry types are provided in Table 4.2.

Table 4.2: Geometrical description of the contact surface pairs in the vertical action

Contact No.	Contact description	Geometry type
1	Key-Ground at rest rail felt	Line-Circle
2	Key-Ground at front rail punching	Line-Circle
3	Key-Whippen at capstan	Circle-Line
4	Jack-Hammer at hammer butt leather	Hybrid-Circle
5	Jack-Ground at let-off button	Circle-Line
6	Hammer-String at strike point	Circle-Line
7	Hammer-Ground at hammer rest rail	Line-Circle
8	Hammer Butt-Backcheck (bottom point)	Circle-Concave circle
9	Damper-Whippen at damper spoon	Line-Circle
10	Damper-Ground at string	Circle-Line
11	Jack-Hammer at hammer butt cushion	Circle-Line
12	Jack-Ground at jack stop rail	Line-Circle
13	Hammer Butt-Backcheck (middle point)	Circle-Concave circle
14	Hammer Butt-Backcheck (top point)	Circle-Concave circle
15	Key-Ground at balance rail	Line-Circle
16	Damper-Ground at damper stop rail	Line-Circle

The modeling of felt compression-versus-force characteristics is a complex process due to the nonlinear hysteretic behavior of these complicated nonwoven networks under compression load schemes [1, 14, 23, 115]. There should be a theoretical framework to characterize the compression behavior of these materials as a function of fiber properties, structure architecture, and the fiber interactions, but it is also important to develop the relation in such a form that it can be updated in each step of a simulation in a reasonable amount of time. Therefore, a simplified approach was used for the contact model in order to keep the simulation time tractable. The experimental results for predicting the compressive behavior of a typical felt used in piano hammers is shown in Figure 3.14. The guillotine-like impact test in which a typical piano hammer strikes a rigid stop in free-fall experiments, performed at three different impact speeds, reveals the following properties of the dynamic

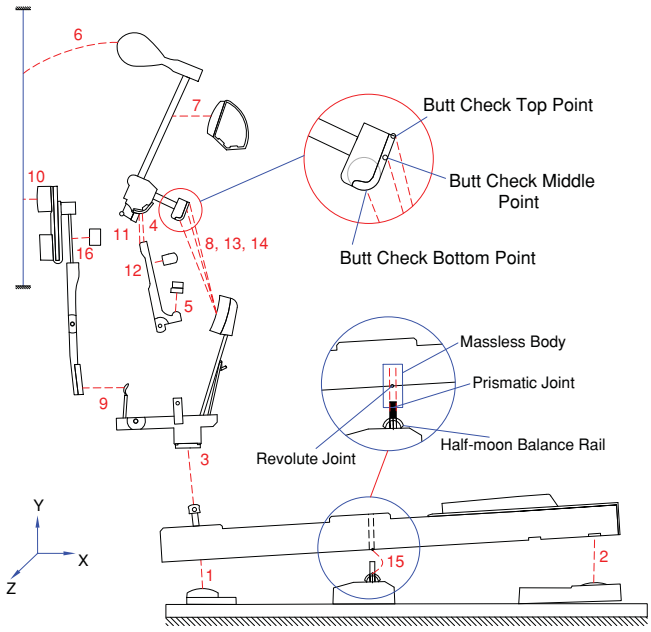

Figure 4.5: Contact locations in the vertical action mechanism.

compression behavior of piano felt:

1. The compliance of the loading and unloading curves is nonlinear.
2. There is a significant hysteretic loss in the fiber mass response when cyclic loading schemes are applied. This loss is attributed to both the friction of the interacting fiber as well as the difference in the structural parameters in loading and unloading stages [14, 23].
3. The loading curves are nearly velocity-independent, at least for these velocities, which are typical of the range applicable to the hammer-string interaction. This observation confirms the lack of viscoelastic behavior in felt.
4. Partial unloading curves depend on the uppermost loading compression level in each cycle.

Consequently, the major effort should be directed to constructing a mechanistic model, while still maintaining computational simplicity, to characterize the compression behavior of felt including all of the mentioned properties. Presently, we rely on an empirical

mathematical model to calculate the contact forces between interacting bodies in terms of the penetration depth at the interfaces, based on the experimental results obtained. The possibility of capturing all the dynamic properties of felt using a mechanistic approach has been discussed specifically in Section 3.3.2; in Section 4.1.5, the applicability of this procedure will be examined and compared with the mathematical model presented in this section.

A novel contact model with a unique set of parameters, independent from the inputs to the piano action, is introduced and precisely analyzed. This approach resolves the shortcomings associated with considering an input-dependent damping coefficient, which is the approach that has been used in previous work [36, 40, 118]. The proposed approach, originally introduced by Hirschkorn [36] for modeling a grand piano action, was developed based on an empirical mathematical curve that was fit to the average compression-recovery curve; hysteresis was incorporated into the model by assuming a viscoelastic relation and introducing a speed-dependent damping term. This approach is a compromise, since it is generally accepted that hysteresis in felt is related to dry friction and not viscous forces. This approach also generates highly velocity-dependent hysteresis, which does not reflect the recent experimental results presented in Figure 3.14.

These shortcomings are resolved in the present work by a novel approach that: (i) recognizes that partial unloading curves lie inside the hysteresis loop associated with the uppermost loading state achieved prior to unloading, and (ii) obtains a smooth transition between loading and unloading states that depends on the rate of unloading. Separate loading ($F_L(\varepsilon_p)$) and unloading ($F_U(\varepsilon_p)$) curve fits were calculated for force-compression data obtained from an experiment where the contact pair was loaded to a force in excess of the maximum anticipated in this application. The curve fits were calculated using the trust-region reflective algorithm [16] as implemented in MATLAB [67]. The most appropriate mathematical function to fit both loading and unloading data was found to be the following:

$$F(\varepsilon_p) = a\varepsilon_p e^{b\varepsilon_p} + c\varepsilon_p \tag{4.21}$$

in which $F(\varepsilon_p)$ is the contact force at the penetration depth ε_p between two interacting bodies, and a, b, and c are constant parameters. Contact force is defined to be zero for negative penetration depths (i.e., for non-colliding bodies). To model the hysteretic behavior and consider partial loading and unloading during interactions, the following mathematical relation is applied:

$$F_n(\varepsilon_p, \nu_n) = \begin{cases} F_L(\varepsilon_p), & \text{if } \nu_n \geq 0 \\ F_L(\varepsilon_p) + \delta_{LU}(\varepsilon_p)\tanh(\alpha\nu_n), & \text{if } \nu_n < 0 \end{cases} \tag{4.22}$$

where F_n is the normal contact force, ε_p is the penetration depth, $\delta_{LU}(\varepsilon_p) = F_L(\varepsilon_p) - F_U(\varepsilon_p)$ is the difference between the loading and unloading curve fits at each penetration depth, α is a constant that controls the transition speed between loading and unloading states, and ν_n is the normal speed between the two surfaces at the contact point, which also influences the transition. The relation defined in equation 4.22 confines the partial loading and unloading curves to lie within the experimental hysteresis loop used to obtain the curve fits— i.e., $F_U(\varepsilon_p) \leq F_n(\varepsilon_p) \leq F_L(\varepsilon_p)$.

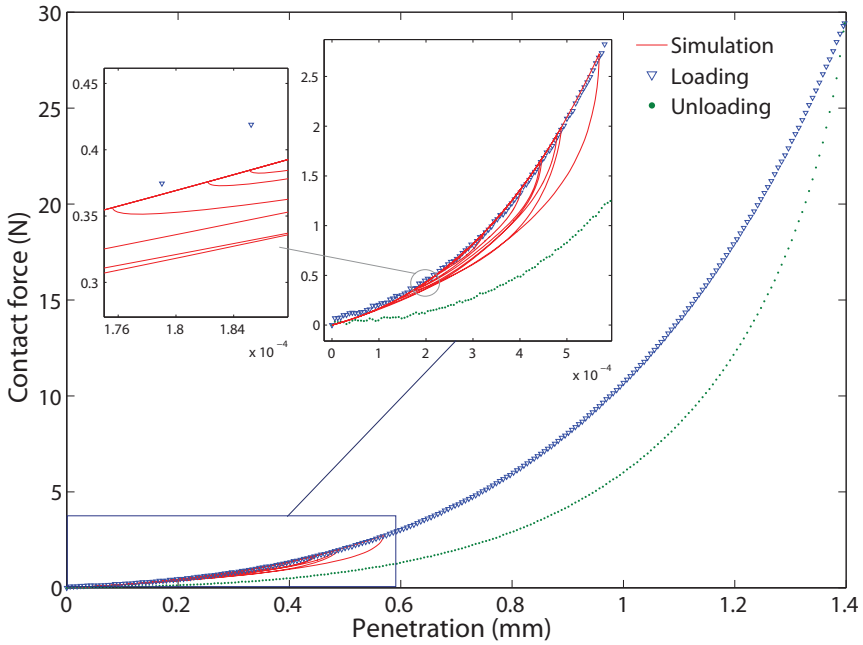

Figure 4.6: Experimental loading and unloading curves for a contact interface in the vertical action, and simulated hysteresis curves obtained using the technique described in Section 4.1.4.

Experimental results were obtained for each contact surface pair in the model, measuring force and compression in response to a cyclic loading scheme. The uppermost compression value for each contact was anticipated according to the preliminary simulation

results with approximate compression parameters. Force-compression data were collected using the Instron micro-testing machine in a quasi-static scheme with a compression rate limited to 0.1 mm/s. A typical result for the hysteretic contact force in the simulated model at the interface between the butt check and the backcheck is illustrated in Figure 4.6. As expected, the simulation results confirm the smooth transition between partial loading and unloading stages. The most promising characteristic of the proposed contact approach is that the simulated model is independent of the input force or motion on the key, which improves the main shortcoming of the model used by other researchers. To calculate the tangential friction on the contact interfaces, the common method of Coulomb friction modeling was utilized [18], as previously represented by [36].

4.1.5 Micromechanical-based contact mechanics

Applying the mathematical-based contact model in the dynamic model of the piano action ensures reasonable simulation results, at least as far as maintaining a minimum level of error in the modeling of contact between colliding bodies. The only drawback of the model is that it does not convey a mechanistic concept in calculating the contact forces as functions of the penetration depth between contact interfaces.

The micromechanical algorithm proposed in Section 3.3.2 is complicated but still of low computational cost; thus it is an encouraging contact approach in multibody simulations. Although it is a micromechanical procedure based on experiments, the pressure-compression relation is entirely evaluated according to a mechanistic approach. In particular, we consider the bending of the fiber at the microscale, along with fiber-to-fiber friction and structural parameters that differ in the loading and unloading stages. We still use the experimental data for each contact to determine (i) the uncertainty parameters in the micromechanical model with a binomial distribution of fiber contacts (K_p and γ in equation 3.64), representing the elastic portion of loading and unloading curves; and (ii) the structural parameters (θ_{crj} in equation 3.66) for estimating the friction contribution to generate nonlinear hysteresis in the contact model, referring to the algorithm introduced in Section 3.3.2. However, when we incorporate the contact model into the dynamic simulations, it is only based on mathematical curves carrying physical concepts, along with the hysteresis prediction formed on a fiber-to-fiber basis.

In the first phase of the contact model (contact detection), the penetration depth is calculated; in the second phase, the obtained force is linked to the multibody dynamics of the action mechanism. Accordingly, the pressure acquired from the described contact models requires information on the equivalent common contact area to predict the amplitude of the normal force on the interfaces. For simple contact geometries, estimating the

area in terms of penetration depth is straightforward, but when interacting surfaces with complex curvatures rotate and displace during contact, a more sophisticated technique is needed. Due to restrictions in performing the experiments on different types of felt used in the vertical piano action, collecting the required data in the micromechanical contact model for all 16 contact points was not possible; this task remains for future work. Instead, contact information for one of the most important contact locations, the hammer-string interaction, has been provided and is used to evaluate the proposed model. Computing the common contact area is not complicated in this case, and is evaluated theoretically. As will be demonstrated by the simulation results, the only notable difference when applying these two contact models is in the simulation time, since both models were constructed based on the same experimental data, but applying different approaches — one mathematical and one micromechanical.

4.2 Experimental regulation and numerical simulation

The equations of motion obtained for the action are in fully symbolic form. Numerical simulation for a specific vertical action mechanism, including hammer-string interaction, requires estimating the physical parameters defined in developing the dynamic model, and providing the inputs and initial conditions required to solve the ordinary differential equations. To this end, the Steinway Model 45 action was selected and instrumented as the specific physical prototype. Standard experimental procedures were then employed to measure the physical parameters for the action mechanism. Predicting initial conditions, measuring input force profiles, and estimating physical parameters of the vertical piano action mechanism are discussed thoroughly in the following sections. An inventory of string parameters for the Steinway upright piano (Steinway & Sons 45), note 40, is provided in Table 4.1.

Experimental data for the vertical piano action prototype were collected and processed by Professor Stephen Birkett, at the piano design laboratory of the University of Waterloo, with whom we collaborated. The experiments include estimating relative motion of the tracking points on the action components using high-speed video cameras, performing compression or tension tests on the flexible components, springs, and contact surfaces, measuring the input forces to the action, taking still photos from the action, and regulating the physical prototype action. The geometrical information from the action components, along with the kinematic data, was used by the author to extract displacement and speed of specific points for comparison against the simulation results. All the high-level processing of

the experimental data including measuring mass properties of the components, estimating structural properties and vibrations of the flexible components and springs, and extracting the contact parameters were completed by the author.

4.2.1 Force profiles

The inputs for simulations consist of force or motion profiles applied at the key front. In fact, the inputs to the piano action should resemble the finger force or motion of a pianist striking a real vertical piano action key. These force or motion inputs must be precisely repeatable to enable a methodological study of the dynamic behavior of the action in multiple trials. Hence, a mechanical actuator along with a control unit is used in the experiments with a physical prototype, assuming that it generates a force profile fairly similar to that generated by real pianist finger.

Two typical force profiles, a 'forte pressed' blow (forceful, but not abusive) and a 'piano pressed' blow (soft and gentle) are generated and examined in this thesis. The simulation force profile inputs, consisting of oscillating ramps and held forces, are shown in Figure 4.7. The time scale has been translated so the moment the contact force between the hammer and string is at a maximum corresponds to time zero. These forces have been obtained from a force sensor attached on the key front between the finger actuator mechanism and its point of application on the key surface. The slope of the force profile determines the strength of the hammer striking the string, as defined by the impact speed; steeper slopes result in more rapid hammer accelerations. As can be seen, the initial impact in the forte blow can be expected to be faster than that of the piano blow.

4.2.2 Component parameters

To parameterize the obtained symbolic equations, the geometric and mass properties of the piano action components, along with ground point locations, should be measured. All bodies from the disassembled prototype action were scanned using a flat bed scanner. The obtained images were then imported into a CAD software package and scaled to match known reference dimensions of each part. The boundaries of each body were traced precisely, and the dimensions were derived from the obtained drawings. High-resolution images were taken (from different angles) of the action prototype base frame, to which the mechanism components are attached, and a similar procedure was utilized to find the global and relative coordinates of the ground points and pivots.

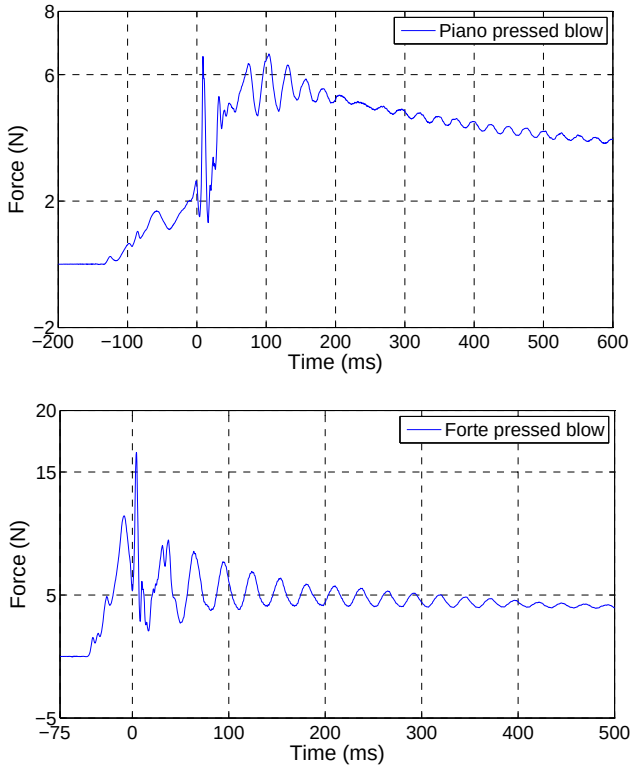

Figure 4.7: Piano pressed (top) and forte pressed (bottom) key stroke force profiles (model inputs).

Masses were measured using a lab scale, and the mass moment of inertia of each body was estimated by measuring the frequency of free oscillations about a specific point of the body. To include the flexibility of the backcheck wire and hammer shank, mass properties of the exploded whippen and hammer assembly were required. The CAD drawings of the hammer and whippen were used to construct a 3D SOLIDWORKS [99] model, from which the location of the center of mass and the mass moment of inertia of the disassembled parts were derived, assuming homogeneous material properties. The 3D model was also beneficial for monitoring the regulation of the action and validating the mass properties of each body. Numerical values of the action parameters including mass and structural parameters of the action components (bodies, bridle strap, and torsional springs), contact interfaces and joints parameters, modeling points considered on each body of the action, and global location of ground points are listed in Appendix A.

4.2.3 Experimental regulation of the action

Regulation is the process of making (small) adjustments to the piano action in order to maintain the proper feel and response, as well as a desired sequence of events during the key stroke. To function correctly, a piano action requires tolerances that cannot be maintained indefinitely, due to (i) material expansion and contraction caused by ambient conditions, (ii) creep compression, and (iii) wear in the felts. These changes are compensated for by a design with several adjustable components. For example, the capstan can be screwed in or out to adjust its height on the key, washers can be placed under the key front to adjust the overall key motion possible (key dip), and the backcheck wire can be bent to change its position with respect to the hammer butt. Regulation is a static or pseudo-static procedure.

In parameterizing the action model, it is not possible to explicitly measure component geometries with sufficient accuracy to satisfy a particular known prototype mechanism regulation in the simulated action. This situation applies, in particular, to the initial conditions, which are determined in a real action by the static configuration of the components under gravity as the felts in the interfaces compress with the action at rest. The regulation process adjusts parameters so that each component in the action mechanism precisely performs a desired task at the right time with respect to the other components. Virtual regulation steps were used to adjust parameters in the simulation model following the same sequence used in a real action, ensuring that the correct functionality was achieved at each stage. After each parameter adjustment made in the model, a new set of initial conditions was obtained by simulation by allowing the components to fall under gravity and reach equilibrium.

The regulation process in the vertical piano action is described briefly below, taken almost verbatim from the Steinway World-Wide Technical Reference Guide [102]. The letters in Figure 4.8 show the adjustment locations in the action.

A. KEY DIP: The distance from the underside of the key front at rest to the top of the front rail punching is 10.5 mm. Paper washers are used underneath the front rail punching to adjust it. In the model, the ground contact surface is moved.

B. HAMMER BLOW: The horizontal distance from the hammer contact surface to the string is 48 mm. This distance is adjusted by screwing the capstan up or down in the key. In the model, the capstan contact surface is moved.

C. BACKCHECK. After the hammer has struck the string under a moderate key blow, the hammer rebounds and is captured by the backcheck at 15 mm from the string.

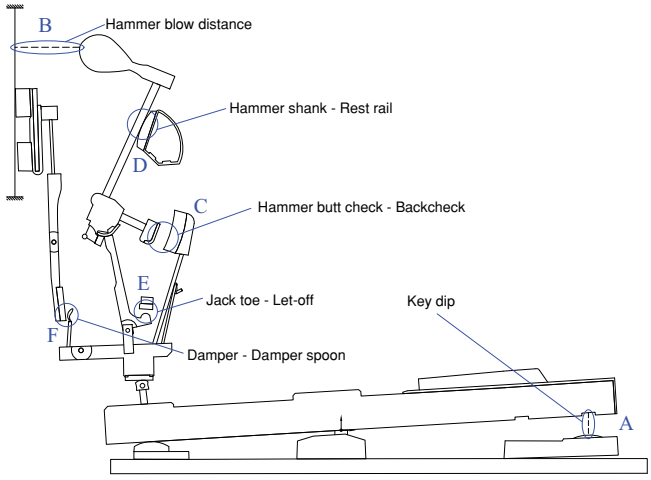

Figure 4.8: Regulation points for the vertical piano action.

The backcheck is adjusted by bending the backcheck wire. In the model, the location of the backcheck contact surface is moved, or its angle is changed, until the desired check position with respect to the string is attained.

D. HAMMER REST RAIL: The hammer shank should touch the rest rail felt with minimal contact. Therefore, the hammer shank should follow the hammer rail very slightly if the hammer rail is gently pulled away from the shanks. In the model, the location of the hammer shank ground contact surface is moved. The lost motion, which is the space between the hammer butt and the jack, should be about 1 mm when the hammer shank is initially supported by the hammer rest rail.

E. LET-OFF: This action should occur when the hammer contact surface is 2 mm away from the string; The distance is adjusted using the let-off regulating screw. In the model, the ground contact surface for the jack toe is adjusted.

F. DAMPER: The damper lever should begin to move when the hammer is approximately half the distance to the string. This distance is adjusted by bending the damper spoon located on the back end of the whippen. In the model, the appropriate contact surface on the damper is moved.

According to the experiments accomplished on the vertical action prototype, a very precise regulating of the action is required to keep the simulation results reasonably and accurately comparable to the experimental ones. The sensitivity of the action response

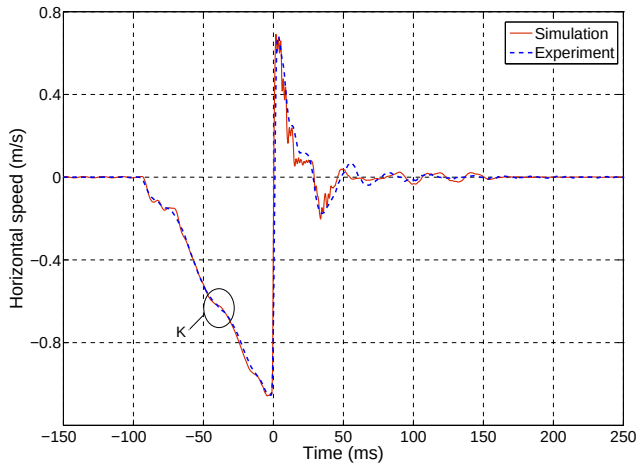

Figure 4.9: Simulated and experimental horizontal speed of hammer tip for the piano pressed input.

differs in each regulating step with respect to the specific parameter adjustments. For instance, changing the position of the jack let-off about 0.1 mm results in a significant shift in the hammer-string impact speed and, subsequently, the rest position and impact initiation time of the hammer butt check on the backcheck. In other words, a slightly inaccurate timing of different events during the key stroke can influence the overall response of the action considerably. In the following, the particular stages required to verify the precision of the regulation are discussed.

One of the most reliable criteria to assess the accuracy of the regulation process is to monitor the speed of a typical point on the hammer and compare it with the simulated speed. Figures 4.9 and 4.10 indicate the speed in the horizontal direction versus time for a tracking point on the hammer tip in the case of piano and forte blows, respectively. Excellent agreement with experimental results indicates that the let-off timing in the simulation is accurate for both input forces applied on the key. This agreement can be achieved by:

I. Ensuring accurate before-impact and after-impact speeds of the hammer-string interaction by adjusting the position of the let-off regulating rail and the string structural damping parameters, respectively. In fact, the pick values in the speed profiles, specifying pre-impact and post-impact hammer speeds, play a key role in the overall dynamic behavior of the action. According to the simulation results, the impact speeds for piano and forte blows were 1.06 m/s and 3.36 m/s, with respective relative errors 0.34% and 5.64% with respect to experiments. Simulated post-impact speeds

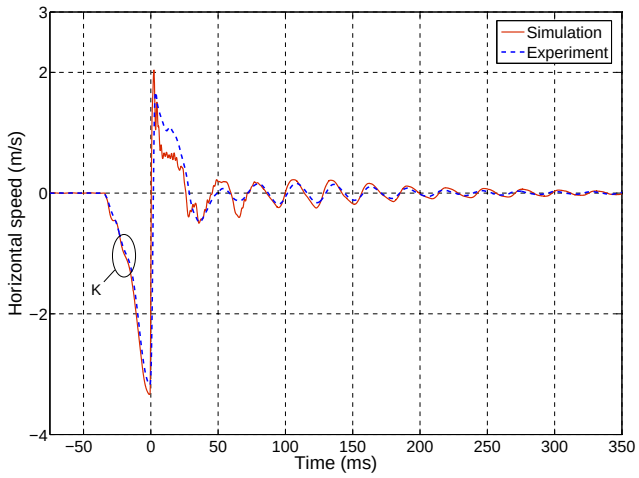

Figure 4.10: Simulated and experimental horizontal speed of hammer tip for the forte pressed input.

for piano and forte inputs of 0.69 m/s and 2.04 m/s give relative errors of 1.4% and 21%, respectively.

II. Following the explicit slope changes in the speed profiles, which are due to changes in the angular speed of the whippen. This action occurs exactly when the damper spoon hits the damper and causes it to start rotating counterclockwise, away from the string. For the piano below, it occurs at time $t = 0.219$ s; for the forte blow, $t = 0.088$ s. These times are indicated by point K in Figures 4.9 and 4.10, which confirm good agreements in timing between simulation and experiments.

III. Verifying the correct distance between the hammer and string at the moment that contact force 4 (Jack-Hammer at Hammer Butt Leather, referring to Table 4.2 and Figure 4.5) approaches zero. Its simulated value of 2.2 mm in the final regulated model is in close agreement with regulation stage E of the real action. This agreement can be achieved by moving the let-off regulating rail slightly, which also significantly affects the speed of the first impact between the hammer and string, as well as the capstan height on the key.

It is to be noted that regulation and precise timing require a balance between all the adjustment parameters in the action mechanism.

4.2.4 Analysis of simulation results and experimental validation

Simulation results for the comprehensive vertical action model, developed and regulated in the theoretical sections of this chapter, are extensively analyzed and experimentally validated in this following section. Capability in collecting the required experimental information for all 16 contact points in the prototype model has enabled us to apply the novel mathematical-based contact model as the primary contact approach in the simulations. Moreover, this approach is much faster than the other detailed contact model (as discussed in Section 4.1.5).

The applicability of the micromechanical-based model in the multibody simulation of the action is analyzed in Section 4.2.5, confirming the strength and stability of the proposed contact model in creating a fully mechanistic model. The experimental data for hammer felt are sufficient to derive the parameters of the micromechanical contact model for hammer-string interaction. Extension of the model to the remaining 15 contact points requires experimental data for all the different types of felt used in the vertical action, which is left as future work. It will be demonstrated that the obtained results, except for the simulation time, do not change significantly; thus, the model can be used in any multibody model simulations with similar interactions between contacting bodies.

Flexibility of the hammer shank and backcheck wire were included in the simulation of the multibody dynamic model. The obtained simulation results are compared with those obtained when the bodies are rigid to assess the necessity of adding flexibility to those components. In addition, the hammer-string interaction, the new contact model, and key lift-off are further complications that are considered in the action to achieve a high fidelity simulation model. The significance of applying the stiff compliant string instead of a rigid stop will be discussed and evaluated. The new contact model provides the capability to apply unified contact parameters for different inputs to the action model, which modifies the input-dependent contact model used in previous work on grand piano action models. Utilizing the massless body in conjunction with a prismatic joint to estimate the lift-off motion of the key makes the simulated model behave in a more accurate fashion when compared to experiments.

In the experiments, instead of measuring angular rotations, as was done in [35, 40], tracking designated marked points on different locations of the action components is preferred. In fact, tracking different points on each body using a high-speed camera enables us to incorporate all the possible motions, such as the compliance or vibrations of components, in the obtained results. Accordingly, the vibrations due to component flexibility can be estimated by monitoring different tracking points on the action parts. A schematic of the real prototype action along with all tracking points marked on the real action components

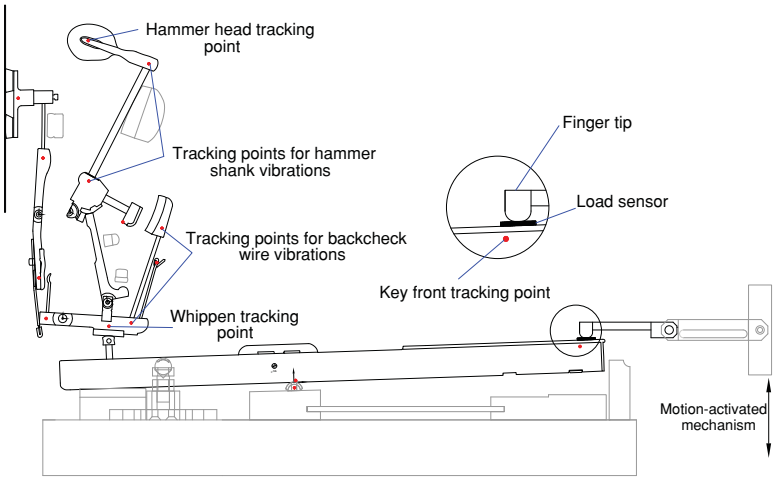

Figure 4.11: Tracking points on the constituent components of the piano action.

at desired local coordinates is illustrated in Figure 4.11. The prototype model has all five main bodies used in the simulated action, but comparisons are only made for the motion of the key, whippen, and hammer, since they are more operative during the key stroke and the experimental results for these three bodies are more reliable.

High-speed video cameras are used to obtain accurate measurements of the displacements and speeds of designated tracking points on different bodies of the real action. A Photron Fastcam-X 1280 camera was used by Professor Stephen Birkett to capture digital videos from the fast moving components of the piano action at some desired resolution [35], depending on the frame speed at which the experiments were performed. Technologically, resolutions up to 1280×1024 pixels and speeds up to 16,000 frames per second are achievable by this particular camera. In general, capturing high-speed videos at higher resolution requires lower recording rates. The camera software, capable of recording position of the specific tracking points in the videos, provides information corresponding to the relative motion of any desired point on the action components based on its position in each frame. In this research work, a resolution of 1280×1024 pixels was achieved at a speed of 2,000 frames per second, and displacements of the marked points were measured with respect to the original positions at rest. The force sampling occurred at the same rate used by the camera.

Piano-pressed input

The piano blow, which represents a very soft note in a piece of music, is applied to the key surface on the force sensor using the actuator mechanism, as shown in Figure 4.11. A prescribed motion of the actuator arm base will produce the desired force on the key. The force data read by the load sensor on the key front is utilized as the input to the action model. The simulation results for the displacement of the tracking point on the key front in the Y direction, Δ_Y^{kf}, is shown in Figure 4.12 and compared with the corresponding experimental data. The acquired force is plotted in the same graph to simultaneously inspect the coincidence of particular events in the action.

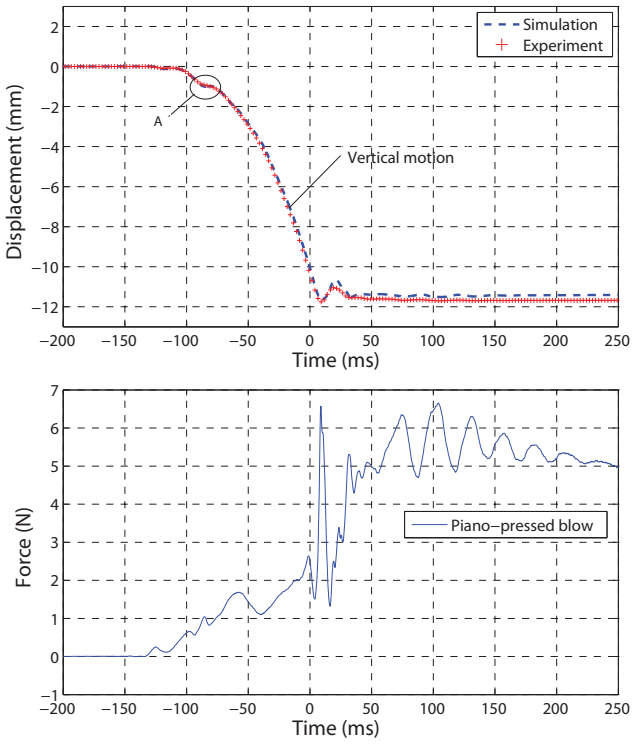

Figure 4.12: Vertical displacement of the key front tracking point, Δ_Y^{kf} (top), and piano-pressed force profile (bottom).

When the pianist presses the key, it does not start to move immediately due to the weight on the capstan as well as joint friction, especially in the key pivot. The obtained simulation results, in comparison to experiments, confirm that the correct friction values were used for the joints. Overcoming the joint friction and weights, the key starts to rotate

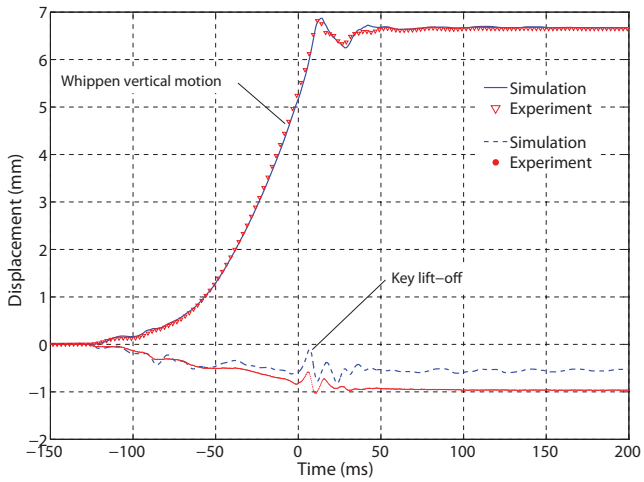

Figure 4.13: Vertical displacements of the whippen tracking point, Δ_Y^{wh}, and key lift-off, $4\Delta_Y^{kb}$, for piano-pressed blow.

clockwise about the balance rail pin and causes the capstan located at the end of the key to move upward. There is a considerable change in the tangent line to the displacement profile at point A in Figure 4.12, which is as a result of the lost motion between the jack and hammer butt, where the jack moves on the side wall of the butt without pushing the hammer. The vertical motion of the capstan on the key back makes the whippen rotate counterclockwise about its ground-fixed pin. The correct timing of whippen rotation has a significant effect on the proper performance of the jack and the moment that jack let-off occurs in the action model. Displacement of the whippen tracking point in the Y-direction, Δ_Y^{wh}, is shown in Figure 4.13. The vertical motion of the tracking point on the key, adjacent to the balance pin, is also plotted in the figure, and represents the key lift-off prismatic joint variable in the model. It should be noted that the plotted profiles are $4\Delta_Y^{kb}$ to magnify the tiny magnitude of key lift-off and distinguish more details. Although it does not fit the experiments perfectly, the simulation follows the experimental results in a promising manner. The error, at its largest value, is about 0.15 mm, which is negligible and does not have a significant effect on the simulation results. The source of minor disagreement is probably due to inconsistent model considerations and parameters that are utilized in modeling the atypical joint at the key balance rail.

X- and Y-displacements of the tracking point on the hammer tip, Δ_X^{htip} and Δ_Y^{htip}, are shown in Figure 4.14. A great agreement between the simulation and experiment can be observed, which verifies the precise regulation and accurate simulation model of

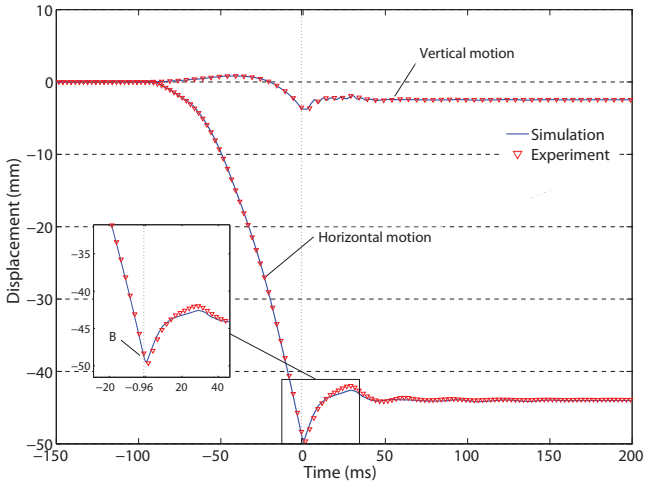

Figure 4.14: Horizontal, Δ_X^{htip}, and vertical, Δ_Y^{htip}, displacements of the hammer tracking point for piano-pressed blow.

the action. In order to have an accurate stop position of the hammer on the backcheck, the simulation should follow the experimental trajectory profile in an extremely precise manner. Figure 4.14 signifies that the simulation performs very well, especially before hammer-string impact at point B ($t \simeq 0$). The magnitude of impact speed, which depends on the dynamic response of the hammer before impact, plays a very important role in the dynamic behavior of the hammer in the post-impact stage. Generally speaking, there are four main factors to achieving a consistent hammer stop position on the backcheck:

1. Hammer-string post-impact speed.
2. Precise description of contact between the hammer and backcheck.
3. Flexibility of the backcheck wire.
4. Amount and type of friction between the hammer and backcheck

As shown in Figure 4.14, the hammer-string interaction causes the hammer to bounce back on the backcheck and undergo low-frequency oscillations before it rests completely on the backcheck.

Forte-pressed input

To validate the capability of the action model in representing a comprehensive theoretical model, it should be consistent in responding to various inputs. To this end, a completely different force profile is applied to the action and the simulation results are compared with a corresponding experiment. The application of a different force profile to the same model proves that introducing our new contact model has resolved the problem of input-dependent parameters used in previous research. The forte blow, which is more acute and much stronger, is a proper candidate to apply on the key front. The vertical displacement of the key front tracking point, Δ_Y^{kf}, and the force profile are shown in Figure 4.15. A

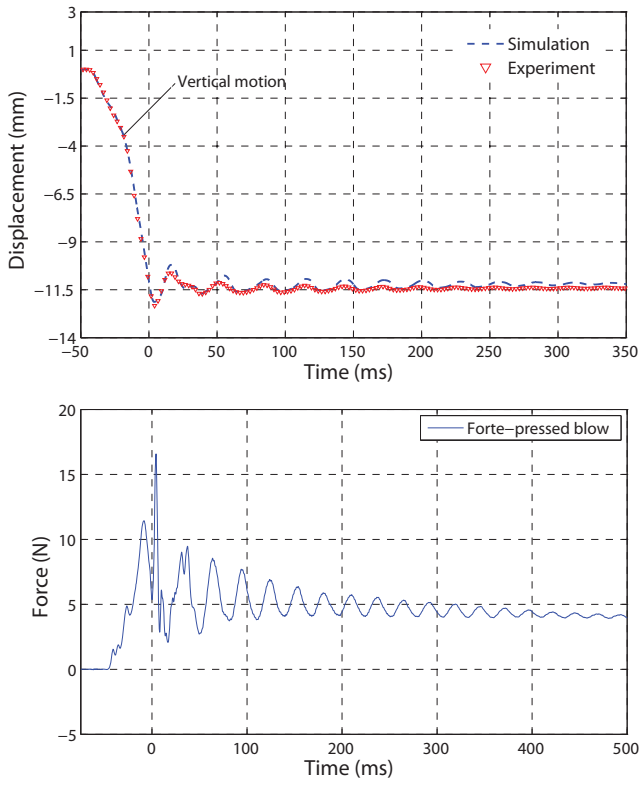

Figure 4.15: Vertical displacement of the key front tracking point, Δ_Y^{kf} (top), and forte-pressed force profile (bottom).

good agreement between simulation and experiment was recognized for the key motion profile. The only noticeable difference is the amplitude of oscillation after impact between the key front and its balance rail, which is due to the large impact force produced by

the hammer-string interaction for this particular force input. Simplifications considered in modeling the components may be also responsible for the dissimilarity. In comparison to the piano-pressed results, the key travels a larger distance due to more compression in the front rail felt.

The hammer horizontal and vertical motion, whippen vertical motion, and key lift-off in response to the forte input are shown in Figure 4.16. It is interesting to note that the simulation profiles follow the experiments very well before hammer-string contact occurs. This figure confirms that accurate values were measured for the mass properties, joint frictions, and spring constants, and a well-regulated mechanism was used in the simulation. The main sources of error (e.g., oscillations after hammer-backcheck impact) originate from the large post-impact force in the hammer-string contact, the degree of flexibility considered, the contact model and, on the top of all this, involving all components and their contact interfaces in the reaction to hammer-backcheck interaction. The main difference between upright and grand piano actions is that all the components, except the jack, will be involved in stopping the hammer after it bounces back from the string impact. Thus, all the modeling shortcomings will accumulate in the final stop position of the action. This phenomenon can be observed in the time history of the hammer displacement in the X- and Y-direction, as shown in Figure 4.16.

The validation results obtained for the simulated model affirm the capability of the simulation model to respond to various inputs applied to the action mechanism. Furthermore, using a single set of contact parameters for both inputs proved the reliability of the model regardless of the input. However, acquiring a very precise stop position of the hammer on the backcheck may require some parameter adjustments at this contact point due to the complex interaction between hammer and backcheck. The most important and delicate point about the piano action simulation is the way that the input has been applied. In this thesis, a load sensor has been attached to the key front surface, where the actuator touches the key, and the measured force was used as input to the mechanism. If there occurs a very small shift in the timing of the response for any of the action components, it will produce a reaction force on the key which is not the same as that observed experimentally. In fact, this temporal shift can be considered the main source of error between the simulation and experimental results. Applying a motion profile, generated by the actuator mechanism, as the input to the action model will likely result in a more realistic response.

Including additional complexity in modeling the action components requires considerable effort and computational expense. Consequently, it is worthwhile to investigate the effect of ignoring complex effects on the response of the action model. In the following sections, the impact of ignoring flexibility in the hammer shank and backcheck wire, as well as the compliance of the string will be studied by observing the hammer dynamic

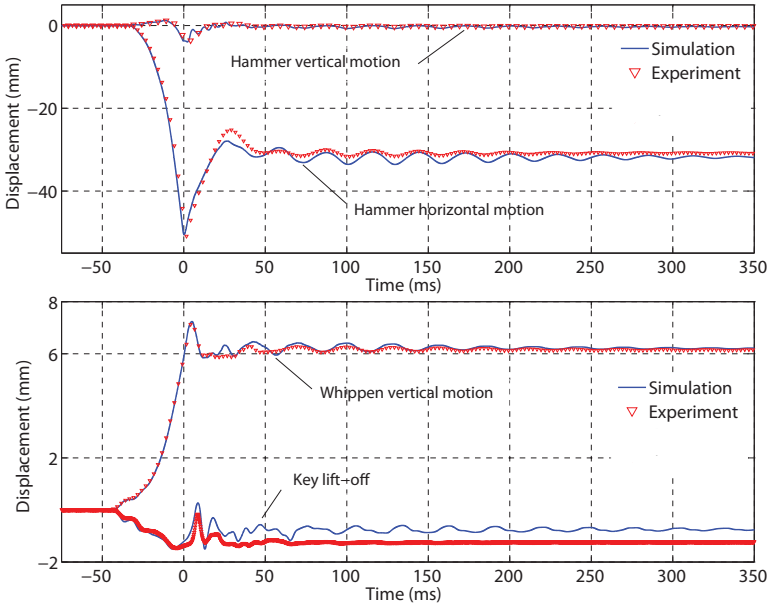

Figure 4.16: Time history of tracking point displacements of the hammer (Δ_X^{htip} and Δ_Y^{htip}), whippen (Δ_Y^{wh}), and key lift-off ($4\Delta_Y^{kb}$) for forte-pressed blow.

behavior.

Backcheck wire and hammer shank flexibility

Monitoring the motion of the hammer and backcheck using high-speed videos revealed that there are visually significant vibrations in both the backcheck wire and the hammer shank during the experiments.

I. Flexible vs. rigid backcheck wire

Substituting the flexible backcheck wire with a rigid component reduces the computation time, but influences the dynamic behavior of the action model to a great extent. In Figure 4.17, simulation results for the hammer motion using flexible and rigid backcheck wires are demonstrated by applying the piano and forte force profiles. The rest position of the hammer on the backcheck has been altered for both blows. Specifically, the stronger blow loses its energy considerably faster than the piano blow due to friction between the

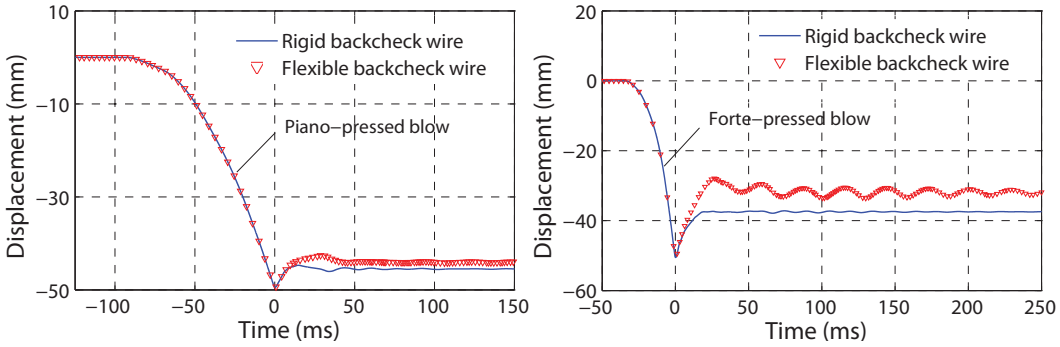

Figure 4.17: Simulation results for horizontal displacement of hammer tracking point using flexible and rigid backcheck wires.

interacting bodies and a lack of compliance in the wire, so the hammer stops closer to the string. The backward motion of the hammer toward the string after striking the backcheck is not observed in the simulation results without flexibility. This result means that the absence of wire flexibility can even influence the quality of sound in repeated notes, as the hammer is closer to the string before the second note is played.

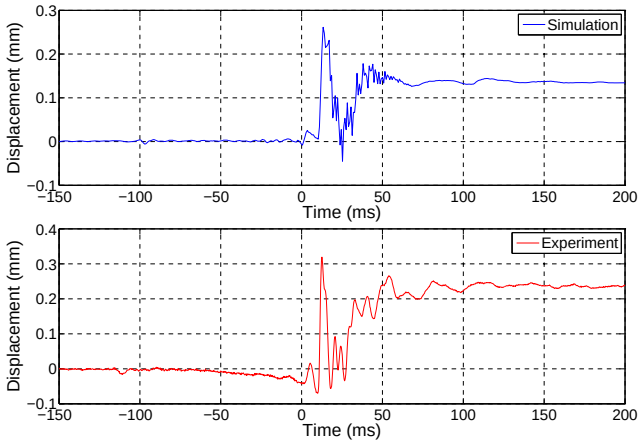

Figure 4.18: Time history of horizontal vibrations of a tracking point on the backcheck for the piano blow.

Tracking a point on the backcheck (where it is attached to the backcheck wire) with respect to another point on the whippen (where the backcheck wire is attached) provides the information required to study vibrations of the flexible body. Simulated and experimental

vibrations obtained from tracking the designated points on the backcheck and whippen (see Figure 4.11) in the horizontal direction are shown in Figure 4.18 for the piano blow force. They were not plotted in the same set of axes due to the high data density so that they can be recognizable and compared. A reasonable agreement can be observed between the simulation and experiment, which validates the model assumptions and estimated parameters of the flexible component. The major source of error in this case is the clearance in the revolute joint between the whippen and ground. This error can be recognized by tracking the motion of an arbitrary point on the whippen. The trajectory of such a point about the whippen pivot deviates from a circular path, which confirms the existence of the clearance. Furthermore, the simplification assumptions considered in modeling the friction and contact between the hammer and the backcheck can have a significant effect on the dissimilarity at the end of simulation. The oscillation for the forte blow is similar, but with a greater degree of oscillation; the plots have been omitted for the purpose of brevity.

II. Flexible vs. rigid hammer shank

The dynamic behavior of the hammer strictly influences the quality of the sound produced due to hammer-string interaction, as well as the feel of the action. A more precise hammer model can be achieved by including the shank flexibility, but there should be a balance between the computation cost and adding more realistic features to the model. Hence, it is worthwhile to compare the hammer motion using flexible and rigid hammer shanks. Figure 4.19 shows a comparison of the hammer horizontal motion for flexible and rigid hammer shanks for piano and forte blow forces. There is no significant difference between

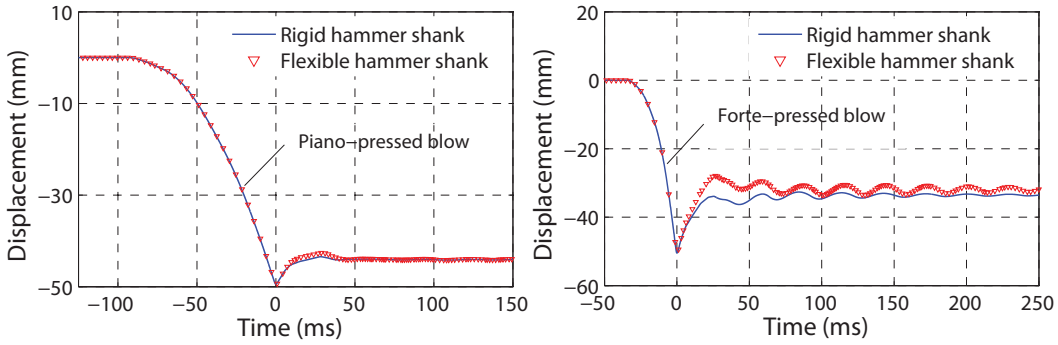

Figure 4.19: Simulation results for horizontal displacement of hammer tracking point using flexible and rigid hammer shanks.

the hammer displacement profiles the for piano input, but in case of the forte blow, the hammer shank model affects both the stop position and the amplitude of oscillations. As demonstrated in Figure 4.20, the inconsistency can be due to noticeable vibrations in the hammer head for the forte blow.

Comparing Figures 4.17 and 4.19 shows that the effect of hammer shank flexibility on the dynamic behavior of the action is much less than that of the backcheck wire flexibility.

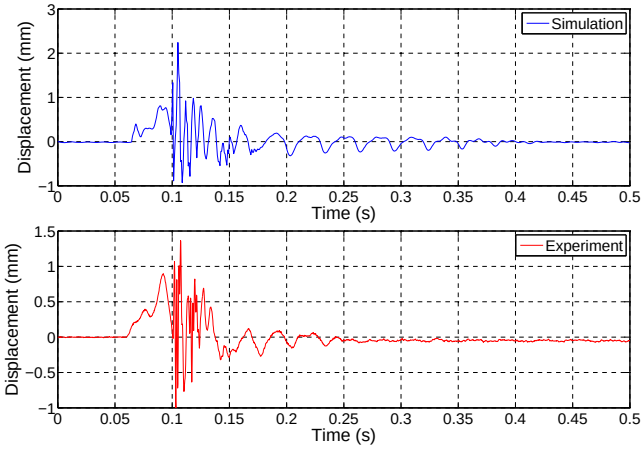

Figure 4.20: Time history of horizontal vibrations of a tracking point on the hammer head for the forte blow.

Hammer-string interaction vs. rigid stop

Hammer-string interaction has been a challenging issue in building more realistic piano action models. By including a stiff string model, the governing equations of motion will be much more complicated and computationally expensive. While some previous investigations only focus on using a rigid stop [35, 36, 40, 41], this section utilizes the idea presented by Vyasarayani [118] to demonstrate the importance of applying a compliant string instead of a rigid stop. Figure 4.21 shows simulation results for the hammer motion using hammer-rigid stop and hammer-string interactions for the piano and forte input forces. Monitoring contact 6 (hammer-string) reveals that the impact force produced by the rigid stop is much higher than that produced with the string, as listed in Table 4.3. The rigid stop causes the hammer to rebound from its ground point with greater speed. For both force inputs, the stop position of the hammer on the backcheck is further from the string when using the rigid stop, which is due to the higher impact force in the hammer-rigid stop interaction.

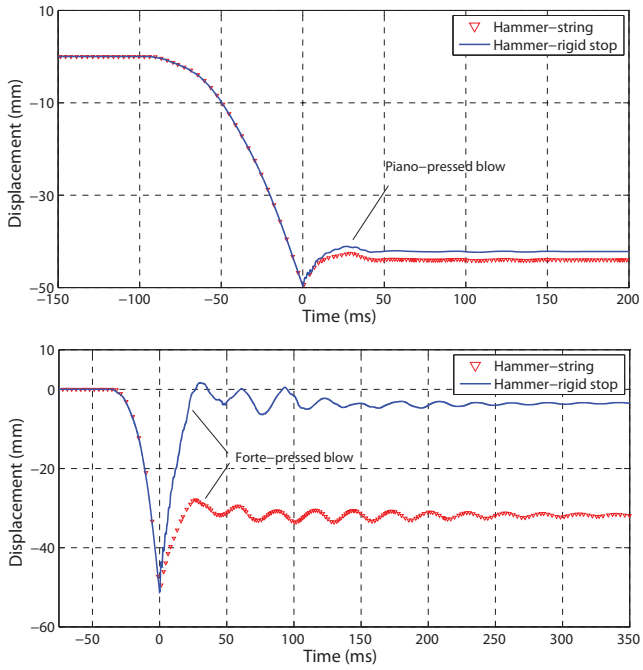

Figure 4.21: Horizontal displacement of the hammer tracking point for forte (bottom) and piano (top) blows using rigid stop and string ground point in hammer-string contact.

These results also indicate the necessity of precise event timing in the action model. In the case of the forte blow, the situation becomes worse than the piano blow and it seems that the hammer does not even contact the backcheck and rests around its initial position on the rest rail. In other words, the backcheck should be in a wrong position when the contact occurs. Monitoring contact forces 8, 13, and 14 (hammer butt-backcheck) reveals that there is another justification: the force at the first contact between the hammer and backcheck is large enough to overcome the reaction force on the capstan, and causes the key to rotate counterclockwise. This force carries the whole action nearly back to its initial state, then the hammer rebounds to lie on the backcheck again in another position which is far away from the string, as shown in Figure 4.21. The obtained results demonstrate the extreme importance of applying the compliant string model, ensuring precise timing, and demanding accurate regulation in the action model to have reasonable dynamic responses.

Table 4.3: Comparison of hammer-string and hammer-rigid stop responses

Blow force	Max impact force (string contact) (N)	Max impact force (rigid stop contact) (N)	Contact duration (string contact) (ms)
Forte-pressed	39.31	364.90	2.3
Piano-pressed	11.56	25.88	2.8

Effect of the hysteretic contact model

To examine the importance of including hysteresis in the proposed contact model, a lower-fidelity contact approach in which there is no hysteresis loss in the compression behavior of felt is considered. To achieve this, the average of loading and unloading data is assumed to represent the nonlinear compliance of felt in compression. The hysteresis-free contact model is applied to all the interacting bodies with "line-circle" contact (refer to Table 4.2) in the multibody dynamic model of the vertical piano action. Simulation results, applying the hysteretic micromechanical approach and the lower-fidelity contact model, are demonstrated in Figures 4.22 and 4.23 for the two different inputs to the action.

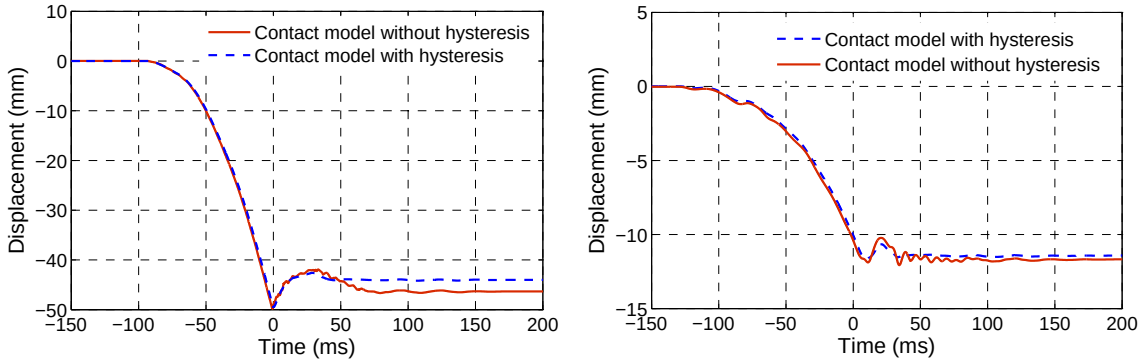

Figure 4.22: Comparison between simulation results for key vertical motion (right) and hammer horizontal motion (left), applying hysteretic and non-hysteretic contact models in case of piano input blow.

It can be concluded that it is very important to implement a precise contact concept in the dynamic model of the piano action. Higher oscillation peaks, especially in the vertical motion of the key, when applying the lower-fidelity contact model, reflect lower damping effect and stiffer response of felt compression in unloading stage due to lack of hysteresis

in the contact model. This significantly affects the stop position of the hammer on the backcheck in both piano and forte input blows.

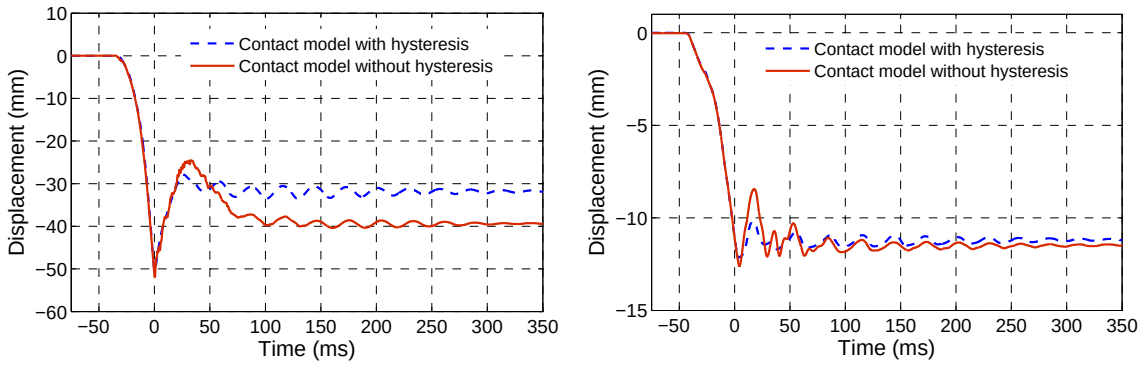

Figure 4.23: Comparison between simulation results for key vertical motion (right) and hammer horizontal motion (left), applying hysteretic and non-hysteretic contact models in case of forte input blow.

Bridle strap and butt spring

Butt springs and bridle straps in vertical piano actions play vital roles in the dynamic behavior of the action, especially for detached blows like repeated notes or staccato, unconnected notes. These two components help the hammer bounce back from the string to its still position on the rest rail. When the key is released after a stroke, the whippen falls back to rest on the capstan screw and the hammer tilts backward around its center pin to its rest position. The whippen falls straight down while the hammer rotates backwards. The butt spring alone is not nearly strong enough to accelerate the hammer back. Moreover, the torque generated from the weight of the hammer about its pivot is not sufficiently strong to help the hammer rebound when some specific blow forces are applied on the key. This means that the whippen is much faster than the hammer at returning to its rest position. The function of the bridle strap (if adjusted properly) is to jerk the hammer back when the whippen falls, ensuring that the hammer will return to its rest position quickly. The bridle strap also prevents the hammer from hitting the string if a key is only partially pressed. Keys get partially pressed quite often when a piano is played manually because of thick or misplaced fingers not fitting exactly on the correct keys all the time. To investigate the importance of including these two components, a typical staccato force profile was applied on the key and the motion of a tracking point on the hammer tip was

monitored. The force profile measured by the load sensor represents a physical pulse of 25 ms duration, as shown in Figure 4.24. Simulation results for the hammer motion with active and inactive butt spring and bridle strap components are also shown in Figure 4.24. As expected, the post-impact rebound time for the hammer increases by removing either the butt spring or bridle strap. Whereas the butt spring applies a continuous force on the hammer, a smoother trajectory is acquired when there is no force from the bridle strap on the hammer (the black-dotted curve in the figure).

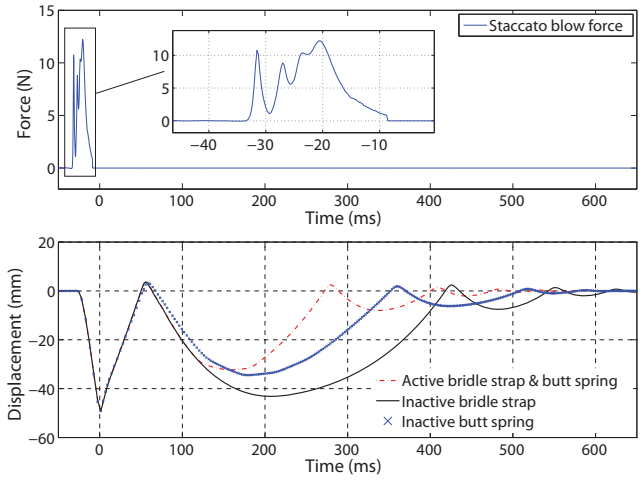

Figure 4.24: Staccato blow force profile (top) and simulation results for hammer horizontal motion (bottom) in different scenarios.

The simulation and experimental results for the hammer horizontal motion and bridle strap force are shown in Figure 4.25. The bridle strap and butt spring are active in this case and influence the dynamic response of the action. The force produced by the strap is calculated according to the nonlinear behavior of the component, which is calibrated using experimental measurements. This force was zero for the piano-pressed and forte-pressed blow forces. It is worthwhile to note that the bridle strap acts on the hammer several more times in the absence of the butt spring, as illustrated in Figure 4.26. The magnitude of the largest pulse in the applied force is unexpectedly smaller in this case, which can be justified as follows: since the speed of pre-impact increases in the absence of the butt spring force, so too does the rebound between the hammer and the string. Consequently, the action of the bridle strap force will be slower, as the hammer is closer to the whippen with less relative speed.

Removing each of the components and studying the obtained dynamic responses reveals

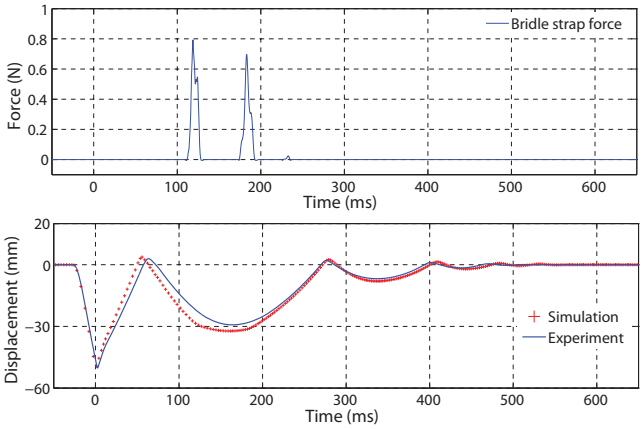

Figure 4.25: Bridle strap force (top) and hammer horizontal motion (bottom) for staccato blow force profile.

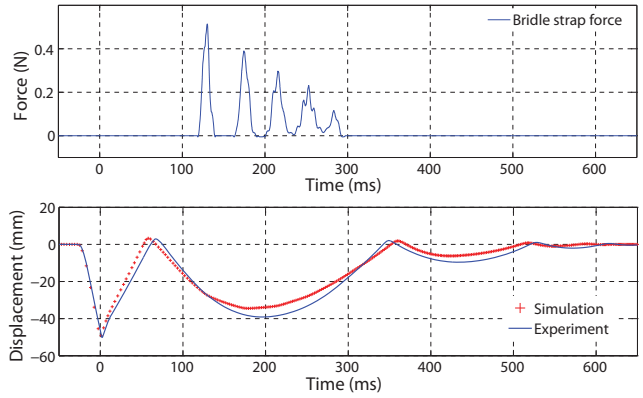

Figure 4.26: Bridle strap force (top) and hammer horizontal motion (bottom) with inactive butt spring and active bridle strap.

the necessity of employing both of them in the action model. By comparing the simulation and experiment for possible scenarios (removing and keeping the butt spring and bridle strap), the accuracy of measuring the parameters like butt spring constant and bridle strap performance can be assessed and verified. Figures 4.26 and 4.27 show the simulation and experimental results obtained when the butt spring and bridle strap are inactive in the action, respectively. Good agreement confirms the precise design approaches that have been applied in modeling the vertical action mechanism. Although the simulated action

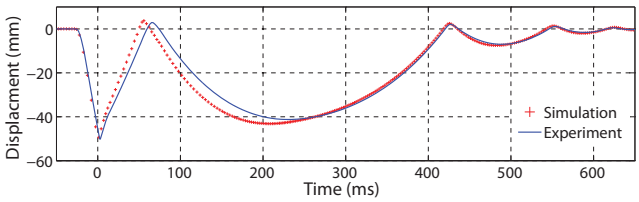

Figure 4.27: Hammer horizontal motion with active butt spring and inactive bridle strap.

performs well in responding to various inputs, developing a mechanistic and more precise contact model is still highly desirable.

4.2.5 Action simulation results including micromechanical contact model

The idea developed in the micromechanical modeling of fiber assemblies, designed for application in multibody simulations, along with the procedure mentioned in Section 4.1.5, was used in the hammer-string contact model of the vertical piano action.

The simulation stages for multibody dynamics of the piano action, incorporating the micromechanical contact model, is shown in Figure 4.28. In each step of simulation, the generalized coordinates and speeds are computed using a numerical integration method. By applying kinematic relations, along with these coordinates and speeds, the penetration depth and relative normal speed between interacting bodies at the point of contact will be estimated. This normal speed distinguishes between loading and unloading stages. On one hand, penetration depth, or volume fraction, is used to calculate the elastic portion of the pressure due to the interpenetration between bodies (equation 3.64 with the identified parameters for the felt-lined interfaces), and on the other hand, to obtain critical angle of sliding, which is used to estimate the contribution of friction in the overall pressure generated between contacting bodies. The obtained overall contact pressure/force between

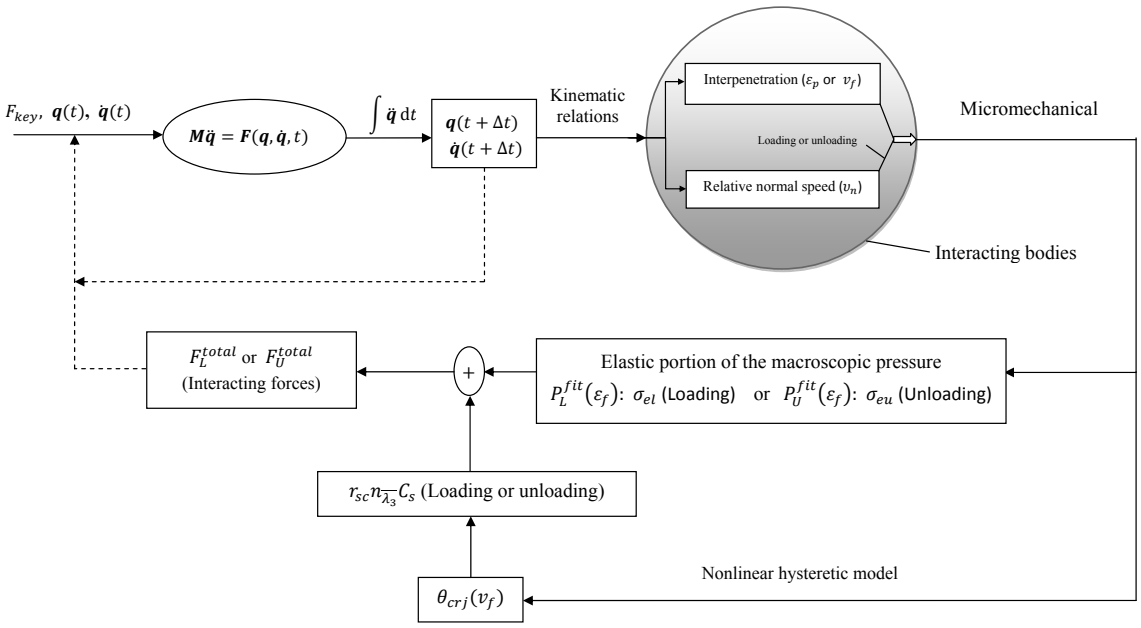

Figure 4.28: The procedure for dynamic simulation of the vertical piano action incorporating the micromechanical contact model at interfaces.

the bodies (calculated by adding the hysteresis part to the elastic part), along with the generalized coordinates and speeds is fed-back to the input for the next step of simulation. Simulation code was changed in order to incorporate the micromechanical approach into the multibody dynamics of the action. Parallel programming techniques appear to be necessary to acquire the simulation results in a reasonable amount of time.

As anticipated, the results did not change significantly in comparison to the simpler mathematical contact model; the main difference was the simulation time. For piano and forte force profiles, the simulation results accord with the experimental results very well, as illustrated in Figure 4.29. Accordingly, the proposed approach may be a superior candidate for incorporating micromechanical models into the simulation of multibody systems where the interfaces of the interacting bodies are lined with fiber networks. Using a 2.40-GHz quad-core processor, the simulation times for the piano and forte inputs were 1113 s and 1595 s, respectively. Although these simulations took longer than those using the mathematical contact model, where the CPU running times were, respectively, 262 s and 269 s for piano and forte inputs, this technique is still encouraging for multibody simulations.

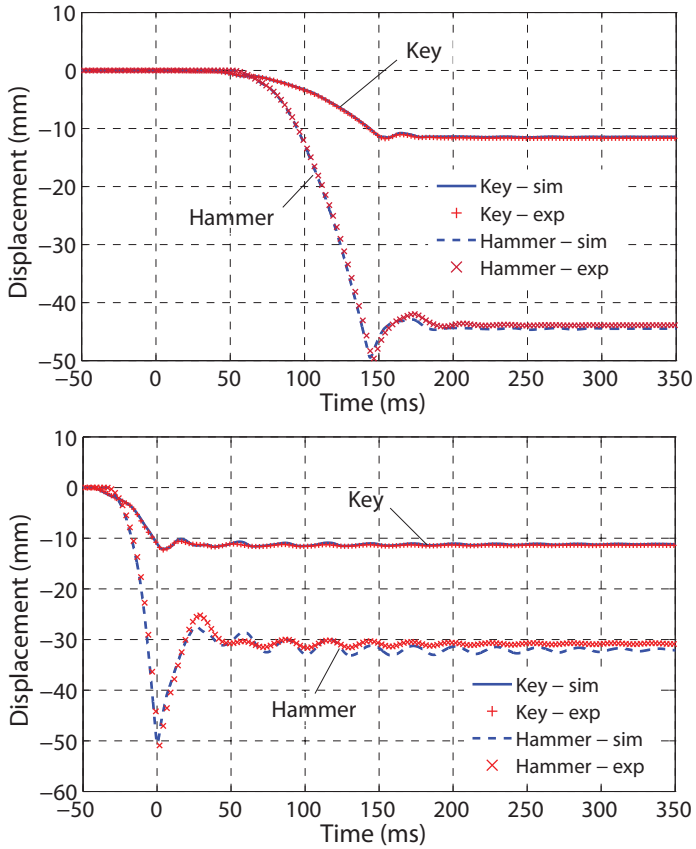

Figure 4.29: Hammer horizontal and key vertical motion, applying the micromechanical contact model for piano (top) and forte (bottom) inputs.

4.3 Chapter summary

The theoretical framework for constructing a mechanistic multibody dynamic model of a vertical piano action was described, and its experimental regulation and general validity were established in this chapter. Some possible features in developing more realistic components in the piano action were introduced, then the affect of applying those model considerations to the overall dynamic response of the action were theoretically analyzed and experimentally validated. The experimental procedure utilized to estimate the displacement and speed of designated tracking (marked) points on different bodies of the prototype action was established. Validation of the proposed contact models, the action parameters measured using experiments, and the GTM-based modeling software was accomplished by

comparing the simulation results with the experimental ones, applying inputs with significantly different features to the action. The importance of precise event timings, action regulation, and including more complicated action components was studied by utilizing different validation scenarios. Backcheck wire flexibility and compliance in the string used for modeling hammer-ground contact affected the dynamic behavior of the action significantly, so should not be ignored in the action modeling. The hammer shank flexibility revealed more influence for more rigorous inputs to the action. The essential roles of the butt spring and bridle strap in the vertical piano action were investigated and verified by experiments, applying a detached input, such as a staccato blow, on the key, which ensures activation of these components during the key stroke. The consistency between simulation and experimental results for various inputs and scenarios to the action confirmed the reliability and accuracy of the model and experimental procedure. Two contact models were examined, a mathematical and a micromechanical approach, and the applicability of the (more complicated) micromechanical contact model in simulating multibody systems with interacting felt-lined bodies was confirmed.

Chapter 5

Dynamic Simulation and Vibration Analysis of a Piano Key Actuator

Studying the dynamic and vibration behavior of the device used to generate finger-key contact force profiles that realistically replicate that of a real pianist's finger is the main objective of this chapter.[1] This is particularly important when a motion profile, instead of force inputs, is applied to the piano action model. The finger actuator mechanism proposed by Hirschkorn et al. [35], reproducing the finger force on the key, is used as the prototype model. The focus is on the hub, arm, and tip mass dynamics, so it can be easily adjusted for the current mechanism that was used for experimental validation of the vertical action mechanism. As shown in Figure 5.1, the actuation system consists of a flexible arm attached to a DC brushless rotary motor through a hub. The compliant arm behaves as a cantilever beam to which an eccentric tip mass has been attached at its free end. During the piano key stroke, the contact force input from the tip causes the key to rotate and impact the ground through an interface lined with stiff felt to suppress vibrations and noise. Euler-Bernoulli beam theory in conjunction with Lagrange's method is utilized to obtain the governing equations of motion for the system. The finite element method is used as the discretization procedure for the flexible cantilever beam, which can be considered a distributed parameter system. To include contact dynamics at the stop, the nonlinear hysteretic behavior of felt under compression is modeled in such a way that smooth transitions between loading and unloading stages are produced, ensuring accurate response under dynamic conditions, particularly with partial loading and unloading states that occur during the contact period. The contact force model has been discussed thoroughly in the Section 4.1.4.

[1] Most of the materials in this chapter have been presented by R. Masoudi, S. H. Birkett, and A. Salehian [66] at the ASME IDETC/CIE 2011 conference held in Washington, DC, USA.

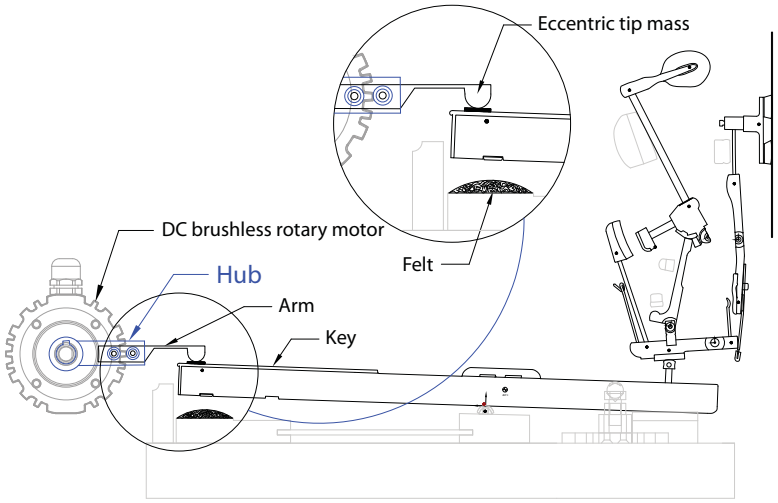

Figure 5.1: Key actuation system with the prototype upright piano action mechanism.

Force readings from a sensor on the key, comparing the forces generated from the actuator mechanism and real pianist finger on a typical grand piano action, are shown in Figure 5.2 [35]. The rigidity of the actuation system, and in particular that of the aluminum arm, is likely responsible for the undesirable strong vibrations observed in the input force profile, notably during the impact event as the key strikes the stop underneath. In comparison, these vibrations, though also present in the force profile recorded from a pianist's key input, are of much smaller amplitude and strongly damped.

For the automated key actuator, arm flexibility should reflect the overall biomechanical compliance of the pianist, including that of the fingertip pulp, as seen at the key surface. Since the arm acts as a flexible beam, its characteristics can produce undesired reaction forces, especially during the contact period between the felt under the key front and the key. The problem is analyzed here by constructing a dynamic model of the overall actuation system, including the input torque produced by the motor, the hub, flexible arm, eccentric tip mass at the end of the arm, and the contact interface between key and stop. The Finite Element Method (FEM) is utilized for the flexible arm, in part because it is possible to allow the cross section to vary along the arm axis. A continuous contact dynamic model, in which the contact force is expressed as a function of local deformation and relative velocity of penetration between objects, is also applied. Simulations are used to study how the finger contact force profile at the key is influenced by the geometrical and material properties of the arm. Additionally, the effect of incorporating various damper types into the actuator design is investigated.

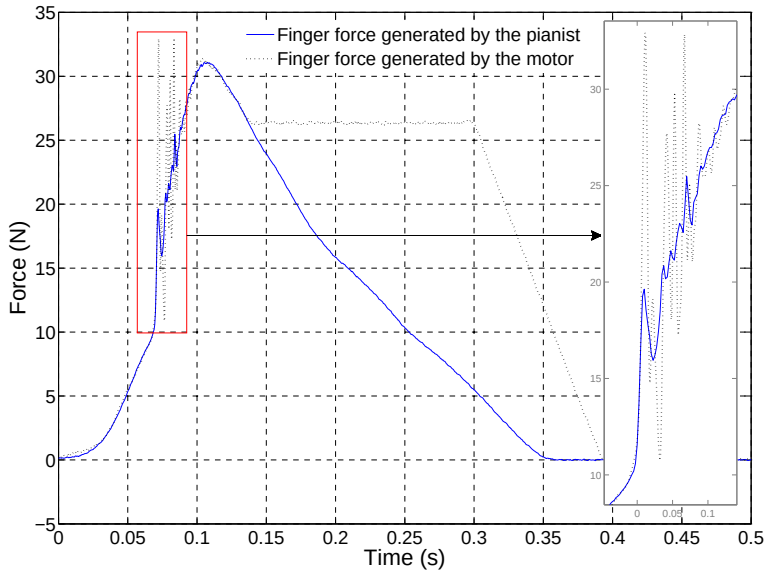

Figure 5.2: Typical forte blow forces generated by the pianist and motor actuator with aluminum arm measured by the load cell on the key (Hirschkorn [35]).

5.1 Actuation system dynamic model

5.1.1 Equivalent dynamic response of the action mechanism

In the actuation system shown in Figure 5.1, the motor generates a prescribed torque on the hub, nominally determined by the open-loop control objective of replicating the force profile as measured from a pianist's finger. Through contact with the key surface the input force is exerted on the key via the arm attached to the hub. Two different types of arm, a wood and an aluminum arm with different shapes, have been used to investigate vibration behavior of the system for the specified torque applied on the hub. As the focus in this research is on the actuation system and its influence on vibrations, for our model the load profile from the piano action has been replaced by a simple equivalent reaction force derived from the measured real force between actuator tip and key surface when the same input torque is applied on the hub. This is a rational approximation, considering that the action modeling including its interaction with the actuation mechanism is in itself a major research project. Moreover, by this assumption, a good estimate has been achieved for the total force generated by the piano mechanism due to the bodies' acceleration and vibration, inertias, and even joint friction in reaction to the same input on the hub. As

shown in Figure 5.3, the dynamic response of the piano action mechanism is replaced with the equivalent force (F_{action}) on the finger tip, which will be negligible after the key touches the balance rail felt (during key-balance rail contact). F_{felt} is the contact force between the key and felt underneath, which mathematically is represented by a Heaviside function in terms of penetration depth, i.e. the force is zero when there is no contact. It is important to note that the key is assumed to transfer the contact force from the felt to finger arm directly, i.e. the key and finger contact in Figure 5.1 is considered to be permanent and undetachable during the simulation.

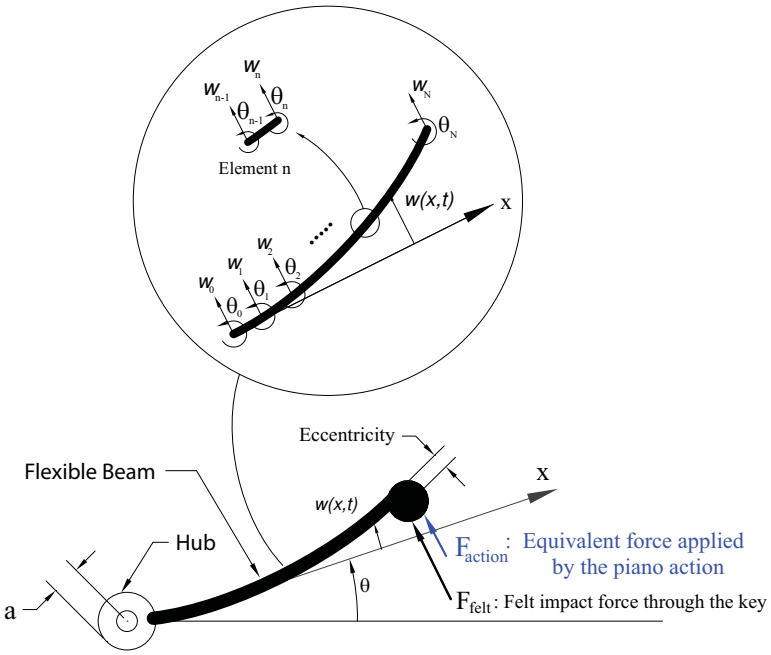

Figure 5.3: Schematic of the simplified actuation system.

5.1.2 Dynamic modeling and FEM discretization

As shown in Figure 5.3, the actuation system consists of a rotating hub with a flexible cantilever beam fastened tightly to its free end. An eccentric tip mass has been attached to its free end in order to transfer the torque applied on the hub through the arm to the key in a continuous fashion. Euler-Bernoulli beam theory in conjunction with Lagrange's method is utilized to obtain the equations of motion for the system. Due to its versatility

and high accuracy, the FEM is used as the spatial discretization procedure for the flexible beam, which can be considered a distributed-parameter system.

Finite element discretization

The spatial configuration of a typical point on the actuator consists of a rigid-body motion due to rotation θ of the hub and elastic displacements due to flexibility of the beam. As illustrated in Figure 5.3, according to Euler-Bernoulli assumptions for the beam, each element of the flexible beam has two nodes and every node possesses two degrees of freedom, a transverse deflection and a rotation. The elastic displacement $w_n(x,t)$ for the element n can be expressed as [15]

$$w_n(x,t) = \sum_{j=1}^{4} \phi_{jn}(x) q_{jn}(t) \tag{5.1}$$

in which we assume the following shape functions:

$$\begin{aligned} \phi_{1n}(x) &= 1 - 3\frac{\hat{\beta}^2}{l_n^2} + 2\frac{\hat{\beta}^3}{l_n^3} \quad \phi_{2n}(x) = l_n\left[1 - 3\frac{\hat{\beta}^2}{l_n^2} + 2\frac{\hat{\beta}^3}{l_n^3}\right] \\ \phi_{3n}(x) &= 3\frac{\hat{\beta}^2}{l_n^2} - 2\frac{\hat{\beta}^3}{l_n^3} \qquad \phi_{4n}(x) = l_n\left[-\frac{\hat{\beta}^2}{l_n^2} + \frac{\hat{\beta}^3}{l_n^3}\right] \end{aligned} \tag{5.2}$$

and

$$\begin{aligned} \hat{\beta} = x - x_{n-1}, \;\; q_{1n}(t) = w_{n-1}, \\ q_{2n}(t) = \theta_{n-1}, \;\; q_{3n}(t) = w_n, \;\; q_{4n}(t) = \theta_n \end{aligned} \tag{5.3}$$

where $\phi_{in}(x)$ is the i^{th} shape function for the n^{th} element, w_n and w_{n-1} are the elastic deformations at the end nodes of the n^{th} element, θ_n and θ_{n-1} are rotations at the end nodes, and l_n is the length of the element n. The above equations can be written in a local nondimensional coordinate, s, which is related to the beam coordinate, x, according to the following linear transformation [15]

$$x = x_{n-1} + l_n s, \;\; 0 \le s \le 1 \tag{5.4}$$

In matrix form, equation 5.1 will be

$$w_n(s,t) = \{\phi\}_n^T \{q\}_n \tag{5.5}$$

in which $\{\phi\}_n = \{\phi_{1n}(s)\ \phi_{2n}(s)\ \phi_{3n}(s)\ \phi_{4n}(s)\ \}^T$ and $\{q\}_n = \{w_{n-1}\ \theta_{n-1}\ w_n\ \theta_n\ \}^T$.

Governing differential equations

To obtain the dynamic equations governing the behavior of the system, Lagrange's method is employed in which the kinetic and potential energy of the whole system should be calculated. To apply the approach, kinetic and potential energies associated with each component of the mechanism will be calculated and then its contribution in the overall dynamic behavior of the system is introduced into the global coefficient matrices of the dynamic equations. If we consider N elements for the flexible beam, the generalized coordinates for the whole system will be:

$$\boldsymbol{q}_{2N+3\times 1} = \{\theta\ \ w_0\ \ \theta_0\ \ w_1\ \ \theta_1\ \ ...\ \ w_N\ \ \theta_N\}^T \tag{5.6}$$

• *Kinetic energy for a typical element* $\boldsymbol{n}$*:*

For small elastic deflections, the position and speed of a typical point p on the flexible beam, x_p and $\dot{x}_p$, will be

$$x_p = (x+a)\theta + w_n(x,t) \quad \Rightarrow \quad \dot{x}_p = (x+a)\dot{\theta} + \dot{w}_n(x,t) \tag{5.7}$$

By substituting equation 5.1, the speed can be written in another form as

$$\dot{x}_p = [x+a\ \ \phi_{1n}(x)\ \ \phi_{2n}(x)\ \ \phi_{3n}(x)\ \phi_{4n}(x)] \times \begin{Bmatrix} \dot{\theta} \\ \dot{w}_{n-1} \\ \dot{\theta}_{n-1} \\ \dot{w}_n \\ \dot{\theta}_n \end{Bmatrix} = \boldsymbol{\eta}^T \{\dot{q}\}_n \tag{5.8}$$

in which a is the equivalent radius of the hub. Using equation 5.7 and the transformation defined in equation 5.4, the kinetic energy for the element n is

$$KE_n = \int_{x_{n-1}}^{x_n} \tfrac{1}{2}\rho_n A_n \dot{x}_p^T \dot{x}_p \,\mathrm{d}x = \tfrac{1}{2}\int_0^1 \rho_n A_n l_n \{\dot{\hat{q}}\}_n^T \boldsymbol{\eta}\boldsymbol{\eta}^T \{\dot{\hat{q}}\}_n \,\mathrm{d}s = \tfrac{1}{2}\{\dot{\hat{q}}\}_n^T \boldsymbol{M}_n \{\dot{\hat{q}}\}_n \tag{5.9}$$

where $\boldsymbol{M}_n = \int_0^1 \rho_n A_n l_n \boldsymbol{\eta}\boldsymbol{\eta}^T \,\mathrm{d}s$ is the 5×5 local mass matrix, ρ_n is density, and A_n is cross section area of the n^{th} element. To get the global mass matrix, all elements' mass matrices should be assembled in a way that their components are placed in corresponding location in the global mass matrix. It is illustrated schematically in Figure 5.4.

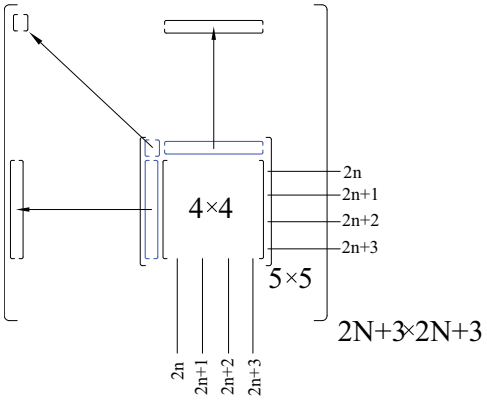

Figure 5.4: Schematic procedure of assembling the global matrices.

• *Kinetic energy for the tip mass and the hub:*

The tip mass undergoes translational and rotational movement due to rigid-body motion and vibrations of the arm:

$$\begin{cases} KE_{\text{tip mass}} = \tfrac{1}{2}m_{_T}\dot{w}_{_N}^2 + \tfrac{1}{2}m_{_T}(L+a)^2\dot{\theta}^2 + m_{_T}(L+a)\dot{\theta}\dot{w}_{_N} + \tfrac{1}{2}m_{_T}r^2\dot{\theta}_{_N}^2 = \\ \qquad\qquad \tfrac{1}{2}\dot{\boldsymbol{q}}^T\boldsymbol{M}_{\text{tip}}\dot{\boldsymbol{q}} \\ KE_{\text{hub}} = \tfrac{1}{2}J_{_H}\dot{\theta}^2 = \tfrac{1}{2}\dot{\boldsymbol{q}}^T\boldsymbol{M}_{\text{hub}}\dot{\boldsymbol{q}} \end{cases} \tag{5.10}$$

in which $m_{_T}$ is the tip mass, L is the length of the beam, r is eccentricity, and $J_{_H}$ is the

moment of inertia of the hub. $\boldsymbol{M}_{\text{tip}}$ and $\boldsymbol{M}_{\text{hub}}$ can be calculated by placing the obtained terms in equation 5.10 in their appropriate locations in these matrices. Total kinetic energy will have the final form:

$$KE = \frac{1}{2}\dot{\boldsymbol{q}}^T \boldsymbol{M} \dot{\boldsymbol{q}} \tag{5.11}$$

in which the global mass matrix, $\boldsymbol{M}$, can be acquired by summation of the obtained local mass matrices.

• *Potential energy for the flexible beam:*

Potential energy for the flexible beam element n can be obtained by

$$PE_n = \frac{1}{2}\int_{x_{n-1}}^{x_n} E_n I_n \left(\frac{\partial^2 w_n(x,t)}{\partial x^2}\right)^2 \mathrm{d}x = \frac{1}{2}\{\hat{q}\}_n^T \boldsymbol{K}_n \{\hat{q}\}_n \tag{5.12}$$

where E_n and I_n are the modulus of elasticity and second moment of area of the n^{th} element, respectively. The assembling procedure to achieve the global stiffness matrix, $\boldsymbol{K}$, is the same as described before. The potential energy for the beam can be written as

$$PE = \frac{1}{2}\boldsymbol{q}^T \boldsymbol{K} \boldsymbol{q} \tag{5.13}$$

• *Generalized forces:*

The generalized forces used in Lagrange's formulation are due to torque applied by the motor on the hub, the equivalent reaction force, and the key-stop contact force which exists only when contact is detected. The effect of gravity is included in generalized force because of its nonlinear relation with the generalized coordinates. Altogether, we have

$$\delta W_{F(t)} = \delta W_{\left(T_h + F_{\text{action}} + F_G + H(\varepsilon_p) F_{\text{felt}}\right)} \tag{5.14}$$

where T_h is the applied torque on the hub by the motor, F_{action} is the equivalent reaction force from the piano action, F_G is the force due to gravity, $H(\varepsilon_p)$ is the Heaviside step function, ε_p is the penetration depth of the virtual key in the felt underneath during the

contact, and F_{felt} is the corresponding contact force. In order to get the generalized forces, the virtual work done by these forces should be calculated:

$$\delta W_{\text{hub}} = T_h \delta\theta, \qquad \delta W_{\text{action + felt}} = (F_{\text{action}} + H(\varepsilon_p) F_{\text{felt}}) \left((L+a)\delta\theta + \delta w_{_N}\right)$$

$$\delta W_{\text{Gravity}} = -\cos\theta \left(\sum_{n=1}^{N} \int_{x_{n-1}}^{x_n} \rho A g((x+a)\delta\theta + \delta w)\, \mathrm{d}x + m_{_T} g((L+a)\delta\theta + \delta w_{_N}) \right) \tag{5.15}$$

It is important to note that in our calculations we assumed small elastic deflections for the arm. The assembling procedure for the generalized force due to gravity for the flexible beam is similar to the one used for the mass and stiffness matrices. The equations of motion can be obtained using Lagrange's equations in matrix form as

$$\frac{\mathrm{d}}{\mathrm{d}t}\left(\frac{\partial \mathscr{L}}{\partial \dot{\boldsymbol{q}}}\right) - \frac{\partial \mathscr{L}}{\partial \boldsymbol{q}} = \boldsymbol{Q} \tag{5.16}$$

in which $\mathscr{L}$ is the Lagrangian $\mathscr{L} = KE - PE$ and $\boldsymbol{Q}$ is the generalized force vector. Therefore, the governing differential equations will be in the form

$$\boldsymbol{M}\ddot{\boldsymbol{q}} + \boldsymbol{K}\boldsymbol{q} = \boldsymbol{Q} \tag{5.17}$$

It is worthwhile to notice that the original equations governing the dynamic behavior of the actuation system are of a hybrid type in which both ODEs of rigid-body motion and PDEs of elastic vibrations are involved. The discretization approach was utilized to develop the overall dynamic equations in the form of highly nonlinear ODEs.

Contact mechanics modeling

In dynamic modeling of the actuation system, the kinematic constraints at the contact interface between key and stop rail felt are not simple, because these bodies are not always in contact during input from the actuator. Therefore, exactly the same continuous analysis introduced in the vertical action model is used to model impact in terms of coupled applied forces that act during the contact period. For simplicity, we used the mathematical

approach, although the simulation results with the micromechanical model will be nearly the same. Fit curves were calculated for both loading and unloading data in the following form

$$F_{fit}(\varepsilon_p) = a\varepsilon_p e^{b\varepsilon_p} + c\varepsilon_p \tag{5.18}$$

in which F_{fit} is the fit curve function, ε_p is the penetration depth between two interacting bodies, and a, b, and c are constant parameters. Contact force is zero for negative penetration depths, i.e. for non-colliding bodies, which is modelled by the Heaviside function.

To model the hysteretic behavior and consider partial loading and unloading during interactions, the following mathematical relation is applied:

$$F_{\text{felt}} = f_n(\varepsilon_p, \nu_n) = \begin{cases} F^l_{fit}(\varepsilon_p), & \text{if } \nu_n \geq 0 \\ F^l_{fit}(\varepsilon_p) + \delta_{lu}(\varepsilon_p)\ \tanh(\alpha\nu_n) & \text{if } \nu_n < 0 \end{cases} \tag{5.19}$$

where $f_n(\varepsilon_p, \nu_n)$ is the normal contact force, $\delta_{lu}(\varepsilon_p) = F^l_{fit}(\varepsilon_p) - F^u_{fit}(\varepsilon_p)$ is the difference between loading and unloading fit at each penetration depth, α is a parameter that controls the transition speed between loading to unloading states, and ν_n is the normal speed between the two surfaces at the contact point, which also influences the transition.

5.2 Simulation and numerical results

5.2.1 Actuation mechanism without damping

As the vibration response of the actuator is characterized mainly by its behavior during contact with the stop, the only significant input requirement is to ensure that a realistic impact speed is achieved, and that sufficient force is provided to hold the key down on the felt after impact. Consequently, a simple ideal ramp function from zero to 3 N·m in the first 0.06 s, with subsequent constant holding torque of 3 N·m, is used for input torque in the simulation. To extract geometrical and mass information for the hub and arms, a 3D-model for each body was constructed in SolidWorks software [99] and estimates of location of center of mass and the mass moment of inertia about center of the hub were extracted from the CAD model. As shown in Figure 5.5, two types of arms have

been considered in replicating the desired finger-key contact force. Numerical values of the actuator mechanism parameters including mass and structural parameters of the hub, wooden arm, and aluminum arm are listed in Appendix B.

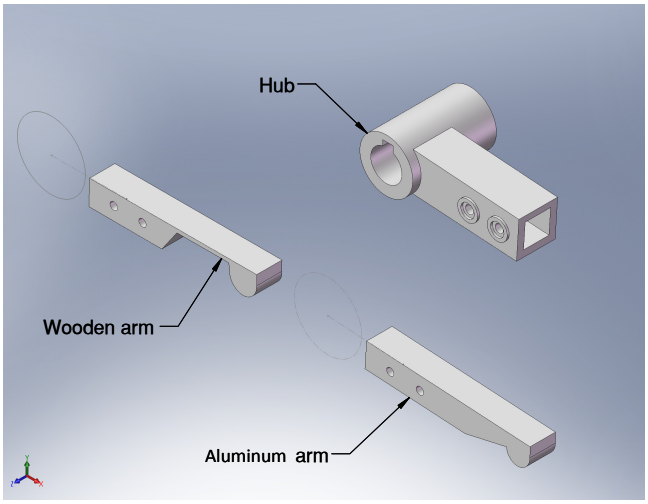

Figure 5.5: Hub and arms utilized in the simulation model and experimental prototype.

Using the symbolic capabilities of Maple software [64], we obtained the local mass, stiffness, and generalized force matrices, including effect of gravity, for each element. The associated global matrices are obtained by exporting the matrices into MATLAB® [67] and assembling them using the procedure discussed in the previous sections. In this work, a stiff solver, ODE15s, was applied and the results for rotation angle and tip deflection of the wood and aluminum arms are shown in Figures 5.6 and 5.7.

As can be expected, the vibrations for the wooden arm are more severe in terms of magnitude and duration compared to the stiffer aluminum arm. These vibrations can affect the dynamic behavior of the key, and thereby also the whole piano action response. Thus, comparing the oscillations with the experiment in the future can help us in developing a more realistic actuation system as the input to the piano action mechanism. Finger-key contact force as would be measured by a force sensor between input arm and key can be calculated for simulations by adding the reaction force generated by the piano action to the interaction force between key and felt.

Simulation results for the two types of finger arm are shown in Figure 5.8. The similarities between the simulated force profile for the aluminum arm and that generated by the actual motor aluminum arm (dotted curve in Figure 5.2) confirm that the assumptions and simplifications used in modeling the actuator system are reasonable. It is worthwhile to

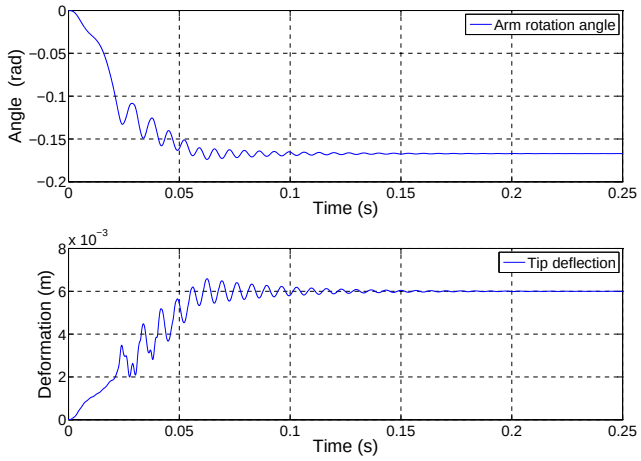

Figure 5.6: Simulated rotation angle and tip deflection of the wood arm in case of no damping.

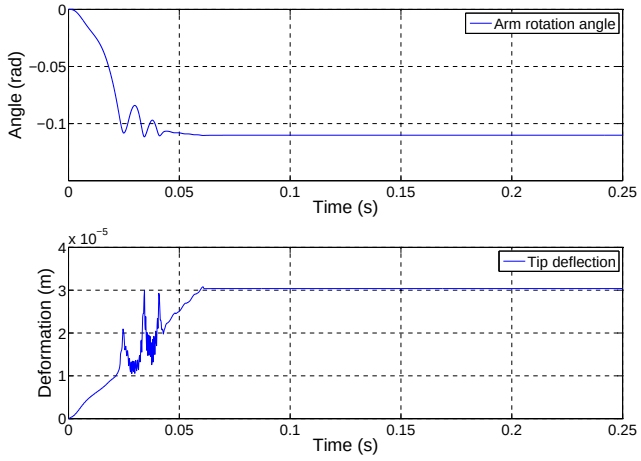

Figure 5.7: Simulated rotation angle and tip deflection of the aluminum arm in case of no damping.

note that the difference between the first peak in the force profiles results mostly from the different reaction from the piano action compared to the approximate reaction force used in simulations; however this does not affect significantly the conclusions about vibration response. Furthermore, the torque applied on the hub by the motor is somewhat different from the ideal torque profile used for simulations. A rigid actuator such as the one with the aluminum arm produces larger amplitude vibrations with longer duration than does a pianist's finger. Adding compliance to the arm has been proposed to improve this situation, for instance through the use of a flexible wooden arm, but, as can be seen in the simulation results of Figure 5.8, this is not sufficient to eliminate the problem. Additionally, some source of damping must be incorporated into the actuation system, if the input response is to better match that of the pianist. Two types of damper are considered in the following sections.

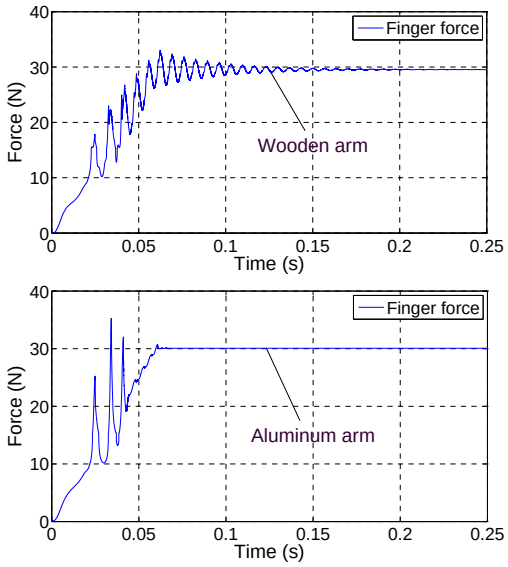

Figure 5.8: Simulated finger force generated between key and tip mass for wooden and aluminum arms in case of no damping.

5.2.2 Simple grounded rotary dashpot at the hub

A grounded dashpot at the hub, in which one end is fixed at the ground and the other end to the hub, has been applied to the system with the wooden arm. The simulation results shown in Figure 5.9 for a damping ratio $c = 0.0075$ N/(m/s) confirm that combining the

compliance of the wooden arm and damping properties of the dashpot is encouraging in achieving a more realistic finger force profile. Moreover, the undesired oscillations due to flexibility of the wooden arm are eliminated in an appropriate manner when compared to the real finger force shown in Figure 5.2.

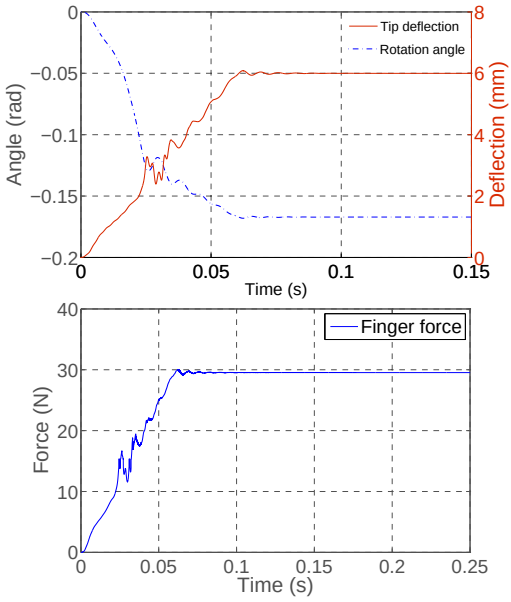

Figure 5.9: Time history of simulated tip deflection, wooden arm rotation angle, and finger force with simple damping applied at the hub.

5.2.3 Grounded one-sided rotary dashpot

The simple dashpot added to the actuator causes a delay in the first impact between key and felt and also in the pre-impact force profile due to the dashpot opposing force. To solve this undesired delay, a grounded one-sided rotary dashpot, in which the torque is generated only when the actuator rotates in the direction that releases the key, is utilized. Consequently, the excessive vibrations in the undamped actuation model are eliminated with the same pre-impact force profile and identical time of first contact between key and felt. The results for damping coefficient $c = 0.05\,\mathrm{N/(m/s)}$ are shown in Figure 5.10. Comparing the pre-impact portion of the force profiles in Figures 5.9 and 5.10, confirms the existence of some differences in the magnitude, shape, and time of first impact. These can affect the timing in studying the dynamic behavior of the whole piano action mechanism.

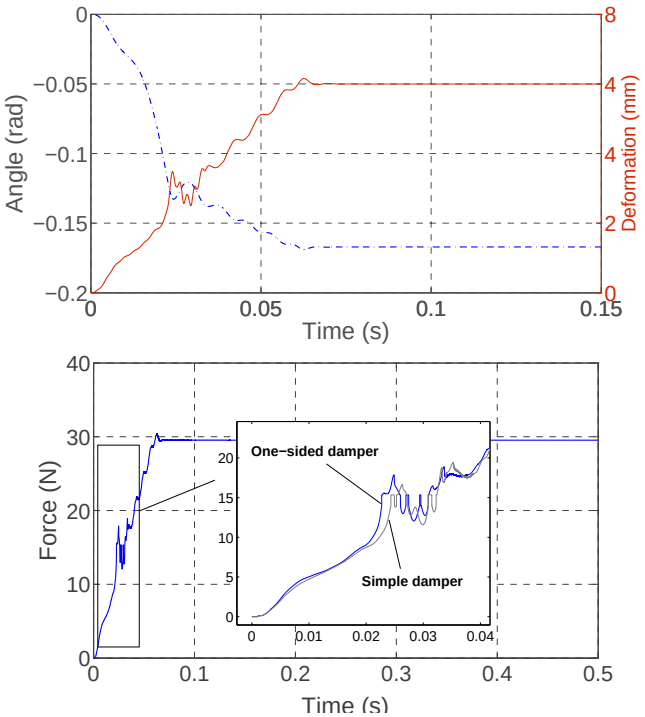

Figure 5.10: Time history of simulated tip deflection, wooden arm rotation angle, and finger force with one-sided damping applied at the hub.

It is important to note that the level of damping is different for each case to achieve reasonable results.

5.2.4 Discussion

As expected, by increasing the stiffness of the arm we obtained short-lasting oscillations with greater peaks during contact in the finger force profile. It can be observed in Figure 5.7 that the aluminum arm, which has more stiffness and also thicker cross section area, is undergoing more rigorous vibrations with greater amplitude of oscillations during contact. Hence, a more compliant component is required to approach the more realistic profile similar to the finger tip force. The occurrence of the first contact is seen at 0.032 s according to the contact force profile. At this time, an increase in the vibration of the flexible arm and also a significant change in rotation angle of the hub and finger force are noticed. Simulation results are in good agreement with our prediction from the physics of the system and also

qualitatively with the experiments using an aluminum arm, as seen in Figure 5.2. Using a wooden arm with different geometry and rigidity was a good candidate to add the required flexibility to the actuation mechanism; however this showed more vibrations and continued oscillations during the post-impact period. Adequate damping as in the pianist's finger and body is necessary to suppress these excessive vibrations. Two amelioration strategies were utilized and compared.

By applying a rotational grounded dashpot on the hub, the elastic vibrations of the wooden arm are reduced considerably. This will especially affect the amplitude of finger force profile and the successive post-impact oscillations, as shown in Figure 5.9; however, due to continuous action of the damper in both positive and negative directions of the hub rotation, the time of the first contact is delayed and the obtained pre-contact profile is somewhat different. This delay can be seen in Figure 5.11 in which the same level of damping is used in the two cases. Finally, the results improved remarkably by using a rotational

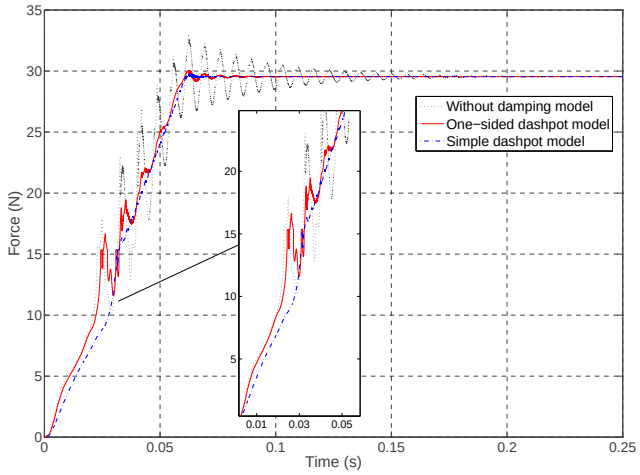

Figure 5.11: Comparison of actuator tip-key (total) force for three models of the actuation system in case of wooden arm.

grounded one-sided dashpot. This kind of damper acts only when the angular velocity of the arm is in the positive direction and so will not affect the acceleration/force profile before contact, which may influence the dynamic behavior and timing when an actuator is used to drive a real piano action experimentally. Although this type of damping exhibits more oscillations in comparison to the simple dashpot (with the same level of damping), it is preferred to be utilized for experiments to achieve more realistic results, especially when the simple equivalent reaction force is replaced by the real dynamic response of the whole piano action mechanism.

5.3 Chapter summary

Developing a device to achieve a desired finger-key contact force profile that realistically replicates that of a real pianist's finger was the main objective of this chapter. The proposed actuation system consists of a flexible arm which is attached to a DC brushless rotary motor through a hub. The compliant arm behaves as a cantilever beam to which an eccentric tip mass has been attached at its free end. During the piano key stroke, the contact force input from the tip causes the key to rotate and impact the ground through an interface lined with stiff felt to suppress vibrations and noise. Euler-Bernoulli beam theory in conjunction with Lagrange's method is utilized to obtain the governing equations of motion for the system. The finite element method is used as the discretization procedure for the flexible cantilever beam, which can be considered a distributed parameter system. To include contact dynamics at the stop, the nonlinear hysteretic behavior of felt under compression is modeled in such a way that smooth transitions between loading and unloading stages are produced, thus ensuring accurate response under dynamic conditions, and particularly with partial loading and unloading states that occur during the contact period. Simulation results show excessive vibration is produced due to the arm flexibility and also the rigid-body oscillations of the arm, especially during the period of key-felt contact. To eliminate these vibrations, the system was supplemented with various dashpot models, including a simple grounded rotational dashpot, and a grounded rotational dashpot with a one-sided relation. The results of simulations are presented showing the effect on vibration behavior attributed to these additional components. A combination of the actuator system model and the piano action mechanism would be a challenging project to study the dynamic response of the piano action as well as its interaction with the actuator in a more realistic manner, which can be left for future work.

Chapter 6

Conclusions

In this research, predicting the response of random fiber networks subjected to compression loading schemes, on the basis of geometric features of the structure and the mechanical behavior of individual constituent fibers, has been explored. We discussed the structural characterization and architectural parameters required in developing a theoretical formulation representing the macroscopic behavior of the network in terms of the microscopic response of elemental units within the network. Well-established criteria for estimating the number of fiber contacts in structures with randomly-distributed fibers were presented. The compressional behavior of random fiber masses with high volume fraction was examined by applying two micromechanical approaches: granular media, in which the pressure on the network flows into the network through contacts between grains (fibers); and a continuum model in which elongation of the fibers is the predominant deformation scheme at the microscale. Performance of the methods in estimating the micromechanical features of wool felt was analyzed through comparison to experimental pressure-deformation data. Although fairly good results were achieved by applying the granular-based approach to the felt experimental data, the physical significance of the optimized parameters was not meaningful enough to utilize this strategy for constructing a mechanistic model.

In the case of felt materials formed by interlocked wool fibers, a binomial distribution of the number of fiber-to-fiber contacts, along with a normal orientation distribution of imaginary straight fibers between neighboring contact points, accords the unique nonlinear behavior of felt, assuming that bending of the fiber dominates the other deformation schemes during the compression of the fiber mass. Adopting fiber-to-fiber friction in the interactions between fibers at the micro level, the nonlinear hysteretic phenomenon observed in felt was incorporated into the micromechanical model. The model was able to reproduce the hysteresis, generated from internal friction and structural parameter changes

during loading and unloading, in the compression behavior of the network, provided that structural information such as the critical angle of fiber sliding can be evaluated. The process of constructing a uniformly-distributed random fiber network, estimating structural parameters such as the proportion of slipping fibers, and calculating macroscopic pressure in terms of the obtained parameters and the micro-deformation of fibers, is computationally expensive and time-consuming. This makes the proposed approach inappropriate in multibody dynamic simulations with felt-lined interacting bodies. Thus, a novel technique was introduced to include the hysteresis in the force-penetration relation during contact in multibody systems, specifically that of piano action mechanisms. Smooth transition between loading and unloading stages during simulation was accomplished using a novel mathematical formulation; the idea used for the transition between kinetic and static friction in Coulomb friction models provided the inspiration for this strategy.

The theoretical framework for constructing a fully mechanistic multibody dynamic model of a vertical piano action was described and its general validity was established in this thesis. Hammer-string interaction was included in the model, applying an elastic stiff string model proposed by Fletcher [25] and adapted for grand piano actions by Vyasarayani [117], then adjusted for the vertical action model. Observing significant vibrations in backcheck wire and hammer shank using high-speed video imaging, a flexible Euler–Bernoulli beam model was utilized to predict the deflection characteristics of these components. For simulation, parameters were obtained by the experimental testing and measurement of a physical prototype vertical action. Techniques were described for the virtual regulation of the model to ensure that the initial conditions and pseudo-static response accurately represent the precise configuration and desired relationships between the components during the key stroke. A sophisticated key pivot model, which was a modified version of existing models in grand piano actions, captured both the rotational motion and the vertical translation of the key as it can lift off the balance rail under some conditions. The performance of two components that are unique to the vertical action — the bridle strap and the butt spring — were examined, applying a specific input to the action by which the components are active during the key stroke. The force applied by the bridle strap on the hammer butt signifies the key role of this component in restraining the hammer motion in more rigorous inputs, such as a staccato blow force.

A dynamic model of a rotating flexible hub-beam system including contact, which represents the simulation model of the pianist's finger applied on the piano key, has been developed as a part of this research project. The more compliant arm (wooden arm) along with a one-sided damper applied on the hub was a promising combination to acquire a more realistic finger force from the simulated model, as compared to the experiments.

6.1 Contributions

Micromechanics of nonwoven fiber networks

Several micromechanical approaches in modeling the nonlinear compliance of bonded fiber networks, with relatively high volume fraction under compression loading schemes, were examined. A mechanistic model suitable for highly compressed fiber masses in small deformation ranges, which was based on the elongation of fibers at the microscale, was extended to the modeling of larger bulk deformations, applying a binomial distribution of fiber contacts. A random fabric structure was constructed to estimate the evolution of the network structure, including incremental changes in the structural parameters and the number of fiber contacts.

A well-established micromechanical model, built on a rate theory for granular solids, was utilized to study the compression behavior of felt. Applicability and performance of the complex mathematical model for studying uniaxial compression of felt was established. The obtained uncertainty parameters were used to predict the key microstructural deformation scheme in the network.

To capture hysteresis, the network was represented by two subnetworks: one to represent the proportion of fibers that do not slide and can be considered as a bonded fiber network, and the other portion in which fibers slide, which is the source of energy loss and the difference in structural parameters during loading and unloading stages. One of the significant contributions in this work is a micromechanical approach to model the elastic compression response of felt, due to non-sliding interconnections between fibers. In addition, a novel algorithm was introduced to include fiber-to-fiber friction for generating the observed compression hysteresis, which is computationally of low-cost and is fast enough to be appropriate in multibody dynamic simulations, still keeping the microscopic physical information in developing the model. This reflects a notable improvement in current contact models applied to grand piano mechanisms, in which viscoelastic relations were wrongly used to include force-deformation estimation in contact interfaces. The proposed technique has a wide range of engineering applications, particularly in multibody dynamic simulations with contact interfaces lined with fiber networks.

Dynamic simulations of a vertical piano action and the actuator mechanism

Developing a mechanistic vertical piano action mechanism was accomplished in this thesis. Fully symbolic equations of motion were derived and parameterized using an experimental prototype. The model includes hammer-string interaction, flexibility in the hammer

shank and backcheck wire, a sophisticated key pivot model, bridle strap and butt spring performance, and most importantly, a micromechanical contact model for hammer-string interaction. Also studied was a simulation model for the dynamic and vibration analysis of the actuator system, reproducing the pianist finger force. Furthermore, techniques to achieve a more realistic finger force on the action were examined.

6.2 Future work

Fiber assemblies - contact models

A comprehensive study is required on the structural characterization of compressed random fiber networks. Experimental procedures and sophisticated image analysis tools for estimating the distribution of fiber diameter and orientation, fiber crimp, and structural architecture are extremely important in constructing fiberwebs for a high-fidelity simulation. In-situ mechanical tests are encouraging methods for predicting the predominant structural deformation schemes in various fiber assemblies. More precise experiments are required to derive physical properties of constituent fibers and determine the way they interact with other fibers. To increase the fidelity of the simulated model, it should be extended to the case of non-uniform compression by an indenter with surface curvature, as is the case with the piano hammer, and applied to a contact area that may be smaller than that of the felt.

Molecular dynamics is a very efficient, though still detailed and complicated, approach to the micromechanical modeling of nonwoven fiber networks. Fiber-to-fiber friction for representing compression hysteresis can be incorporated in an overall potential function to be minimized. Moreover, its capability in involving various microscopic deformation schemes, as well as evaluating the structural parameter evolution, may provide the information required to predict bulk properties of the network in terms of individual fiber response.

Piano action - actuator mechanism

According to the simulation results, when compared to the experimental data obtained by the high-speed video cameras, applying a force input on the key as the pianist's finger force makes the simulated piano action very sensitive to the correct timing and precise regulation of the action components. In general, the load sensor on the key front records the overall reaction that is transmitted through the components to the point of application

of the force input during the key stroke. This force was obtained from the experimental prototype response. Therefore, utilizing the same force in the simulation model, which will inevitably have some measurement and modeling errors, leads to inaccurate results if each body does not perform its desired duty at precisely the right moment during the simulation. For instance, if the occurrence of contact between the hammer and backcheck shifts by a tiny time constant, it will produce a force on the capstan which belongs to another time in the real model and, hence, will result in different dynamic behavior. This affirms the necessity of utilizing a motion profile to the simulation model, as done in the real action . Some preliminary simulations with a prescribed motion input have been done and qualitatively compared with the experiments. More precise simulations using the real parameters of the motion-activated mechanism are left for future work. Moreover, there are several complicated biomechanical scenarios that can be implemented to incorporate more realistic features of the finger action in generating high-fidelity actuator models.

Provided that experimental data for every contact point of the action can be acquired, the new micromechanical contact model can be applied at all contact locations of the piano action mechanism. Furthermore, the felt model can be applied to other instruments (e.g., mallets on timpani or cymbals) and systems in general (e.g., clothing wear, upholstery) Integrating the actuator system and the piano action mechanism in a unified system is also a challenging problem in studying the interaction between the two dynamic simulation models.

References

[1] M. Alkhagen and S. Toll. Micromechanics of a compressed fiber mass. *Journal of Applied Mechanics*, 74:723–731, 2007.

[2] M. Alkhagen and S. Toll. The effect of fiber diameter distribution on the elasticity of a fiber mass. *Journal of Applied Mechanics*, 76(4):041014–1–041014–6, 2009.

[3] M. P. Allen and D. J. Tildesley. *Computer simulation of liquids*. Clarendon Press, Oxford, Oxfordshire, 1987.

[4] Robert Johnson Associates. *ESEM Manual: An Introduction to ESEM*. CA, USA, 1996.

[5] C. Barbier, R. Dendievel, and D. Rodney. Role of friction in the mechanics of nonbonded fibrous materials. *Physical Review Letters*, 80(1):016115 [5 pages], 2009.

[6] C. Barbier, R. Dendievel, and D. Rodney. Computational approach to the mechanics of entangled materials. In *18th French Congress of Mechanics*, Grenoble, France, 27-31 August 2007.

[7] N. B. Beil and W. W. Roberts JR. Modeling and computer simulation of the compressional behavior of fiber assemblies part I: comparison to van Wyk's theory. *Textile Research Journal*, 72(4):341–351, 2002.

[8] N. B. Beil and W. W. Roberts JR. Modeling and computer simulation of the compressional behavior of fiber assemblies: part II: hysteresis, crimp, and orientation effects. *Textile Research Journal*, 72(5):375–382, 2002.

[9] S. Buell, G. C. Rutledge, and K. J. Van Vliet. Predicting polymer nanofiber interactions via molecular simulations. *ACS Applied Materials & Interfaces*, 2(4):1164–1172, 2010.

[10] M. Bulacu. *Molecular Dynamics Studies of Entangled Polymer Chains*. PhD Thesis, University of Groningen, Groningen, The Netherlands, 2008.

[11] F. Cacho, P.J. Elbischger, J.F. Rodríguez, M. Doblaré, and G.A. Holzapfel. A constitutive model for fibrous tissues considering collagen fiber crimp. *International Journal of Non-Linear Mechanics*, 42(2):391–402, 2007.

[12] G. P. Cai, J. Z. Hong, and S. X. Yang. Dynamic analysis of a flexible hub-beam system with tip mass. *Mechanics Research Communications*, 32(2):173–190, 2005.

[13] G. A. Carnaby and J. I. Curiskis. The tangent compliance of staplefibre bundles in tension. *Journal of the Textile Institute*, 78(4):293–305, 1987.

[14] G. A. Carnaby and N. Pan. Theory of the compression hysteresis of fibrous assemblies. *Textile Research Journal*, 59:275–284, 1989.

[15] B. V. Chapnik, G. R. Heppler, and J. D. Aplevich. Modeling impact on a one-link flexible robotic arm. *IEEE Transactions on Robotics and Automation*, 7(4):479–488, 1991.

[16] T. F. Coleman and Y. Li. An interior, trust region approach for nonlinear minimization subject to bounds. *Society for Industrial and Applied Mathematics: Journal on Optimization*, 6(2):418–445, 1996.

[17] H. L. Cox. The elasticity and strength of paper and other fibrous materials. *British Journal of Applied Physics*, 3:72–79, 1952.

[18] S. J. Cull and R. W. Tucker. On the modeling of Coulomb friction. *Journal of Physics AMathematical and General*, 32(11):2103–2113, 1999.

[19] G. Van den Berghe, B. De Moor, and W. Minten. Modeling a grand piano key action. *Computer Music Journal*, 19(2):15–22, 1995.

[20] M. Djalili-Moghaddam and S. Toll. A model for short-range interactions in fibre suspensions. *Journal of NonNewtonian Fluid Mechanics*, 132(1-3):73–83, 2005.

[21] K. E. Ducketta and C. C. Chengb. A discussion of the cross-point theories of van Wyk. *Journal of the Textile Institute*, 69(2-3):55–59, 1978.

[22] J. I. Dunlop. Characterizing the compression properties of fibre masses. *Journal of the Textile Institute*, 65(10):532–536, 1974.

[23] J. I. Dunlop. On the compression characteristics of fibre masses. *Journal of the Textile Institute*, 74(2):92–97, 1983.

[24] J. I. Dunlop. Nonlinear vibration properties of felt pads. *The Journal of the Acoustic Society of America*, 88(2):911–917, 1990.

[25] H. Fletcher. Normal vibration frequencies of a stiff piano string. *The Journal of the Acoustical Society of America*, 36(1):203–209, 1964.

[26] G. Gilardi and I. Sharf. Literature survey of contact dynamics modelling. *Mechanism and Machine Theory*, 37(10):1213–1239, 2002.

[27] B. Gillespie. Dynamical modeling of the grand piano action. In *Proceeding of the International Computer Music Conference*, pages 77–80, San Jose, CA, 1992.

[28] B. Gillespie. *Haptic Display of Systems with Changing Kinematic Constraints: The Virtual Piano Action*. PhD Thesis, Stanford University, Stanford, CA, 1996.

[29] R. B. Gillespie and M. Cutkosky. Dynamical modeling of the grand piano action. In *Proceedings of the International Computer Music Conference*, pages 77–80, San Jose, CA, 1992.

[30] J. Goldstein, D. Newbury, D. Joy, C. Lyman, P. Echlin, E. Lifshin, L. Sawyer, and J. Michael. *Scanning Electron Microscopy and X-Ray Microanalysis*. Springer, New York, USA, third edition, 2003.

[31] P. Grosberg. The strength of twistless slivers. *Journal of the Textile Institute*, 54(6):T223–T233, 1963.

[32] P. Grosberg and P. A. Smith. The strength of slivers of relatively low twist. *Journal of the Textile Institute*, 57(1):T15–T23, 1966.

[33] E. Hayashi, M. Yamane, and H. Mori. Behavior of piano-action in a grand piano. I. Analysis of the motion of the hammer prior to string contact. *Journal of the Acoustical Society of America*, 105(6):3534–3544, 1999.

[34] S. Heyden. *Network Modelling for The Evaluation of Mechanical Properties of Cellulose Fibre Fluff*. PhD Thesis, Lund University, Lund, Sweden, 2000.

[35] M. Hirschkorn. Dynamic Model of a Piano Action Mechanism. MSc Thesis, University of Waterloo, Waterloo, ON, Canada, 2004.

[36] M. Hirschkorn, J. McPhee, and S. H. Birkett. Dynamic modeling and experimental testing of a piano action mechanism. *ASME Journal of Computational and Nonlinear Dynamics*, 1(1):47–55, 2006.

[37] W. Huang. *Online Characterization of Fabric Compressional Behavior*. PhD Thesis, North Carolina State University, Raleigh, North Carolina, 1999.

[38] K. H. Hunt and F. R. E. Crossley. Coefficient of restitution interpreted as damping in vibroimpact. *ASME Journal of Applied Mechanics*, 42(2):440–445, 1975.

[39] M. Itoh and T. Komori. An extension to the theory of the deformation of fiber assemblies. *Seni Gakkaishi*, 47(11):563–572, 1991.

[40] A. Izadbakhsh. Dynamics and Control of a Piano Action Mechanism. MSc Thesis, University of Waterloo, Waterloo, ON, Canada, 2006.

[41] A. Izadbakhsh, J. McPhee, and S. H. Birkett. Dynamic modeling and experimental testing of a piano action mechanism with a flexible hammer shank. *ASME Journal of Computational Nonlinear Dynamics*, 3(3):1–10, 2008.

[42] J. McPhee and C. Schmitke. *DynaFlexPro User's Manual*. MotionPro Inc., Waterloo, Ontario, Canada, 2006.

[43] F. Járai-Szabó. Computer Simulation Study of Entangled Materials. MSc Thesis, Grenoble Institute of Technology, Cluj-Napoca, Romania, 2003.

[44] A. A. Jeddi, H. S. Kim, and B. Pourdeyhimi. Measurement of fiber orientation in nonwovens: optical Fourier transform. *International Nonwovens Journal*, 10(3):10–16, 2001.

[45] A. Kabla and L. Mahadevan. Nonlinear mechanics of soft fibrous networks. *Journal of the Royal Society Interface*, 4(12):99–106, 2007.

[46] T. R. Kane and D. A. Levinson. *Dynamics: Theory and Applications*. McGraw-Hill, New York, NY, 1985.

[47] T. Komori and M. Itoh. A new approach to the theory of the compression of fiber assemblies. *Textile Research Journal*, 61(7):420–428, 1991.

[48] T. Komori and M. Itoh. Theory of the general deformation of fiber assemblies. *Textile Research Journal*, 61(10):588–594, 1991.

[49] T. Komori and M. Itoh. A model analysis of the compressibility of fiber assemblies. *Textile Research Journal*, 62:567–574, 1992.

[50] T. Komori and M. Itoh. A modified theory of fiber contact in general fiber assemblies. *Textile Research Journal*, 64:519–528, 1994.

[51] T. Komori and M. Itoh. Analyzing the compressibility of a random fiber mass based on the modified theory of fiber contact. *Textile Research Journal*, 67:204–210, 1997.

[52] T. Komori and K. Makishima. Numbers of fiber-to-fiber contacts in general fiber assemblies. *Textile Research Journal*, 47:13–17, 1977.

[53] T. Komori and K. Marishima. Estimation of fiber orientation and length in fiber assemblies. *Textile Research Journal*, 48(6):309–314, 1978.

[54] P. J. Kruger. Withdrawal forces in the processing of wool slivers: part I: the determination of withdrawal force. *Journal of the Textile Institute*, 58(10):463–471, 1967.

[55] H. M. Lankarani and P. E. Nikravesh. Continuous contact force models for impact analysis in multibody systems. *Nonlinear Dynamics*, 5(2):193–207, 1994.

[56] D. H. Lee and G. A. Carnaby. Compressional energy of the random fiber assembly part i: Theory. *Textile Research Journal*, 62(4):185–191, 1992.

[57] D. H. Lee and G. A. Carnaby. Compressional energy of the random fiber assembly part ii: Evaluation. *Textile Research Journal*, 62(5):258–265, 1992.

[58] D. H. Lee, G. A. Carnaby, A. J. Carr, and P. J. Moss. *A review of Current Micromechanical Models of the Unit Fibrous Cell*. WRONZ Communication no. C113, Canesis Network Limited, Canterbury, Christchurch, New Zealand, 1990.

[59] D. H. Lee, G. A. Carnaby, and S. K. Tandon. An energy analysis of the compression of a random fibre assembly. In *Proceedings of the 8th International Wool Textile research Conference*, pages V34–V44, Christchurch, New Zealand, 1990.

[60] D. H. Lee and J. K. Lee. Initial compressional behavior of fibre assembly. In *Objective Measurement: Applications to Product Design and Process Control (S. Kawabata, R. Postle, and M. Niwa (Eds.))*, pages 613–622, Osaka, Japan, 1985. The Textile Machinery Society of Japan.

[61] W. H. Lehmberg. Mechanical properties and uses of wool felt. Technical report, The Felt Association Inc., New York, NY, USA, 1945.

[62] H. L. Liu, W. D. Yu, and H. B. Jin. Modeling the stress-relaxation behavior of wool fibers. *Journal of Applied Polymer Science*, 110(4):2078–2084, 2008.

[63] A. E. H. Love. *A Treatise on the Mathematical Theory of Elasticity*. Cambridge University Press, Cambridge, UK, forth edition, 1927.

[64] Maplesoft. *Maple 11 User Manual*. Maplesoft, a division of Waterloo Maple Inc., Waterloo, ON, Canada, 2007.

[65] R. Masoudi, S. H. Birkett, and J. McPhee. Dynamic model of a vertical piano action mechanism. In *Proceeding of ASME IDETC/CIE*, pages 389–398, San Diego, California, USA, August 30 - September 2 2009.

[66] R. Masoudi, S. H. Birkett, and A. Salehian. Dynamic simulation and vibration analysis of a mechanical piano key actuator. In *Proceeding of ASME IDETC/CIE*, Washington, DC, USA, August 28–31 2011.

[67] MATLAB®. *Version 7.10.0 (R2010a)*. The MathWorks Inc., Natick, Massachusetts, 2010.

[68] P. A. Matveev and A. M. Rymskij-Korsakov. *Sbornik*. 1937.

[69] J. McPhee. Unified modeling theories for the dynamics of multibody systems. In *Advances in Computational Multibody Systems*, pages 125–154, Dordrecht, The Netherlands, 2005. Springer.

[70] J. McPhee, C. Schmitke, and S. Redmond. Dynamic modelling of mechatronic multibody systems with symbolic computing and linear graph theory. *Mathematical and Computer Modelling of Dynamical Systems*, 10(1):1–23, 2004.

[71] L. Meirovitch. *Fundamentals of Vibrations*. McGraw-Hill, New York, NY, 2001.

[72] M. A. Narter, S. K. Batra, and D. R. Buchanan. Micromechanics of three-dimensional fibrewebs: constitutive equations. *Proceedings of the Royal Society A Mathematical Physical and Engineering Sciences*, 455(1989):3543–3563, 1999.

[73] B. Neckář. Compression and packing density of fibrous assemblies. *Textile Research Journal*, 67(2):123–130, 1997.

[74] B. Neckář and S. Ibrahim. A contribution to van wyk's theory of contacts between fibers. In *Adevanced Flexible Materials and Structures: Engineering with Fibers*. The Fiber Society 2003 Spring Symposium, Loughborough University, UK, 2003.

[75] A. Oledzki. Dynamics of piano mechanisms. *Mechanism and Machine Theory*, 7(4):373–385, 1972.

[76] N. Pan. A modified analysis of the microstructural characteristics of general fiber assemblies. *Textile Research Journal*, 63(6):336–345, 1993.

[77] J. Park and N. Kang. Applications of fiber models based on discrete element method to string vibration. *Journal of Mechanical Science and Technology*, 23(2):372–380, 2009.

[78] D. Perrin, M. Alteirac, S. Corn, and M. E. R. Shanahan. A novel method for the measurement of elastic moduli of fibres. *Composites: Part A, Applied science and manufacturing*, 38(1):71–79, 2007.

[79] W. Pfeiffer. *The Piano Key and Whippen: An Analysis of their Relationship in Direct Blow Actions.* Verlag Das Musikinstrument, Frankfurt am Main, Germany, volume 18 of fachbuchreihe das musikinstrument edition, 1967.

[80] D. Poquillon, B. Viguier, and E. Andrieu. Experimental data about mechanical behaviour during compression tests for various matted fibres. *Journal of Materials Science*, 40(22):5963–5970, 2005.

[81] B. Pourdeyhimi. Assessing fiber orientation in nonwoven fabrics. *INDA Journal of Nonwovens Research*, 5(3):29–36, 1993.

[82] B. Pourdeyhimi and R. Dent. Measuring fiber orientation in nonwovens, part IV: flow field analysis. *Textile Research Journal*, 67(3):181–187, 1997.

[83] B. Pourdeyhimi and R. Dent. Measuring fiber diameter distribution in nonwovens. *Textile Research Journal*, 69(4):233–236, 1999.

[84] B. Pourdeyhimi, R. Dent, and H. Davis. Measuring fiber orientation in nonwovens, part III: Fourier transform. *Textile Research Journal*, 67(2):143–151, 1997.

[85] B. Pourdeyhimi, R. Dent, A. Jerbi, S. Tanaka, and A. Deshpande. Measuring fiber orientation in nonwovens part V: real webs. *Textile Research Journal*, 69 (3):185–192, 1999.

[86] B. Pourdeyhimi and H. S. Kim. Measuring fiber orientation in nonwovens: the Hough transform. *Textile Research Journal*, 72(9):803–809, 2002.

[87] B. Pourdeyhimi, R. Ramanathan, and R. Dent. Measuring fiber orientation in nonwovens, part I, Simulation. *Textile Research Journal*, 66(11):713–722, 1996.

[88] B. Pourdeyhimi, R. Ramanathan, and R. Dent. Measuring fiber orientation in nonwovens, part II: direct tracking. *Textile Research Journal*, 66(12):747–753, 1996.

[89] B. Pourdeyhimi, Y. Velu, A. Deshpande, and S. Tanaka. Measurement of fiber orientation in nonwovens. In *Proceedings of the International Nonwovens Technical Conference*, Cambridge, MA, 8 September 1997.

[90] B. Pourdeyhimi and B. Xu. Pore size characterizing in nonwoven fabrics. *INDA Journal of Nonwovens Research*, 5(3):20–27, 1993.

[91] B. Pourdeyhimi and B. Xu. Characterizing pore size in nonwoven fabrics: shape considerations. *International Nonwovens Journal*, 6(1):26–30, 1994.

[92] A. Rawal. A modified micromechanical model for the prediction of tensile behavior of nonwoven structures. *Journal of Industrial Textiles*, 36(2):133–149, 2006.

[93] A. Rawal. Application of theory of compression to thermal bonded non-woven structures. *Journal of the Textile Institute*, 100(1):28–34, 2009.

[94] A. Rawal, S. Lomov, Th. Ngo, I. Verpoest, and J. Vankerrebrouck. Mechanical behavior of thru-air bonded nonwoven structures. *Textile Research Journal*, 77(6):417–431, 2007.

[95] A. Rawal, S. Lomov, and I. Verpoest. An environmental scanning electron microscope study of a through-air bonded structure under tensile loading. *Journal of the Textile Institute*, 99(3):235–241, 2008.

[96] A. Rawal, P. K. Mishra, and H. Saraswat. Modeling the compression-induced morphological behavior of nonwoven materials. *Journal of Materials Science*, Online version:1–10, 2011.

[97] D. Rodney, M. Fivel, and R. Dendievel. Discrete modeling of the mechanics of entangled materials. *Physical Review Letters*, 95(10):108004 [4 pages], 2005.

[98] M. Sherburn. *Geometric and Mechanical Modelling of Textiles*. PhD Thesis, University of Nottingham, Nottingham, UK, 2007.

[99] SolidWorks® Office Premium. *SolidWorks 2007 Online User's Guide - SP0.0* . SolidWorks Corporation, Concord, Massachusetts, USA, 2007.

[100] W. Stamm. Compressional Behavior of Felt. MSc thesis, University of Waterloo, Waterloo, ON, Canada, 2004.

[101] S. B. Stankovic. Compression hysteresis of fibrous systems. *Polymer Engineering and Science*, 48(4):676–682, 2008.

[102] Steinway & Sons. *World-Wide Technical Reference Guide*. Steinway & Sons, New York, 2007.

[103] A. Stulov. A simple grand piano hammer felt model. In *Proceedings of the Estonian Academy of Sciences, Engineering*, volume 1, pages 172–182, Tallinn, Estonia, 1995. Eesti Teaduste Akadeemia toimetised.

[104] A. Stulov. Dynamic behavior and mechanical features of wool felt. *Acta Mechanica*, 169:13–21, 2004.

[105] A. Stulov. Experimental and computational studies of piano hammers. *Acta Acustica with Acustica*, 91(6):1086–1097, 2005.

[106] A. Stulov. Experimental and theoretical studies of piano hammer. In *Proceedings of the Stockholm Music Acoustics Conference*, Stockholm, Sweden, August 6-9 2003.

[107] A. Stulov and A. Magi. Piano hammer testing device. In *Proceedings of the Estonian Academy of Sciences, Engineering*, volume 6, pages 259–267, Tallinn, Estonia, 2000. Eesti Teaduste Akadeemia toimetised.

[108] J. C. Tan, J. A. Elliott, and T. W. Clyne. Analysis of tomography images of bonded fibre networks to measure distributions of fibre segment length and fibre orientation. *Advanced Engineering Materials*, 8(6):495–500, 2006.

[109] S. Toll. Note: On the tube model for fiber suspensions. *Journal of Rheology*, 37(1):123–125, 1993.

[110] S. Toll. Packing mechanics of fiber reinforcements. *Polymer Engineering and Science*, 38(8):1337–1350, 1998.

[111] S. Toll and J.-A. E. Manson. Elastic compression of a fiber network. *Transactions of the ASME Journal of Applied Mechanics*, 62(1):223–226, 1995.

[112] T. N. Topper and B. L. Wills. The computer simulation of piano mechanisms. *International Journal of Modeling and Simulation*, 7(4):135–139, 1987.

[113] C. Truesdell and W. Noll. *The Non-Linear Field Theories of Mechanics*. Springer, Berlin, 2nd edition, 1992.

[114] G. Van den Berghe, B. De Moor, and W. Minten. Modeling a grand piano key action. *Computer Music Journal*, 19(2):15–22, 1995.

[115] C. M. van Wyk. Note on the compressibility of wool. *Journal of the Textile Institute*, 37(12):T285–T292, 1946.

[116] D. Šajn, J. Geršak, and R. Flajs. Prediction of stress relaxation of fabrics with increased elasticity. *Textile Research Journal*, 76(10):742–750, 2006.

[117] C. P. Vyasarayani. *Transient Dynamics of Continuous Systems with Impact and Friction, with Applications to Musical Instruments*. PhD Thesis, University of Waterloo, Waterloo, ON, CA, 2009.

[118] C. P. Vyasarayani, S. H. Birkett, and J. McPhee. Modelling the dynamics of a compliant piano action mechanism impacting an elastic stiff string. *Journal of Acoustical Society of America*, 125(6):4034–4042, 2009.

[119] Wikipedia® Wikimedia Foundation Inc. Wikipedia, January 2012.

[120] X.-F. Wu and Y. A. Dzenis. Elasticity of planar fiber networks. *Journal of Applied Physics*, 98(9):093501–1–093501–9, 2005.

[121] A. S. Yigit, A. G. Ulsoy, and R. A. Scott. Dynamics of a radially rotating beam with impact, part 1: theoretical and computational model. *Journal of Vibration and Acoustics*, 112(1):65–70, 1990.

[122] A. S. Yigit, A. G. Ulsoy, and R. A. Scott. Dynamics of a radially rotating beam with impact, part 2: experimental and simulation results. *Journal of Vibration and Acoustics*, 112(1):71–77, 1990.

[123] A. S. Yigit, A. G. Ulsoy, and R. A. Scott. Spring-dashpot models for the dynamics of a radially rotating beam with impact. *Journal of Sound and Vibration*, 142(3):515–525, 1990.

APPENDICES

Appendix A

Vertical Piano Action Parameters

The parameters used for the modeling and simulation of the piano action mechanism including piano action components, bridle strap, joint springs, and contact parameters are given below. Figures A.1 and A.2 show the main bodies of the action, modeling points, and local reference frames considered on each component.

A.1 Mass and structural properties

Table A.1: Mass properties of the components

Component	Mass (kg)	Mass Moment of Inertia (kgmm^2)	Center of Mass (mm)
Key	0.1176	1741	(-46.3 13.10)
Whippen	0.9506E-2	20.94	(29.30 7.10)
Jack	0.2883E-2	1.892	(1.20 25.60)
Backcheck	0.1921E-2	0.176	(-14.0 -1.4)
Hammer butt	7.58E-3	2.70	(12.7 13.4)
Hammer	7.8E-3	3.10	(0.0 36.9)
Damper	0.1318E-1	56.68	(-4.90 39.8)
Massless body	0.1E-15	0.1E-14	(0.0 0.0)

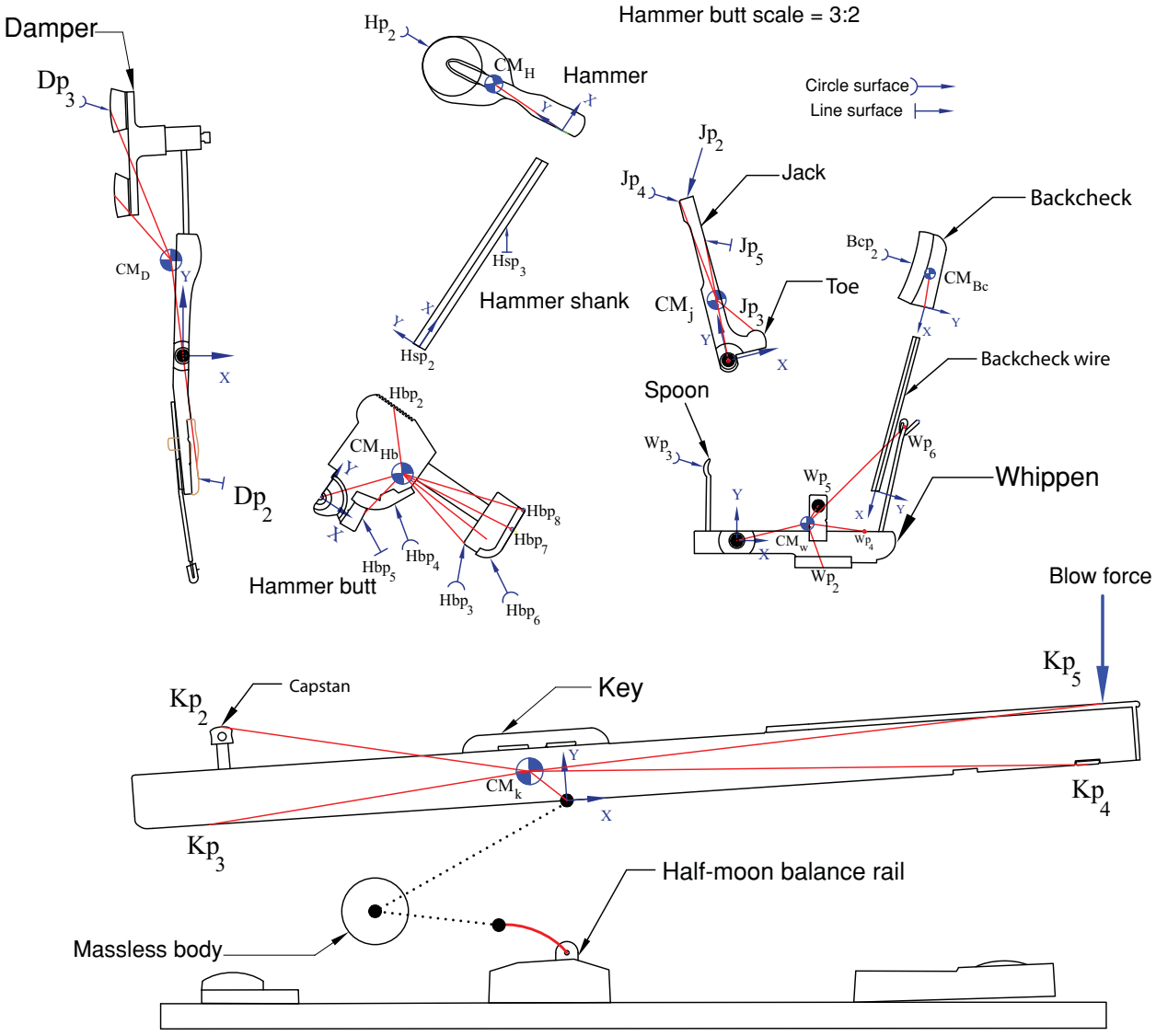

Figure A.1: Modeling points defined on the vertical action components.

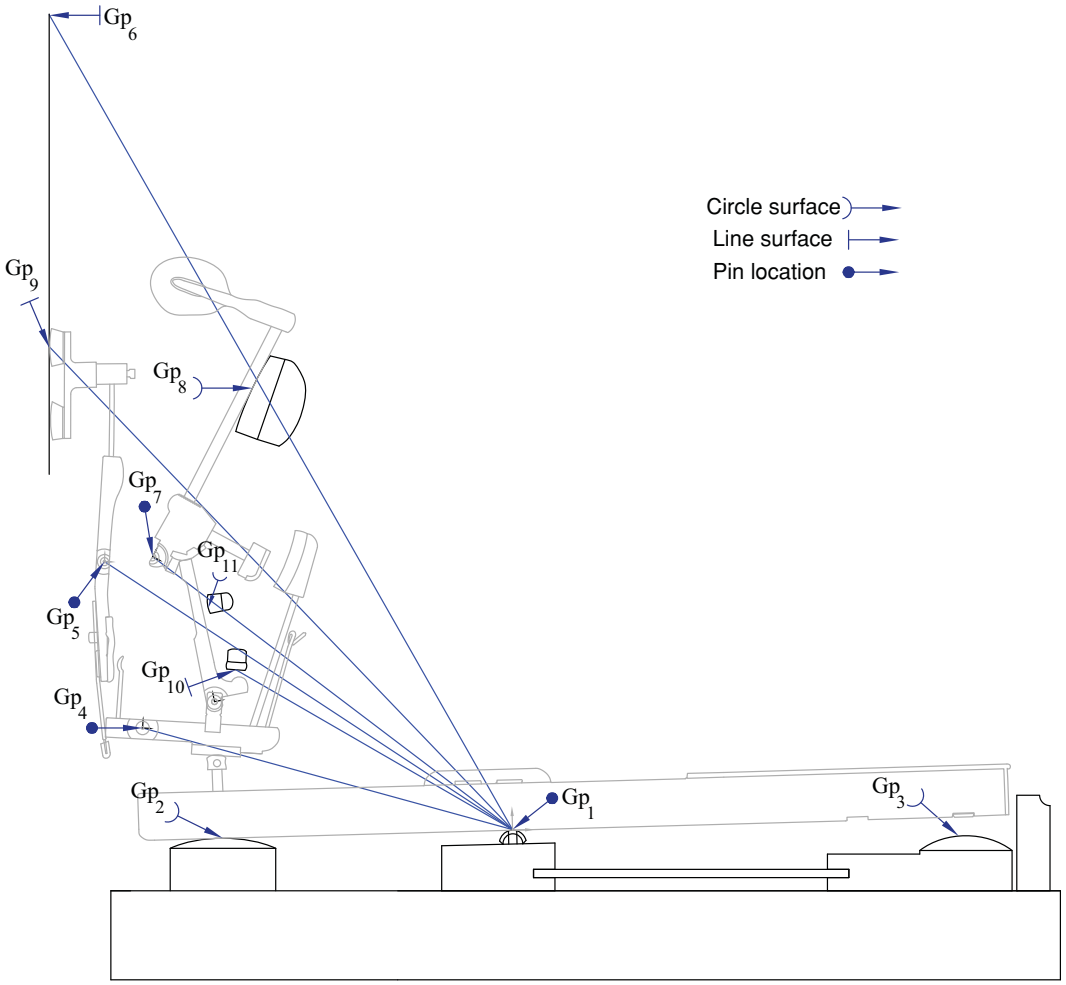

Figure A.2: Ground point locations in the vertical piano action.

Table A.2: Structural properties of hammer shank and backcheck wire

Component	Mass density (kg/m^3)	Length (mm)	Modulus of rigidity (GPa)	Modulus of elasticity (GPa)	Area (mm^2)
Hammer shank	701.18	93.0	7.4	12.618	25.51
Backcheck wire	7830	66.1	74	60.933	6.38

A.2 Geometric information of the contact/pin points

Table A.3: Global position and geometry of ground modeling points

Contact point	Geometry type	Global position (mm)	Normal vector	Radius (mm)	Arc (rad)
Gp_1	Pin	(0 0)			
Gp_2	Circle	(-139 -388)		382	
Gp_3	Circle	(218 -40.7)		38	
Gp_4	Pin	(-178 48.9)			
Gp_5	Pin	(-196 129)			
Gp_6	Line	(-223 327)	(0.9999 0.0106)		
Gp_7	Pin	(-173 131)			
Gp_8	Circle	(3.0 151)		142	
Gp_9	Line	(-222 232)	(0.9999 0.0106)		
Gp_{10}	Line	(-133 77.4)	(-0.0726 -0.9974)		
Gp_{11}	Circle	(-113 112)		30.7	

Table A.4: Local position and geometry of key modeling points

Contact point	Geometry type	Local position (mm)	Normal vector	Radius (mm)	Arc (rad)
Kp_2	Circle	(-141 32.6)		7.9	
Kp_3	Line	(-149 0)	(0.0 -1.0)		
Kp_4	Line	(217 0.2859)	(0.0 -1.0)		
Kp_5	Line	(225 25.1)	(0.0 1.0)		

Table A.5: Local position and geometry of whippen modeling points

Contact point	Geometry type	Local position (mm)	Normal vector	Radius (mm)	Arc (rad)
Wp_2	Line	(35.9 -11.2)	(0.0 -1.0)		
Wp_3	Circle	(-7.9 29.6)		4.8	
Wp_4	Weld	(53.1 3.7)			
Wp_5	Pin	(33.8 14.5)			
Wp_6	Pin	(69.8 47.3)			

Table A.6: Local position and geometry of backcheck modeling points

Contact point	Geometry type	Local position (mm)	Normal vector	Radius (mm)	Arc (rad)
Bcp_2	Circle	(-19.1 -88.7)		81.0	

Table A.7: Local position and geometry of jack modeling points

Contact point	Geometry type	Local position (mm)	Normal vector	Radius (mm)	Arc (rad)
Jp_2	Hybrid	(-3.1 68.5)		1.0	(1.620 3.148)
Jp_3	Circle	(13.1 5.4)		4.0	
Jp_4	Circle	(-3.1 68.5)		1.0	
Jp_5	Line	(2.4 51.4)	(0.9996 0.0272)		

Table A.8: Local position and geometry of hammer butt modeling points

Contact point	Geometry type	Local position (mm)	Normal vector	Radius (mm)	Arc (rad)
Hbp_2	Weld	(3.1 32.0)			
Hbp_3	Bridle strap	(40.2 11.2)			
Hbp_4	Circle	(9.5 13.2)		9.2	
Hbp_5	Line	(12.6 3.0)	(0.9948 0.1016)		
Hbp_6	Circle	(44.8 15.6)		5.1	
Hbp_7	Circle	(49.2 21.7)		0.5	
Hbp_8	Circle	(48.9 27.9)		0.5	

Table A.9: Local position and geometry of hammer modeling points

Contact point	Geometry type	Local position (mm)	Normal vector	Radius (mm)	Arc (rad)
Hp_2	Circle	(-2.8 52.8)		12.3	

Table A.10: Local position and geometry of damper modeling points

Contact point	Geometry type	Local position (mm)	Normal vector	Radius (mm)	Arc (rad)
Dp_2	Line	(6.4 -51.0)	(0.9974 0.0723)		
Dp_3	Circle	(13.6 104.1)		43.9	

Table A.11: Local position and geometry of hammer shank modeling points

Contact point	Geometry type	Local position (mm)	Normal vector	Radius (mm)	Arc (rad)
Hsp_2	Weld	(93.0 0.0)			
Hsp_3	Line	(62.1 -2.8)	(0.0 -1.0)		

A.3 Contact interface parameters

Parameters for 15 contact points in the vertical piano action are listed in Table A.12. The constant parameters a, b, and c can be acquired by fitting the mathematical curve presented in equation 4.21 to the experimental data, which fits notably well to both loading and unloading data.

Table A.12: Contact parameters of components interfaces in vertical action

Contact	Interfaces		Curve fit parameters					
			Loading			Unloading		
			a	b	c	a	b	c
1	Gp_2	Kp_3	5.52E+03	1.58E+03	-0.60E+03	0.19E+03	5.04E+03	3.04E+03
2	Gp_3	Kp_4	2.63E+03	1.36E+03	0.80E+03	0.78E+01	0.36E+03	0.21E+03
3	Kp_2	Wp_2	2.70E+04	1.15E+03	-2.24E+04	0.42E+03	5.25E+03	2.74E+03
4	Hbp_2	Jp_2	1.70E+04	1.56E+04	-4.87E+03	0.18E+03	4.32E+04	1.53E+04
5	Jp_3	Gp_{10}	2.62E+03	2.96E+03	-1.15E+03	0.03E+03	7.99E+03	2.48E+03
6	Hp_2	Gp_6	2.35E+04	1.74E+03	-2.41E+04	2.00E+03	4.52E+03	-0.82E+03
7	Gp_8	Hsp_3	0.14E+03	0.73E+03	0.18E+03	0.28E+01	1.61E+03	0.26E+03
8	Bcp_2	Hbp_6	2.42E+03	1.59E+03	-1.16E+03	0.12E+03	3.62E+03	1.36E+03
9	Wp_3	Dp_2	7.08E+04	0.10E+03	-7.03E+04	5.49E+03	0.94E+03	-6.38E+03
10	Dp_3	Gp_9	0.28E+03	1.00E+03	0.22E+03	0.95E+01	2.30E+03	0.33E+03
11	Jp_4	Hbp_5	0.44E+03	1.63E+03	0.50E+03	0.01E+03	3.55E+03	0.80E+03
12	Gp_{11}	Jp_5	0.47E+03	1.23E+03	-0.09E+03	0.03E+03	2.77E+03	0.24E+03
13	Bcp_2	Hbp_8	2.62E+03	1.84E+03	-2.37E+03	0.12E+03	4.13E+03	1.12E+03
14	Bcp_2	Hbp_7	2.62E+03	1.84E+03	-2.37E+03	0.12E+03	4.13E+03	1.12E+03
15	Gp_{12}	Kp_1	2.70E+04	2.64E+03	-22.71E+03	3.07E+03	6.23E+03	-2.96E+03

Friction parameters for both contact surfaces and joints were estimated by relying on the similarity of component interactions in the vertical and grand piano actions, which have

been extracted by Hirschkorn [35]. In his thesis, he applied the common Coulomb friction criterion and estimated the value of coefficient of friction using the following mathematical function based on normal speed ν_n between interacting bodies and a threshold speed v_t, which provides smooth transition between kinetic and static coefficients of friction:

$$\mu = A\left(\tanh(\nu_n/v_t) + \frac{B_1\nu_n/v_t}{1+B_2(\nu_n/v_t)^4}\right) \tag{A.1}$$

in which A, B_1, and B_2 are constant parameters. The corresponding friction parameters for contact surfaces and revolute/prismatic joints are listed in Tables A.13 and A.14, respectively.

Table A.13: Friction parameters for contact interfaces

Contact		1	2	3	4	5	6	7	8	9	10	11	12	13	14	15
Constants	A	0	0	0.332	0.332	0.434	0.434	0	1.085	0.332	0	0.434	0	1.085	1.085	0
	B_1	0	0	0.73	0.73	1.78	1.78	0	1.78	0.73	0	1.78	0	1.78	1.78	0
	B_2	0	0	1	1	1	1	0	1	1	0	1	0	1	1	0

A.4 Joint friction parameters — springs and bridle strap model

The bridle strap is included in the dynamic model of the piano action as a one-sided spring/actuator model, which only acts when the strap is in tension. In Equation 4.5, $f_{bs} = K_{bs}\Delta_{bs}$ in which $K_{bs} = (3.47\text{E}{+}07)\,\Delta_{bs}^2 + (1.84\text{E}{+}05)\,\Delta_{bs} - 63.45$ has been estimated using experimental data obtained from tension tests on the strap. $L_{bs} = 45.5\,\text{mm}$ is the unreformed length of the strap.

The parameters for torsional spring between whippen and jack, hammer and ground, and damper and ground are listed in Table A.15

Table A.14: Friction parameters for revolute and prismatic joints

Component	A	B_1	B_2	Threshold velocity, w_t or v_t (rad/s or m/s)
Key - ground (revolute)	0.0079	0	0	0.0001
Whippen - ground	7.94E-04	0	0	0.0001
Jack - whippen	0.000397	0	0	0.0001
Damper - ground	0.0049	0	0	0.0001
Hammer - ground	0.0025	0	0	0.0001
Key - ground (prismatic)	0.0664	0	0	0.00001

Table A.15: Parameters for the rotational springs between components

Spring location	K (N.m/rad)	θ_0 (rad)	Spring formulation
Whippen - jack	0.0069	0.40	$T_{wj} = K_{wj}(\theta_j - \theta_{j0})$
Hammer - ground	0.98E-03	-2.8	$T_{hg} = K_{hg}(\theta_h - \theta_{h0})$
Damper - ground	0.0574	0.70	$T_{dg} = K_{dg}(\theta_d - \theta_{d0})$

Appendix B

Piano Key Actuator Parameters

Structural and geometrical parameters used in the dynamic modeling of the key actuator, shown in Figure 5.3 and introduced in the equations of Chapter 5, are listed in Table B.1 for both wooden and aluminum arms.

Table B.1: Geometry and material properties of the key actuator components

Parameter	Description	Unit	Aluminum arm	Wooden arm
a	Hub effective radius	m	61.08E-03	68.48E-03
L	Effective length of the beam	m	38.85E-03	33.05E-03
ρ	Mass density	kg/m^3	2.54E03	7.74E+02
A	Cross section area	m^2	81.44E-06	22.39e-6
E	Beam modulus of elasticity	Pa	6.83e10	10.0E+09
I	Second moment of area	m^4	283.25E-12	5.93E-12
J_h	Moment of inertia of the hub	kg.m^2	51.35E-06	51.35E-06
m_t	Tip mass	kg	1.57E-03	1.29E-03
r	Eccentricity	m	3.39E-03	5.00E-03